Doctoral Dissertation
Doctoral Program in Electrical, Electronics and Communications Engineering (38.th cycle)

Microwave Sensing and Imaging for Early Detection of Neurodegenerative Diseases

Leonardo Cardinali

* * * * *

Supervisors
Prof. Francesca Vipiana, Supervisor
Dr. Jorge Alberto Tobón Vásquez, Co-supervisor

Doctoral Examination Committee:
Prof. Elise Carolyn Fear, Referee, University of Calgary
Prof. Jan Vrba, Referee, Czech Technical University

Politecnico di Torino
May 26, 2026

I hereby declare that, the contents and organization of this dissertation constitute my own original work and does not compromise in any way the rights of third parties, including those relating to the security of personal data.

. . . . . .

Leonardo Cardinali
Turin, May 26, 2026

Summary

Neurodegenerative diseases such as Alzheimer's disease and Parkinson's disease represent a major and growing global health challenge. Both conditions are progressive and currently incurable, with symptoms that evolve over a long prodromal phase. Despite their different clinical manifestations, they share a common need for early detection: identifying pathological changes at an initial stage can significantly improve patients' quality of life, enable timely therapeutic interventions, support caregivers, and reduce the socio-economic burden on healthcare systems. However, existing diagnostic techniques are often invasive, expensive, or unsuitable for large-scale screening, limiting their applicability in early-stage.

In this context, microwave-based techniques have recently attracted attention as non-invasive, low-cost, and portable alternatives for neurological assessment. Operating through the interaction between electromagnetic waves and biological tissues, these methods are sensitive to variations in dielectric properties associated with physiological and pathological changes. Such characteristics make microwave technologies particularly appealing for population-level screening.

The first part of this thesis focuses on Alzheimer's disease (AD) and investigates the feasibility of microwave sensing for its early detection and staging. The proposed approach is motivated by emerging evidence that abnormal concentrations of protein biomarkers in the early phases of AD induce measurable changes in the electromagnetic properties of cerebrospinal fluid (CSF). A conformal six-element antenna array, positioned on the upper portion of the head and operating in the 500 MHz to 6.5 GHz frequency range, was designed to measure variations in the scattering parameters resulting from intracranial CSF permittivity changes. Diagnostic information was extracted using a multi-layer perceptron neural network. The classification strategy consisted of a two-step process, comprising a binary classification to determine disease presence and a multi-class classification to assess disease severity. The system was trained and validated through controlled experiments conducted on an anthropomorphic, multi-tissue head phantom, specifically designed for this application. The results demonstrate that reliable classification can be achieved using amplitude-only data, supporting the feasibility of the proposed method.

The second part of the thesis addresses Parkinson's disease, that is characterized by neurodegenerative processes affecting the substantia nigra, a deep brain structure,

which in its early stages may lead to dielectric asymmetries between the two brain hemispheres. In this work, the potential of differential microwave imaging to detect small permittivity contrasts associated with the illness was investigated through a controlled phantom study. A simplified two-dimensional head phantom was developed using a 3D-printed cylindrical container filled with water, incorporating a Teflon tube to represent the substantia nigra. The tube was filled with hot water, whose gradual cooling was used to emulate controlled dielectric variations. A four-antenna differential imaging system was employed, with image reconstruction performed using the multi-frequency bi-focusing algorithm. The results demonstrate the ability of the system to detect dielectric contrasts corresponding to temperature variations as small as 0.4°C, equivalent to approximately 0.17% in relative permittivity. Although the exact dielectric alterations associated with Parkinson's disease are not yet fully characterized, these findings confirm the high sensitivity of the proposed approach and support the potential of differential microwave imaging as a promising tool for future investigations into Parkinson's disease detection.

Overall, this thesis demonstrates the feasibility and sensitivity of microwave-based sensing and imaging techniques for the early investigation of neurodegenerative diseases, highlighting their potential role as complementary, non-invasive tools for large-scale screening and preliminary diagnosis of Alzheimer's and Parkinson's disease.

Acknowledgements

First of all, I would like to thank my supervisor, Professor Francesca Vipiana, for the attention and dedication she has always shown to me and to the entire Wavision research group. From the very beginning, she has been an example of how to lead a passionate team with decisiveness and scientific rigor, while never neglecting the personal attention that each member deserves. I am also deeply grateful to my co-supervisor, Dr. Jorge Tobón, who has always been there whenever I needed guidance and support.

I would also like to thank Professor Luis Jofre-Roca for his invaluable guidance during my time at Universitat Politècnica de Catalunya. His advice and the time he dedicated to sharing his thoughts and experiences have been extremely enriching for my work and my personal life.

Finally, I wish to thank David, Martina, Cristina, Ali, Martin, Michael, Kaan, Jorge, Victor, Calin, Ramiro, Stefano, Marco, and all the colleagues who accompanied me throughout this journey. A special thanks goes to Valeria, whose meticulous revisions greatly improved the quality of this thesis.

I would like to dedicate
this work to my parents
and to my grandparents,
thank you for the
unconditional support
you always gave me

Contents

List of Tables xi

List of Figures xiii

1 Introduction 1
- 1.1 Principles of Microwave-Based Techniques . . . 1
  - 1.1.1 Scattering Parameters and Vector Network Analyzers . . . 3
  - 1.1.2 Microwave Sensing . . . 5
  - 1.1.3 Microwave Imaging . . . 6
- 1.2 The Uses of Microwave Imaging and Sensing . . . 6
- 1.3 Medical Applications . . . 7
- 1.4 Motivation and Thesis Outline . . . 8

2 Alzheimer's Disease 11
- 2.1 Overview of Alzheimer's Disease and Risk Factors . . . 11
  - 2.1.1 Clinical Symptoms, Disease Progression and Physiological Changes 12
  - 2.1.2 Epidemiology and Global Impact . . . 13
- 2.2 Diagnosis . . . 15
  - 2.2.1 Clinical Examination and Symptom Based Diagnosis . . . 15
  - 2.2.2 Imaging and Laboratory Tests Used in AD . . . 15
- 2.3 Current approaches for early detection . . . 19
- 2.4 Microwave Based Approach to AD Detection . . . 19
  - 2.4.1 Rationale for Microwave Sensing in This Work . . . 20

3 A proof-of-concept Study of Microwave Sensing for Early Alzheimer's Disease Detection 23
- 3.1 Setup . . . 23
- 3.2 Phantom . . . 24
- 3.3 Antennas . . . 27
- 3.4 Data Acquisition Protocol and Dataset Construction . . . 28
- 3.5 Machine Learning Implementation Strategies . . . 29
- 3.6 Experimental Results and Discussion . . . 31

4 Design and Validation of a Microwave Sensing System for Early Alzheimer's Disease Detection **33**
4.1 Microwave Sensing System . . . 33
4.1.1 Antenna Selection and Configuration . . . 34
4.2 Custom Phantom Development . . . 36
4.2.1 Material Selection and Characterization . . . 36
4.2.2 Phantom Fabrication Process . . . 39
4.3 Dataset Construction and Evaluation Protocol . . . 40
4.3.1 Measurement Setup and Protocols . . . 40
4.3.2 Data Augmentation . . . 40
4.3.3 Dataset Partitioning . . . 41
4.4 Machine Learning for Classification . . . 44
4.4.1 Principal components analysis . . . 44
4.4.2 Classification Algorithm and Training Strategy . . . 45
4.4.3 Performance Metrics and Evaluation Criteria . . . 47
4.5 Results and Discussion . . . 48
4.5.1 Binary classification . . . 48
4.5.2 Multiclass classification . . . 50
4.5.3 Clinical implementation . . . 52

5 Parkinson's Disease **53**
5.1 Overview on Parkinson's Disease . . . 53
5.1.1 Clinical Symptoms, Disease Progression and Physiological Changes 54
5.1.2 Epidemiology and Socio-Economic Impact . . . 55
5.2 Diagnosis . . . 56
5.2.1 Clinical Examination and Sypmtom-Based Diagnosis . . . 56
5.2.2 Imaging and Laboratory Tests Used in PD . . . 57
5.3 Current Early Diagnostic Strategies . . . 57
5.3.1 Digital and Sensor-Based Monitoring . . . 58
5.3.2 Biomarkers and Neuroimaging Techniques . . . 59
5.4 Opportunities for Microwave Imaging in PD . . . 59

6 Microwave Imaging for Parkinson's Disease Detection **63**
6.1 Dielectric Characterization of Water . . . 64
6.1.1 Theoretical Model from Literature . . . 64
6.1.2 Experimental Measurements . . . 65
6.2 Microwave Imaging System . . . 68
6.2.1 Antennas . . . 69
6.2.2 Phase Center Determination . . . 71
6.3 Multi-Frequency Bi-Focusing Imaging Algorithm . . . 72
6.3.1 Algorithm Description . . . 72
6.4 Experimental Phantom Design and Fabrication . . . 74

6.5 Thermal Analysis and Stability of the Phantom Environment 75
6.5.1 Measurement Setup and Protocols 76
6.6 Experimental Results and Discussion 77

7 Conclusion and Perspectives **81**
7.1 Summary of Contributions 81
7.1.1 Alzheimer's disease 81
7.1.2 Parkinson's disease 83
7.2 Open Challenges and Future Directions 84
7.2.1 Alzheimer's disease 85
7.2.2 Parkinson's disease 85

Bibliography **87**

List of Tables

1.1 ITU/IEC frequency band classification within the microwave range. . . 2
1.2 IEEE Standard 521-2002 radar-frequency band nomenclature. 2
2.1 Key Findings from the Macroeconomic Burden Analysis of Alzheimer's Disease and Other Dementias (ADODs) [60] 14
2.2 Standardized cognitive and functional assessment protocols for Alzheimer's disease 16
2.3 Overview of physiological biomarkers associated with Alzheimer's disease across different measurement modalities. 18
2.4 Summary of journal articles on microwave sensing/imaging for Alzheimer's related detection. 21
3.1 Recipes of solid materials used in the anthropomorphic phantom employed in the proof-of-concept study. 25
3.2 Definition of Training Sets for Robustness Analysis 29
3.3 Optimized parameters for Method 1 29
3.4 Optimized Parameters for Method 2 30
3.5 Optimized Parameters for Method 3 31
3.6 Comparative Accuracy of the Three Methods on Test Data 32
3.7 Detailed classification metrics for Set 4 (Test Data) 32
4.1 Optimized geometrical parameters of the circular monopole antenna (dimensions in mm). 34
4.2 Graphite powder mass percentage for tissue-mimicking mixtures. . . . 37
4.3 Recipes for artificial CSF 38
4.4 Binary classification, hyperparameters optimization results, DD1. . . . 46
4.5 Binary classification, hyperparameters optimization results, DD2. . . . 46
4.6 Binary classification, validation phase accuracy results in percentages. 48
4.7 Binary classification performances on the test set, Data Division 1, results in percentages. 48
4.8 Binary classification performances on the test set, Data Division 2, results in percentages. 49
4.9 Multi-class classification, module configuration, MLP hyper-parameters. 50
5.1 Economic and social impact of Parkinson's disease. 56
5.2 Current imaging and laboratory technologies for PD detection. 58

5.3 Pre-Symptomatic and Early Diagnostic Biomarkers for Parkinson's Disease (Non-Motor). 60
6.1 Relative sensitivity of σ per 0.1°C shift at specific frequencies. 67
6.2 Relative sensitivity of ε_r per 0.1°C shift at specific frequencies. 68

List of Figures

2.1 Alzheimer's dieasease progression with a realistic estimate of the timing of the events. . . . 13
3.1 proof-of-concept experimental setup; (a): CSF-mimicking liquids; (b) multi-tissue anthropomorphic head phantom, on the side four antennas are placed, the CSF liquid can be poured from the aperture, a clamp closes/opens the tube to flush the fluid; (c) vector network analyzer; (d) central processing unit. . . . 24
3.2 Relative permittivity of the synthetic CSF formulations. The graphs illustrate the properties of the five manufactured mixtures, distinguishing between the healthy mimic and the four pathological variants. The dashed red line indicates the literature reference value for healthy human CSF. . . . 25
3.3 Conductivity of the synthetic CSF formulations. The graphs illustrate the properties of the five manufactured mixtures, distinguishing between the healthy mimic and the four pathological variants. The dashed red line indicates the literature reference value for healthy human CSF. 26
3.4 Sensors used in the proof-of-concept MWS system: left: schematic with the main dimensions in mm; right: antenna picture. . . . 27
3.5 Reflection parameters of the four antennas when put on the surface of the phantom filled with the healthy CSF-mimicking liquid . . . 28
4.1 Schematic of the microwave sensing system including the VNA, the custom antenna array, and the head phantom. . . . 34
4.2 Circular monopole antenna design: (a) geometrical layout and (b) the realized prototype used in the array. . . . 35
4.3 Modeled power density distribution (dBW/m^2) inside a block of layered tissues at 0.5, 3.5, and 6.5 GHz. The striped layer denotes the location of the CSF. . . . 35

4.4 Measured scattering parameters on the six antennas on the phantom: (a) Reflection coefficients and (b) Transmission coefficients grouped by antenna distance. Short distances are highlighted using green dotted lines, whereas medium and long distances are marked with blue and red dashed lines. Additionally, a diagram in the corner illustrates the geometric placement of the antennas on the phantom. 36
4.5 Measured dielectric properties of the materials used to create the phantom: (a) permittivity and (b) conductivity. 37
4.6 Measured dielectric properties of the created liquids that mimic CSF: (a) permittivity and (b) conductivity. 38
4.7 The printed fat-mimicking part of the phantom. The tube used to empty the CSF gap is attached to the inner part. 39
4.8 The anthropomorphic head phantom: (a) assembled view, (b) external shell, and (c) internal brain core. 40
4.9 Protocol scheme for one measurement cycle. 41
4.10 Data augmentation. (a) Original array configuration, and (b) flipped configuration. 42
4.11 Graphical representation of the two data divisions. 43
4.12 PCA analysis. (a) Real and imaginary parts; (b) module only. 45
4.13 MLP confusion matrices. for the multi-class classification with four pathological classes, using the module of the scattering parameters as dataset features. A darker color indicates a higher value.(a) DD1, 60:40 (%); (b) DD2, 70:30 (%). 51
4.14 MLP confusion matrices for the multi-class classification with two pathological classes, using the module of the scattering parameters as dataset features. A darker color indicates a higher value. (a) DD1, 60:40 (%); (b) DD2, 70:30 (%). 51
6.1 Dielectric properties ε_r (blue) and σ (orange) of water across a 25°C to 50°C range. Data points are derived from the Debye model at discrete frequency intervals. All results show a linearity coefficient $R^2 > 0.985$. 65
6.2 Frequency dependent relative deviation between Debye predictions and empirical data. (a) Maximum error for conductivity. (b) Maximum error for relative permittivity. 66
6.3 Dielectric characteristics of deionized water as a function of thermal state. (a) Conductivity results. (b) Relative permittivity results. 67
6.4 Experimental system architecture: (left) Vector network analyzer integration. (right) Geometric antenna distribution within the phantom boundaries. The target coordinate for the dielectric contrast is indicated by the red marker. Grid units are in mm. 69
6.5 Extended gap ridge horn antenna architecture: (a) Isometric 3D view. (b) Longitudinal cross section. (c) Aperture front view. 70

6.6 Measured reflection coefficients of the sensors immersed in water at 25°C: (a) Magnitude response. (b) Phase response. 70
6.7 Measured transmission coefficients between antenna pairs in water at 25°C: (a) Magnitude response. (b) Phase response. 71
6.8 Phase center reconstruction: The simulated position of the phase center relative to the antenna aperture is indicated by the blue curve with circular markers, while the red curve with triangular markers shows the corresponding polynomial fit. Representative top-view maps of the electric field distributions employed for the phase center estimation are reported at 0.8 GHz and 2.0 GHz. 72
6.9 Experimental phantom utilized for system validation: (a) The empty PLA structure prior to VNA integration. (b) The fully assembled and water-filled system during data acquisition. External stabilizing strips were utilized to maintain the vertical alignment of the Teflon target. . . 75
6.10 Measurement protocol for the PD experiment: hot water (40.5°C) is poured in the target tube and each time a 0.1°C decrease is detected the S-parameters are recorded. 77
6.11 Frequency analysis regarding differential transmission scattering parameters. Data reliability decreases above 2 GHz, necessitating the use of the 0.5 to 2 GHz band for imaging. (a) Magnitude. (b) Phase. 78
6.12 Differential reconstruction comparing an air filled target against a water background. The magenta circle denotes the actual target site, which is correctly identified by the algorithm. 78
6.13 Reconstructed differential maps for temperature gradients ΔT between 0.1°C and 0.9°C. The target location is highlighted with a magenta circle in all frames. 79
6.14 Quantitative reconstruction metrics: (a) spatial offset between the reconstructed peak and the true target center versus ΔT; (b) peak magnitude as a function of ΔT including a linear regression fit. The R^2 value is provided in the inset. 80

Chapter 1

Introduction

1.1 Principles of Microwave-Based Techniques

The interaction between microwaves and matter provides a powerful means of probing material composition in a non-invasive and non-ionizing way. Over the past few decades, microwave-based methods have attracted growing attention due to their ability to sense dielectric contrast, offering complementary information to other imaging modalities. Because they use low-power electromagnetic waves, these techniques are safe, cost-effective, and suitable for compact and portable implementations. As a result, they have found applications across diverse areas, from industrial monitoring to biomedical diagnostics, where understanding local dielectric behavior is essential [1, 2].

Microwaves are generally defined as electromagnetic waves in the frequency range between 300 MHz and 300 GHz. According to the International Telecommunication Union (ITU) Radio Regulations, this spectral region is subdivided into three main bands: the Ultra High Frequency (UHF) band spanning 300 MHz–3 GHz, the Super High Frequency (SHF) band covering 3–30 GHz, and the Extremely High Frequency (EHF) band ranging from 30–300 GHz [3]. The latter corresponds to the so-called millimeter-wave region, characterized by wavelengths between 10 mm and 1 mm. In microwave engineering, it is also usual to adopt the IEEE Standard 521-2002 radar-frequency band nomenclature, which partitions the microwave and millimeter-wave ranges into finer sub-bands (L, S, C, X, Ku, K, Ka, V, W, D), widely used in antenna design, radar, and microwave imaging applications [4]. The two classifications are complementary: the ITU bands, shown in Table 1.1, provide a regulatory and global framework, whereas the IEEE letter bands, shown in Table 1.2, offer a practical engineering-oriented subdivision for system design and frequency allocation.

Microwave-based diagnostic methods typically operate in the UHF band according to the ITU classification, or within the L- and S-bands in the IEEE nomenclature. These frequency regions provide a practical compromise between spatial resolution, which

Band	Frequency Range	Metric subdivision
UHF	300 MHz – 3 GHz	Decimetric region
SHF	3 GHz – 30 GHz	Centimetric region
EHF	30 GHz – 300 GHz	Millimetric region

Table 1.1: ITU/IEC frequency band classification within the microwave range.

Band	Frequency Range	Wavelength Range
L-band	1–2 GHz	30–15 cm
S-band	2–4 GHz	15–7.5 cm
C-band	4–8 GHz	7.5–3.75 cm
X-band	8–12 GHz	3.75–2.5 cm
Ku-band	12–18 GHz	2.5–1.7 cm
K-band	18–27 GHz	1.7–1.1 cm
Ka-band	27–40 GHz	11–7.5 mm
V-band	40–75 GHz	7.5–4 mm
W-band	75–110 GHz	4–2.7 mm
D-band	110–170 GHz	2.7–1.7 mm

Table 1.2: IEEE Standard 521-2002 radar-frequency band nomenclature.

improves at higher frequencies, and penetration depth, which increases at lower frequencies. Nevertheless, certain microwave diagnostic techniques may exploit higher-frequency bands when enhanced resolution or specific electromagnetic interactions are required.

All these technologies rely on the sensitivity of electromagnetic fields to the dielectric properties of materials. The response of a sample exposed to microwaves depends on its complex permittivity ε_r, defined as:

$$\varepsilon_r = \varepsilon_r' - j\varepsilon_r'', \tag{1.1}$$

where ε_r', the real part, is also known as the dielectric constant of the material, or the relative permittivity, and describes how well a material stores electric energy through polarization, and ε_r'', the imaginary part, characterizes the losses and is related to the equivalent conductivity σ of the material through the formula:

$$\varepsilon_r'' = \frac{\sigma}{\omega\varepsilon_0}, \tag{1.2}$$

where ω is the angular frequency and ε_0 is the vacuum permittivity. This complex permittivity is not the same for every frequency, the frequency-dependent behavior of materials can be described using dispersion models. The Debye model provides a simple

but effective representation of how permittivity varies with frequency. The order 1 Debye model expresses the complex permittivity as:

$$\varepsilon_r(\omega) = \varepsilon_\infty + \frac{\varepsilon_s - \varepsilon_\infty}{1 + j\omega\tau}, \tag{1.3}$$

where ε_s is the static permittivity, ε_∞ is the permittivity at infinite frequency, and τ is the relaxation time associated with molecular dipole rotation. This formulation captures the characteristic dispersion and absorption mechanisms arising from dipolar relaxation in biological media [5].

While the Debye model offers a good approximation for simple materials as single-component liquids, more complex tissues are usually better described by the Cole-Cole model [6]. The Cole-Cole model extends the Debye representation to account for the distribution of relaxation times typically observed in complex biological tissues. The complex permittivity in the Cole-Cole model is expressed as:

$$\varepsilon_r(\omega) = \varepsilon_\infty + \frac{\varepsilon_s - \varepsilon_\infty}{1 + (j\omega\tau)^{1-\alpha}}, \tag{1.4}$$

where α is an empirical constant that ranges from 0 to 1. This exponent describes the broadening of the relaxation peak, which reflects the structural heterogeneity of the medium. If α is equal to zero, the equation becomes the order 1 Debye model.

Changes in complex permittivity alter the transmission and the scattering of microwaves. In microwave-based systems, the transmitted wave carries information about the material it has crossed, because its amplitude and phase are modified according to the losses and dielectric properties encountered along the path. Scattering, instead, describes the process by which an incident electromagnetic wave is redirected as a consequence of spatial variations in the dielectric properties of a medium. Whenever a wave encounters an inhomogeneity in permittivity, part of the energy is re-radiated in different directions. This scattered field carries information about the location, size, and contrast of those dielectric inhomogeneities. By exploiting these principles, it becomes possible to detect or map variations in permittivity and conductivity, enabling both microwave sensing and microwave imaging applications.

1.1.1 Scattering Parameters and Vector Network Analyzers

Microwave-based systems are commonly characterized through their response to incident electromagnetic waves. A practical and widely adopted instrument for this purpose is the Vector Network Analyzer (VNA). A VNA generates a known microwave signal, injects it into the device under test (DUT), and measures how the system modifies the amplitude and phase of the resulting electromagnetic waves. Accurate microwave measurements require proper calibration of the VNA to remove the systematic errors introduced by cables, connectors, and measurement fixtures. Calibration effectively

shifts the reference plane to the input of the DUT, ensuring that the measured scattering parameters reflect only the DUT response. Common calibration techniques include Short–Open–Load–Thru (SOLT), which is widely used for coaxial measurements, and Thru–Reflect–Line (TRL), which is preferred for waveguide or planar structures where ideal standards are difficult to realize. A good calibration is essential to obtain reliable and repeatable measurements, particularly when small dielectric variations must be resolved. A VNA operates by sequentially exciting each port of a multi-port setup with a calibrated incident signal. For every excitation, the instrument measures the waves emerging from all ports, capturing both magnitude and phase. These measurements are expressed in terms of scattering parameters, which form the scattering matrix.

Scattering parameters, commonly referred to as S-parameters, quantify how an incident electromagnetic wave is distributed across the various ports of a device, indicating the fractions of power that are reflected, transmitted, or coupled between ports. Each S-parameter is identified by the letter S followed by two indices. The second index denotes the port where the signal is injected, while the first indicates the port from which the response is measured. For example, in the simplest case of a two-port device, four fundamental parameters fully characterize its behavior:

- S_{11} quantifies the reflection at port 1, indicating the ratio between the reflected and incident waves.
- S_{21} represents the transmission coefficient that describes how efficiently power injected at port 1 is transferred to port 2.
- S_{12} represents the transmission from port 2 to port 1. For reciprocal structures, such as those typically used in microwave imaging, one expects $S_{12} = S_{21}$. Any noticeable difference between the two generally arises from measurement or calibration inaccuracies rather than from the physics of the system.
- S_{22} is the reflection coefficient at port 2, quantifying the ratio between the reflected and incident waves at that port.

Because microwave signals exhibit both amplitude and phase variations, each S-parameter is a complex quantity. The magnitude provides information about the fraction of power involved in reflection or transmission, whereas the phase reveals how the wave is shifted as it propagates through the network.

For an N-port structure, all the S-parameters can be arranged in an $N \times N$ scattering matrix, where the element S_{ij} represents the response at port i to an excitation at port j. For instance, for a four-port system at a single frequency point, the scattering matrix can be written as

$$\mathbf{S} = \begin{bmatrix} S_{11} & S_{12} & S_{13} & S_{14} \\ S_{21} & S_{22} & S_{23} & S_{24} \\ S_{31} & S_{32} & S_{33} & S_{34} \\ S_{41} & S_{42} & S_{43} & S_{44} \end{bmatrix}, \tag{1.5}$$

where the diagonal elements S_{ii} denote the reflection coefficients at each port, while the off-diagonal elements S_{ij} ($i \neq j$) correspond to the transmission coefficients between different ports.

This matrix-based description offers a complete representation of the inter-port interactions, capturing both the strength and the phase of the wave transformations occurring within the device. The VNA collects these coefficients across a defined frequency range, producing a $N \times N$ scattering matrix for each frequency point.

Variations in the complex permittivity ε influence the phase velocity and attenuation of the waves, thereby affecting the coefficients, which carry the information about the cumulative phase delay and losses along the path between the two ports. When multiple contrasts are present within the medium, their individual scattered contributions superimpose, and the resulting interference pattern becomes embedded in the structure of the measured scattering matrix. Through this mechanism, S-parameters provide an indirect representation of the underlying dielectric distribution. They form the basis of both microwave sensing (MWS), which aims to extract global or local properties from selected S-parameter features, and microwave imaging (MWI), where an inversion algorithm reconstructs the location and intensity of dielectric contrasts from multi-frequency scattered data.

1.1.2 Microwave Sensing

Microwave sensing is the use of electromagnetic waves in the microwave range to detect the presence of objects or to gather information about an environment. The goal is not to locate a dielectric contrast, but rather to assess its presence or to quantify its magnitude.

Microwave sensing can be passive or active:

- **Passive:** the naturally emitted microwave radiation of a target is detected by one or more sensors.
- **Active:** one or more sensors inject electromagnetic energy in the target and analyzes its response.

Passive microwave sensing relies on measuring the natural microwave emission of the target. For this reason, the two approaches provide fundamentally different types of information: passive radiometers retrieve brightness temperature, which depends on the emissivity and temperature of the material, whereas active systems measure amplitude and phase modifications of the incident wave, enabling the extraction of dielectric contrast and structural information. In this work, we focus on active MWS.

Small perturbations in the electromagnetic properties of the target typically manifest as measurable variations in specific scattering parameters. For instance, changes in the complex permittivity may produce detectable shifts in the reflection coefficient S_{11}. Similarly, phase delays in transmitted or reflected signals can reveal subtle variations

in propagation paths or dielectric contrasts within the medium. In resonant structures, for example, the presence of a perturbation can be detected by observing a resonance frequency shift. These metrics, including reflection coefficient variations, phase deviations, and resonance shifts, serve as sensitive indicators of dielectric changes and form the basis for many microwave sensing and imaging techniques.

1.1.3 Microwave Imaging

The objective of microwave imaging techniques is to spatially locate the dielectric contrasts inside an explored region of interest (ROI). Typically, an algorithm reconstructs the spatial map of the dielectric properties of an area, together with their magnitude. In a typical microwave imaging system, an array of antennas sequentially illuminates the target and records the scattered fields across a range of frequencies. MWI systems can operate in mono-static or multi-static configurations: in the first, each antenna acts as both transmitter and receiver, providing reflection data, while in the latter each transmitting antenna is paired with multiple receiving antennas, yielding a richer matrix that includes transmission parameters and thereby improves imaging performance at the cost of a more complex configuration.

The imaging process relies on an inverse scattering algorithm, which interprets these measured fields by estimating the permittivity distribution that best explains the observed data under Maxwell's equations. Reconstructing an image from the measurements requires solving an inverse scattering problem, which is inherently non-linear due to multiple interactions inside the domain of interest. To handle this complexity, imaging algorithms fall into three broad categories:

- **Linearized methods**: rely on approximations that simplify wave interactions and are suited for qualitative shape reconstruction.
- **Radar-based approaches**: focus on locating dominant scatterers with high computational speed.
- **Quantitative techniques**: use iterative solvers together with full-wave electromagnetic models to recover absolute dielectric values.

The choice of the operating frequency band, the antenna topology, and the reconstruction strategy depends on the desired resolution, penetration depth, and complexity of the imaging scenario.

1.2 The Uses of Microwave Imaging and Sensing

Microwave-based techniques have been successfully applied in a wide range of fields for non-destructive evaluation, process monitoring, and quality control. In structural

and civil engineering, microwaves have been used to assess moisture content, detect internal defects, and characterize layered structures. For instance, microwave reflection and transmission measurements have been employed to infer water content and estimate the thickness of concrete elements [7, 8], while other studies demonstrated their capability to identify delamination, voids, and porosity in composite materials difficult to examine using more conventional non-destructive techniques [9]. In agriculture and food quality assessment, microwave sensors provide fast, non-invasive evaluation of moisture levels, ripeness, adulteration, or contamination in packaged products. Examples include the detection of foreign objects in food jars using microwave signals and machine learning [10, 11], and the assessment of spoilage or compositional changes in liquids such as milk via microwave resonance shifts [12, 13]. These techniques enable real-time monitoring and support industrial quality control without damaging the product. Microwave-based methods are also valuable in industrial process control. Real-time monitoring of multiphase flows, such as measuring water fraction and salinity in pipelines, has been achieved using microwave sensors [14, 15]. Similarly, microwave tomography has been used to track moisture distribution in industrial drying systems [16]. In geophysical and heritage applications, radar-based microwave techniques support subsurface characterization for archaeology, mineral exploration, and soil stratigraphy [17, 18].

Across these diverse applications, the advantages of microwave sensing and imaging are clear: microwaves penetrate opaque media, respond sensitively to dielectric contrasts, and can operate at low power, allowing fast, non-destructive, and potentially real-time measurements. The wide-ranging applications of microwave-based techniques highlight their versatility, sensitivity to material properties, and non-invasive nature. These same advantages make microwaves particularly attractive for biomedical applications, where safety, non-ionizing operation, and the ability to probe opaque or complex tissues are critical.

1.3 Medical Applications

Microwave radiation has several characteristics that make it particularly appealing for biomedical applications. First, waves in the GHz range can traverse tissues that are opaque to visible light, allowing them to probe regions that other modalities cannot easily access. Their interaction with biological tissues is strongly dependent on the local dielectric properties, which depend on factors such as water content, cellular structure, protein concentrations, and other physiological alterations. As a consequence, healthy and pathological tissues respond differently when illuminated by microwaves, enabling contrast mechanisms that complement techniques like ultrasound, X-ray imaging, or magnetic resonance imaging (MRI).

Another appealing aspect of microwave technology in medicine is its inherently safe nature. Microwaves are non-ionizing and can operate at very low power levels,

allowing for frequent, repeated, or even continuous monitoring without exposing the patient to harmful doses. This characteristic is of particular relevance in long-term follow-up, bedside monitoring, or the surveillance of chronic conditions.

The first introduction of microwave-based diagnostics into the medical domain dates back to the 1980s. Early work focused mainly on non-invasive dosimetry and feasibility studies [19]. Over the years, substantial technological advances, including the availability of efficient full-wave solvers, compact and low-cost VNAs, and improved computational reconstruction algorithms, enabled the exploration of more sophisticated biomedical applications.

Among the most established medical applications is breast cancer detection. Numerous studies have demonstrated the potential of microwave imaging systems to detect lesions by exploiting the dielectric contrast between malignant and healthy breast tissues [20, 21, 22, 23, 24]. Research in this domain has evolved from early proof-of-concept systems to more advanced setups featuring multistatic antennas, realistic breast phantoms, and supervised machine-learning approaches to enhance detection performance.

A second extensively explored application concerns brain imaging, particularly for stroke detection and monitoring. Microwave-based head imaging aims to differentiate ischemic from hemorrhagic strokes by measuring local variations in dielectric properties, an important capability, as the two conditions require opposite treatments. Several prototype systems and clinical-oriented studies have shown promising results in real-time monitoring and classification [25, 26, 27].

Beyond oncology and stroke, microwaves have also been investigated for other biomedical and physiological monitoring tasks. These include non-invasive glucose sensing through resonant or metamaterial-based probes [12, 13], the monitoring of brain atrophy in neurodegenerative diseases using wearable RF devices [28], and the use of radar-based microwave measurements combined with deep learning for Alzheimer's disease monitoring [29]. A growing line of research also aims at detecting brain tumors using compact antennas and metamaterial-loaded arrays [30, 31].

Overall, the versatility of microwave-based techniques, ranging from wideband imaging systems to narrowband resonant sensors, positions them as a powerful family of tools for biomedical diagnostics.

1.4 Motivation and Thesis Outline

In this thesis, I describe my research work about the application of microwave-based techniques to achieve early detection of Alzheimer's disease and Parkinson's disease. The global prevalence of these illnesses continues to rise, driven by aging populations and increased life expectancy. Despite significant progress in clinical research, early-stage diagnosis remains substantially limited: current neuroimaging modalities detect

structural or metabolic alterations only when neuronal degeneration is already well advanced, while biomarker-based methods are either invasive, costly, or difficult to standardize in routine healthcare. As a consequence, patients often begin treatment at a stage in which therapeutic interventions can no longer halt or reverse the progression of the disease. The scientific and clinical community faces a need for diagnostic tools capable of detecting the earliest physiological changes, ideally before symptom onset, that is also suitable for mass-screening.

Microwave-based techniques offer a promising opportunity in this direction. Electromagnetic waves in the microwave band are sensitive to the dielectric properties of biological tissues, reacting to their composition, water content, and cellular structure. Several studies have shown that pathological processes such as demyelination, inflammation, edema, or protein accumulation induce measurable dielectric contrasts. For Alzheimer's disease, the altered composition of cerebrospinal fluid (CSF), in particular the reduction of permittivity due to increased protein concentration, has been suggested as a potential early biomarker. In the case of Parkinson's disease, emerging evidence highlights microstructural changes in the substantia nigra, including glial scarring, which may also manifest as electromagnetic contrasts. Microwave measurements are non-ionizing, inexpensive, and compatible with compact instrumentation, making them an attractive candidate for new diagnostic strategies.

The motivation of this thesis is to assess whether microwave-based methods, combined with machine-learning approaches, can detect the subtle dielectric variations associated with the early stages of Alzheimer's and Parkinson's diseases. Instead of pursuing full tomographic reconstruction, the work focuses on identifying measurable scattering signatures and learning discriminative patterns directly from experimental data. To this end, two complementary technological frameworks are explored: microwave sensing, based on multi-antenna S-parameter measurements and classification algorithms; and microwave imaging, implemented through a multi-frequency bi-focusing algorithm to localize dielectric anomalies. Experimental phantoms are designed to reflect realistic physiological conditions, enabling a systematic investigation of detectability limits, robustness against noise, and the overall feasibility of the proposed approach.

The remainder of the thesis is organized as follows:

- Chapter 2 provides an overview of Alzheimer's disease, including its pathophysiology, diagnostic workflow, and current research efforts in early detection. It also introduces previous microwave-based studies and discusses their relevance to the present work.

- Chapter 3 presents the proof-of-concept study, in which the feasibility of microwave sensing for the early detection of Alzheimer's disease is investigated using a limited number of antennas and a pre-existing experimental phantom. The results obtained in this phase have been presented in [32, 33, 34].

- Chapter 4 introduces the complete microwave sensing framework developed for

early Alzheimer's disease detection. The chapter details the antenna system design, phantom fabrication, dataset construction, and the associated machine-learning pipeline. Experimental results are reported and critically discussed, these findings have been published in [35].

- Chapter 5 shifts the focus to Parkinson's disease, summarizing the clinical characteristics, existing early-diagnosis strategies, and potential opportunities for microwave techniques.
- Chapter 6 introduces a microwave imaging methodology designed for Parkinson's-related dielectric alterations, covering the phantom design, measurement system, and the multi-frequency bi-focusing reconstruction algorithm, including simulation-based validation and experimental demonstrations. The results of this work have been published in [36, 37].
- Finally, Chapter 7 concludes the thesis by summarizing the main contributions, outlining current limitations, and discussing future directions for microwave-based neurodiagnostics.

Chapter 2

Alzheimer's Disease

2.1 Overview of Alzheimer's Disease and Risk Factors

Alzheimer's disease (AD) represents the most common cause of dementia worldwide and poses one of the greatest global public health challenges of the 21st century. AD is a chronic, progressive neurodegenerative disorder and is characterized by a long asymptomatic phase during which molecular and structural brain alterations gradually accumulate before clinical symptoms emerge. The disease primarily affects memory, executive functions, and daily life autonomy, leading to a progressive decline that has profound consequences on patients, families, and the healthcare system [38, 39].

The risk of developing AD arises from a complex interplay of factors. Some of these factors are non modifiable and depend on genetic factors, while other depend on habits and lifestyle. Among the most important non modifiable factors are increasing age, which remains the strongest single predictor, and genetic predisposition, in particular the presence of the *APOE* $\epsilon 4$ allele, which is associated with a significantly higher hazard ratio for AD compared to non carriers [40]. A family history of dementia also contributes to increased risk, even though the majority of AD cases are sporadic rather than familial [41]. In addition to these inherent risks, a number of modifiable factors have been linked to higher AD probability. Vascular and metabolic conditions such as hypertension, type-2 diabetes mellitus, elevated LDL cholesterol, obesity, and other cardiovascular diseases increase risk likely via mechanisms involving impaired cerebral perfusion, chronic inflammation, and metabolic dysregulation [42, 43]. Lifestyle factors further modulate risk: physical inactivity, smoking, excessive alcohol consumption, poor diet, low educational attainment and limited cognitive/social stimulation have all been associated with increased AD and dementia incidence [44]. Emerging evidence also highlights sensory impairments, usually hearing loss and untreated vision loss, as important and potentially modifiable risk factors. This is because sensory deprivation may reduce cognitive reserve and increase social isolation [45]. Sleep disorders, such as obstructive sleep apnea, may additionally contribute to risk by impairing brain maintenance mechanisms during sleep [46].

Moreover, environmental and other medical risk factors have been proposed. Chronic exposure to air pollution and aggregated vascular/metabolic stress, as well as a history of traumatic brain injury or repeated head trauma, may further elevate AD risk, through neuroinflammatory pathways or by exacerbating vascular damage [47]. Psychological factors such as depression, social isolation, and long term stress have also been associated with higher incidence of dementia, underscoring the role of overall lifestyle, mental health, and social context in modulating susceptibility [48].

Because many of these risk factors are modifiable, interventions at the level of public health, lifestyle changes, and early prevention strategies may meaningfully reduce the incidence or delay the onset of Alzheimer's disease, making the identification of such risks a fundamental step in AD research and care policy.

2.1.1 Clinical Symptoms, Disease Progression and Physiological Changes

Alzheimer's disease manifests through a spectrum of cognitive, behavioral, and physical symptoms that gradually impair daily functioning. Cognitive deficits typically appear first, often as memory loss, particularly affecting recent events or conversations, coupled with difficulty in planning, solving problems, or completing familiar tasks [49, 38]. Patients may become disoriented in time or space, struggle to interpret visual or spatial information, and face challenges with language, such as difficulties speaking or trouble following conversations [39]. Executive dysfunction and impaired judgment further hinder decision making and the ability to manage finances or navigate complex tasks [50]. Beyond cognition, behavioral and psychological changes frequently occur, including shifts in personality, mood disturbances such as depression or irritability, social withdrawal, and a loss of initiative in previously enjoyed activities [51]. Agitation, aggression, delusions, hallucinations, and sleep disturbances, including insomnia, daytime somnolence, and sundowning, may also emerge [52]. Physical and functional deterioration follows, with coordination and mobility difficulties, loss of bladder or bowel control, impaired swallowing, and weight loss becoming apparent, especially in advanced stages [38, 50]. Patients may also experience disorientation to familiar environments, repetitive behaviors or speech, and difficulty recognizing familiar faces [51]. Collectively, these symptoms illustrate the progressive nature of Alzheimer's disease, from subtle cognitive decline to profound impairment in independence and daily living, highlighting the multifaceted challenges faced by patients and caregivers.

Over time, the disease progresses from preclinical AD to mild cognitive impairment (MCI), and ultimately to dementia, where cognitive decline significantly interferes with daily activities. The long preclinical phase is estimated to last 10 to 20 years and is particularly relevant for early detection efforts. During this period, changes in brain physiology and biochemistry accumulate gradually, offering a potentially actionable window for detection before symptoms [53, 54]. As Figure 2.1 summarizes, the first detectable physiological sign of pathology is a change in the concentration of amyloid-beta (Aβ)

in the cerebrospinal fluid (CSF), typically a decrease in CSF $A\beta_{42}$ (or $A\beta_{42}/A\beta_{40}$ ratio), reflecting the transformation of $A\beta$ into insoluble aggregates in the brain. This process linked to the formation of extracellular $A\beta$ plaques, one of the main brain biomarkers linked to AD [55, 56]. This amyloid pathology often appears 15 to 20 years before clinical symptoms. As amyloid pathology advances, alterations in tau metabolism follow: levels of phosphorylated tau (p-tau) and total tau (t-tau) in CSF increase, corresponding to the accumulation of intracellular neurofibrillary tangles, another cardinal AD biomarker [57]. After these molecular changes, neurodegenerative processes begin: synaptic dysfunction, neuronal loss, axonal injury, and brain atrophy become detectable [58, 59]. Only once neurodegeneration has progressed sufficiently do cognitive impairment and the classical clinical symptoms of AD typically start to manifest.

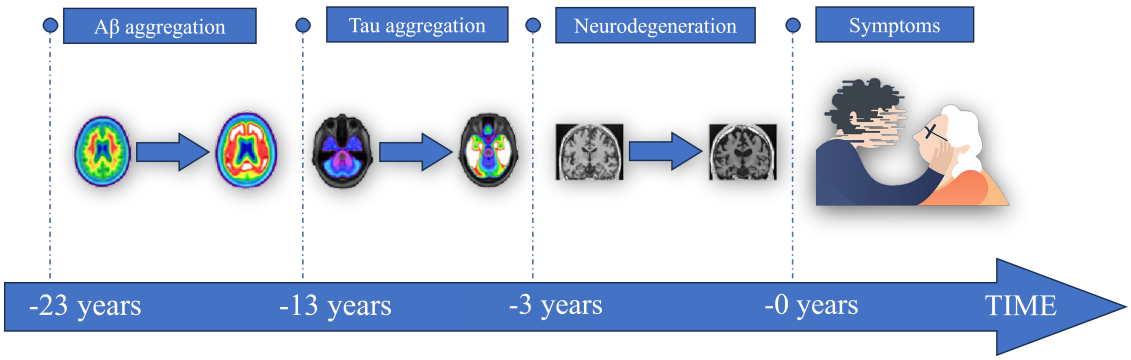

Figure 2.1: Alzheimer's dieasease progression with a realistic estimate of the timing of the events.

2.1.2 Epidemiology and Global Impact

According to the World Health Organization, more than 55 million people are currently living with dementia, and Alzheimer's disease accounts for 60%–70% of these cases [39]. With the progressive ageing of the global population, this number is expected to triple by 2050, becoming one of the primary public health challenges of the century.

The socioeconomic impact is enormous: AD leads to long term disability, dependency, and high healthcare and caregiving costs. The burden is particularly heavy on informal caregivers who experience substantial psychological, physical, and financial stress.

The results summarized in Table 2.1 highlight the growing macroeconomic impact of Alzheimer's disease and other dementias (ADODs) on societies worldwide [60]. Using a macroeconomic model that integrates labour supply reductions, morbidity, mortality, and care related economic diversion, the study estimates that ADODs will impose a cumulative global cost of more than 14 trillion dollars between 2020 and 2050. This corresponds to approximately 0.4% of the annual global GDP, underscoring dementia

as one of the most economically consequential chronic diseases of the century. In absolute terms, the greatest economic losses are projected for China, the United States, and Japan, reflecting their large ageing populations. These losses stem not only from direct medical and long term care expenditures but also from reductions in productive labour due to both patient disability and the unpaid caregiving responsibilities carried predominantly by family members.

The structure of the economic burden also differs markedly by income level. In lower-middle-income countries, up to 85% of the total cost is attributable to informal care, indicating a heavy reliance on family members rather than formal healthcare systems. In contrast, high-income countries show a more balanced distribution of costs, with informal care accounting for around 61%, and treatment plus formal care services representing nearly 31% of the total economic burden. This disparity reflects differences in healthcare infrastructure, social support networks, and demographic transitions between countries.

Finally, the table contextualizes these financial estimates within global demographic trends. The number of people living with dementia is projected to increase to more than 153 million by 2050, driven largely by population ageing. These epidemiological dynamics, combined with the substantial macroeconomic effects outlined above, emphasize the urgency of developing scalable strategies for early detection, risk reduction, and long term care planning to mitigate the future burden of ADODs.

Category	**Main Findings**
Population Impact	People living with dementia: • 2019: 57 million • 2050 (projected): 153 million
Global Economic Burden (2020–2050)	Total cost: $ 14 513 billion
Country Level Burden (2020-2050)	• China: $ 2 961 billion • USA: $ 2 331 billion • Japan: $ 1 758 billion
Informal care burden	• High-income countries: 61% • Lower-middle-income countries: 85%

Table 2.1: Key Findings from the Macroeconomic Burden Analysis of Alzheimer's Disease and Other Dementias (ADODs) [60]

Early detection would significantly reduce this burden by enabling timely interventions, lifestyle modifications, and planning of care pathways. However, despite its importance, current diagnostic tools typically detect AD only after significant neuronal loss has already occurred.

2.2 Diagnosis

The diagnosis of AD relies on an integrated approach combining clinical evaluation, cognitive assessment, neuroimaging, and laboratory biomarkers. Modern diagnostic frameworks follow criteria which incorporate both clinical symptoms and biological evidence such as amyloid and tau pathology [49, 61].

2.2.1 Clinical Examination and Symptom Based Diagnosis

The clinical evaluation of Alzheimer's disease begins with a detailed medical history and structured interviews with both the patient and their close contacts, usually family members. These discussions help contextualize cognitive complaints and functional decline, providing insight into changes in daily behavior, habits, and routines. Neuropsychological testing plays a central role, assessing cognitive domains including episodic memory, language, attention, executive functions, and visuospatial abilities. Functional evaluations complement these tests by examining the patient's ability to perform activities of daily living and maintain independence.

Several standardized assessment tools are commonly employed to quantify cognitive impairment and stage disease severity. Among the most widely used are the Mini-Mental State Examination (MMSE) [62], the Montreal Cognitive Assessment (MoCA) [63], the Clinical Dementia Rating (CDR) [64], the Addenbrooke's Cognitive Examination III (ACE-III) [65] and the Rowland Universal Dementia Assessment Scale (RUDAS) [66]. A summary of these tools is presented in Table 2.2. Each instrument targets specific cognitive domains and functional capacities, providing a structured framework for diagnosis and monitoring of Alzheimer's disease progression.

While symptom based diagnosis is non invasive and widely accessible, it is inherently limited: it primarily identifies the disease at the stage of overt dementia, when structural and neuronal damage is already significant.

2.2.2 Imaging and Laboratory Tests Used in AD

The National Institute on Aging and the Alzheimer's Association have proposed the ATN framework [67] to provide a unifying rationale for the large number of non-symptom-based diagnostic methods described below. This framework defines three biomarkers categories for AD: amyloid pathology (A), tau pathology (T), and neurodegeneration (N), and combines them to have an enhanced diagnostic accuracy. These biomarkers are related to the same physiological changes previously discussed in this chapter. The current technologies able to detect these biomarkers are the following:

- **Structural and microstructural MRI:** magnetic resonance imaging (MRI) is able to detect hippocampal and medial-temporal atrophy, useful to predict the progression from MCI to AD dementia. Voxel based morphometry (VBM) and

Tool	Domains Assessed	Scoring / Interpretation
MMSE [62]	Orientation, registration, attention, calculation, recall, language, visuospatial	0–30 ($\geq$24 $\longrightarrow$ normal)
MoCA [63]	Attention, executive functions, memory, language, visuospatial skills, orientation	0–30 ($\geq$26 $\longrightarrow$ normal)
CDR [64]	Memory, orientation, judgment, problem solving, community affairs, hobbies, personal care	0–3 (0 = none, 0.5 = very mild, 1 = mild, 2 = moderate, 3 = severe)
ACE-III [65]	Attention, memory, verbal fluency, language, visuospatial abilities	0–100 (higher = better; <88 often indicates cognitive impairment)
RUDAS [66]	Memory, executive function, language, visuospatial, reasoning	0–60 (higher = better; cut-offs vary by age and education)

Table 2.2: Standardized cognitive and functional assessment protocols for Alzheimer's disease

subfield hippocampal analyses refine regional sensitivity, while diffusion MRI reveals microstructural white matter disruption that may appear early in the disease course. Structural MRI is essential to identify AD typical atrophy patterns and to exclude alternative structural causes of cognitive decline.

- **Molecular PET imaging (amyloid, tau, and synaptic PET):** molecular PET imaging enables direct in vivo visualization of AD protein pathology. Amyloid PET tracers identify Aβ plaques and tau PET tracers map neurofibrillary tangles. More recently, PET tracers have been developed to quantify synaptic density, offering a direct measure of synaptic loss that may provide additional staging and prognostic value.

- **Functional and metabolic imaging (fMRI, FDG-PET, SPECT):** functional MRI (resting state and task based) detects alterations in network connectivity, a finding that often precedes atrophy. FDG-PET measures regional cerebral glucose metabolism and highlights the lower metabolism characteristic of AD; FDG patterns can reveal dysfunctions before the structural loss is visible. SPECT perfusion imaging provides lower resolution but more accessible measures of regional blood flow to discover the same dysfunctions. Together, these functional and metabolic modalities complement structural MRI and amyloid/tau PET.

- **Cerebrospinal fluid biomarkers:** CSF analysis remains the standard for AD

diagnosis. The canonical CSF signature comprises decreased Aβ_{42} (or reduced Aβ_{42}/Aβ_{40} ratio) and elevated total tau and p-tau concentrations; this abnormal concentration reflects the formation of amyloid plaques and tau tangles. Additional CSF analytes (neurogranin for synaptic dysfunction, YKL-40 for neuroinflammation, NfL for axonal injury) provide complementary information about disease mechanisms and progression.

- **Blood (plasma) biomarkers:** Recent advances have positioned blood biomarkers as promising tools for AD diagnostics. Ultra sensitive assays for plasma phosphorylated tau proteins show strong concordance with amyloid/tau PET and CSF measures, with p-tau217 emerging as a particularly robust early marker. Additional analytes such as the Aβ_{42}/Aβ_{40} ratio, NfL, and GFAP provide minimally invasive indicators of amyloid pathology, neurodegeneration, and glial activation. Despite this progress, blood biomarkers are not yet ready for routine clinical use since variability across laboratory methods, sensitivity to pre-analytical factors (sample collection, processing, storage), and individual differences (genetics, comorbidities, disease stage) still affect reliability and comparability [68].

In addition to the ATN biomarker classes, a broader set of physiological alterations has been reported across multiple modalities (summarized in Table 2.3). These include metabolic shifts, abnormal cerebral hemodynamics captured by transcranial Doppler [69, 70], microstructural white matter disruption detected by diffusion MRI, and changes in electrophysiological activity such as increased slow wave power and reduced alpha activity in EEG/MEG. PET and SPECT also reveal broader functional abnormalities beyond amyloid and tau, such as hypometabolism, perfusion deficits, and neuroinflammation. Peripheral systems show measurable alterations as well, including oculomotor instability, abnormal pupillary responses, and retinal nerve fiber thinning, all of which point to early involvement of sensory and autonomic pathways. Together, these biomarkers complement the core ATN framework by offering a wider view of brain physiology and by capturing additional dimensions of neurodegeneration and network dysfunction.

Despite rapid progress, several practical limitations remain. MRI is expensive and not always available, making it unsuitable for large scale screening. PET imaging faces the same issue and is also invasive because it requires radioactive tracers. CSF analysis is invasive as well, since it depends on a lumbar puncture performed by trained clinicians. Blood based tests, although promising, still require strict standardization across laboratories and populations before they can be used routinely. Many emerging diagnostic techniques also lack large, diverse validation studies and have not yet received regulatory approval. Overall, factors such as accessibility, cost, and ease of interpretation will determine how quickly and widely each method can be adopted for screening, diagnosis, and monitoring.

Modality	Measured Biomarkers	AD Related Changes
CSF	Aβ42/40 & ratio, t-tau, p-tau, cytokines, isoprostanes, α1-antichymotrypsin	Abnormal Aβ, t-tau, p-tau conc.; ↑ oxidative stress & inflam. markers; enlarged CSF spaces (medial temp.).
Blood	Aβ42/40 & ratio, inflam. proteins, isoprostanes, interleukins, APP frags., ADAM10, BACE1	Amyloid changes; peripheral inflam. & oxidative stress; altered APP-processing enzymes.
CT	Structural imaging	Excludes non AD causes of cognitive decline.
MRI	Grey/White matter integrity metrics	Medial temporal/hippocampal atrophy; signs of small vessel disease.
fMRI	Resting state or task activation	↓ activity in memory networks; compensatory ↑ prefrontal activity.
MRSI	Metabolites: NAA, creatine (Cr), myo-inositol (mI), choline (Cho), Glu	↓ NAA, NAA/Cr, Glu; ↑ mI/Cr, Cho/Cr; reduced neuronal integrity markers.
TCD	Carotid/cerebral hemodynamics	↑ carotid intima–media thickness; ↓ blood flow; impaired vasoreactivity; ↑ pulsatility index.
DTI	White matter microstructure (FA, MD)	↓ fractional anisotropy (FA), ↑ mean diffusivity (MD) indicating White matter damage.
PET	Amyloid, tau, glucose, neuroinflammation	↑ Amyloid/tau tracer uptake; temporoparietal hypometabolism; ↑ inflam. signals.
SPECT	Blood flow and perfusion patterns	↓ perfusion in temporal/parietal cortices; altered CSF dynamics.
MEG/EEG	Spectral and connectivity features	↑ slow wave (delta, theta), ↓ alpha power; ↓ signal complexity & synchrony.
Eye Track.	Oculomotor, fixation, pupil dynamics	Saccades: ↑ latency, ↓ velocity/accuracy; unstable fixation; delayed & ↓ pupil response.

Table 2.3: Overview of physiological biomarkers associated with Alzheimer's disease across different measurement modalities.

2.3 Current approaches for early detection

Early detection of Alzheimer's disease relies on physiological and imaging markers that reveal pathological changes before symptoms appear. Structural and microstructural MRI can detect hippocampal and medial-temporal atrophy as well as early white matter disruption (via diffusion metrics such as increased MD and reduced FA). Functional modalities, including fMRI and FDG-PET, capture early network dysfunction and hypometabolism, while amyloid and tau PET provide direct evidence of protein accumulation in preclinical stages. The list of CSF biomarkers include reduced Aβ_{42} or Aβ_{42}/Aβ_{40} and increased total tau or p-tau. These are among the earliest detectable biochemical indicators, complemented by markers of inflammation and oxidative stress (e.g., interleukin-6, isoprostanes). Blood based biomarkers such as plasma p-tau isoforms, Aβ_{42}/Aβ_{40}, NfL, and GFAP show potential for early detection, although they still require rigorous standardization. Additional modalities also display early alterations: MRSI reveals reduced NAA and increased mI, EEG/MEG show slowing of oscillatory activity and reduced network synchrony, and retinal imaging and eye movement analysis detect early oculomotor and pupillary abnormalities. Transcranial Doppler provides non invasive vascular markers, including reduced cerebral blood flow and impaired vasoreactivity, which have been associated with early disease stages. Together, these approaches form a broad set of non-symptom-based techniques capable of detecting AD related changes well before clinical decline.

In contemporary clinical and research practice, these techniques are combined to increase diagnostic certainty and to stage disease biologically. This multimodal approach supports early detection and accurate differential diagnosis: the use of machine learning applied to multimodal data is being studied to allow a more precise early detection [53]. This motivates the exploration of alternative technologies capable of detecting subtle and different physiological changes before the onset of clinical symptoms.

2.4 Microwave Based Approach to AD Detection

Microwave sensing provides a fundamentally different contrast mechanism compared to conventional neuroimaging, being based on dielectric contrast, an information invisible to other techniques. Instead of relying on structural or molecular biomarkers, microwaves interact with tissues through their dielectric properties, which depend on water content, ionic composition, proteins concentrations, cellular organization, and other factors. Since neurodegenerative processes alter the biochemical and structural characteristics of brain tissues and CSF, dielectric contrasts may emerge even at early disease stages. This idea has motivated initial research efforts exploring whether microwave based measurements could detect early AD related changes.

Recent studies have explored whether microwave sensing and imaging can detect

dielectric alterations associated with Alzheimer's disease (AD). Saied et al. [71] characterized wideband permittivity and conductivity changes in grey and white matter, using these contrasts to model microwave signatures of amyloid and tau pathology. Ullah, Saied and Arslan extended this work by demonstrating that microwave S-parameters collected with wearable antenna arrays can detect macroscopic structural changes such as ventricular enlargement, with both algorithmic analysis [72] and an accompanying open access S-parameter dataset [73] supporting reproducibility. Complementary to these sensing studies, the work by Farhatullah et al. [74] showed that microwave radar scattering coupled with deep learning models can classify AD related patterns. Liu et al. [75] reviewed advanced microwave sensor technologies for permittivity measurements, offering relevant methodological context for future AD oriented systems. Finally, Chen et al. [76] proposed a non-invasive microwave based approach for monitoring Alzheimer's disease using realistic numerical brain phantoms. They applied deep learning techniques, combining feature selection methods with hybrid neural network architectures to classify simulated scattering data across different AD stages. Table 2.4 summarizes the main contributions of these studies.

2.4.1 Rationale for Microwave Sensing in This Work

Recent biomedical studies have demonstrated that variations in the concentrations of $A\beta_{1-42}$ and $A\beta_{1-40}$ in the CSF induce measurable modifications in its electromagnetic behavior [77, 78]. The experiments described in [77] employ dielectric dispersion analysis between 1 and 6 GHz to monitor $A\beta$ aggregation via dielectric relaxation variations, establishing a physical foundation for microwave sensors to detect protein concentrations at levels relevant for Alzheimer diagnosis in cerebrospinal fluid. The analysis in [78], instead, indicates that adding $A\beta_{1-42}$ and $A\beta_{1-40}$ proteins to canine CSF results in a 5% permittivity reduction at 1 GHz. Canine CSF is utilized because its dielectric properties correlate strongly with human CSF. These findings motivated the idea that MWS could serve as a non invasive tool for detecting such dielectric changes, especially when combined with advanced data driven analysis. Previous numerical investigations have also explored the electromagnetic interaction with amyloid aggregates from a chiral materials perspective, suggesting additional mechanisms through which EM waves may be perturbed by AD related biomarkers [79]. Furthermore, MWS benefits from being a portable, low cost, and non ionizing modality, capable of probing dielectric contrasts through the interaction of microwave fields with biological tissues [2]. However, raw MWS measurements are often high dimensional and difficult to interpret directly; machine learning in an important component for enabling feature extraction and informed decision making [80].

The present work advances the state of the art by providing, to the best of our knowledge, the first experimental demonstration of microwave sensing combined with machine learning for detecting CSF permittivity changes associated with early AD biomarkers. Building upon earlier feasibility analyses [32, 33, 34], we construct an

First Author	Year	Brain parameters and contributions
Saied [71]	2020	Permittivity and conductivity of grey/white matter; modelling of microwave signatures of amyloid plaques/tau tangles.
Ullah [72]	2022	Wearable antenna S-parameter analysis for detecting ventricular enlargement and structural atrophy via microwave sensing.
Ullah [73]	2023	Open dataset of microwave S-parameters from brain phantoms emulating atrophy for algorithm development.
Farhatullah [74]	2024	Microwave radar scattering analysis combined with deep learning classification of AD related patterns.
Liu [75]	2024	Review of microwave sensors and permittivity measurement methods applicable to brain/CSF dielectric monitoring.
Chen [76]	2024	Deep learning applied to numerical brain phantoms for classification of AD different stages, simulating brain atrophy and dielectric changes of grey/white matter.

Table 2.4: Summary of journal articles on microwave sensing/imaging for Alzheimer's related detection.

anatomically inspired, multilayer head phantom whose CSF compartment can be adjusted to mimic different AD-related dielectric conditions. This allows controlled, repeatable reproduction of biomarker driven permittivity variations that were previously examined only in simulations.

By delivering an experimentally validated, data driven microwave sensing approach for AD related CSF alterations, this work fills a critical gap between numerical studies and practical implementation. Beyond its technical contributions, the method aligns well with emerging views that early stage AD is optimally identified through multi modal strategies. A low cost, portable, and non ionizing screening tool such as MWS could substantially enhance accessibility and complement established biomarkers, thereby increasing the likelihood of early detection at the population level.

Moreover, microwave imaging technology offers a potential solution for the high frequency monitoring of patients undergoing clinical trials for novel AD. This modality enables the longitudinal assessment of CSF dynamics and brain physiological states

while providing a mechanism for the early detection of localized brain damage or vascular leakage. Such high temporal resolution monitoring is currently unfeasible with MRI due to significant operational costs, long acquisition cycles, and the lack of portability required for bedside or outpatient applications.

Chapter 3

A proof-of-concept Study of Microwave Sensing for Early Alzheimer's Disease Detection

This chapter details the preliminary experimental framework developed to assess the viability of microwave sensing as a non-invasive diagnostic tool for Alzheimer's Disease. This initial investigation focuses on a binary classification approach to distinguish between healthy and pathological states of a phantom based on the dielectric variations of CSF. The methodologies and results presented here serve as the foundational proof-of-concept for the advanced system proposed later in chapter 4.

3.1 Setup

The microwave sensing system operates in the frequency band of 0.5 GHz to 6.5 GHz. The lower frequency limit is determined by the physical depth of the CSF layer. This thickness is approximately equal to $\lambda_{CSF}/10$, where λ_{CSF} represents the wavelength within the cerebrospinal fluid. Frequencies above 6.5 GHz, instead, suffer from insufficient penetration depth into the cranial volume.

The system configuration is shown in Figure 3.1 and consists of:

- a 4-port VNA obtained through cascaded Keysight P9371A and P9375A units [81];
- four circuit-printed flexible monopoles antennas, created for brain diagnostic applications [26]. These sensors are equipped with a custom bottom layer made of a urethane-graphite mixture to minimize impedance mismatch with the phantom skin, and a top dielectric substrate supporting the ground plane;
- the anthropomorphic head phantom;
- a central processing unit that drives the VNA and saves the measurements.

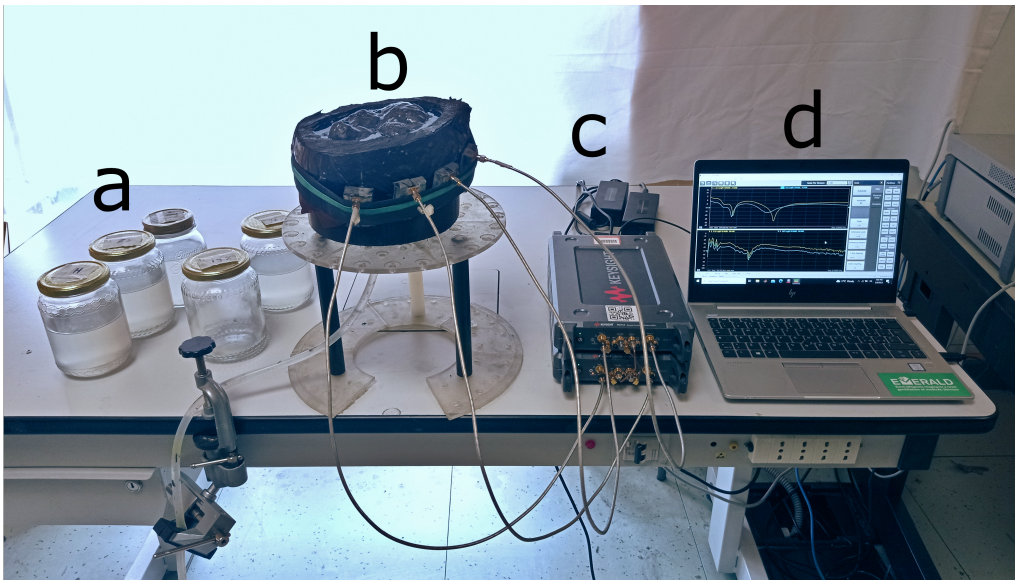

Figure 3.1: proof-of-concept experimental setup; (a): CSF-mimicking liquids; (b) multi-tissue anthropomorphic head phantom, on the side four antennas are placed, the CSF liquid can be poured from the aperture, a clamp closes/opens the tube to flush the fluid; (c) vector network analyzer; (d) central processing unit.

3.2 Phantom

To validate the sensing approach in a controlled environment, a realistic anthropomorphic head phantom created in a previous study of the Wavision research group is utilized [82]. The phantom emulates the geometry and the dielectric behavior of the main components of a human head: skin, bone, fat, CSF, grey matter, white matter, cerebellum, and ventricles. All materials except CSF are solid and created using specific mixtures of urethane rubber, graphite powder, and salt. The recipes for each tissue are shown in Table 3.1. The shapes are modeled through 3D-printed molds based on anatomical CAD models from the Visible Human Project repository [83]. This repository provides high-fidelity geometries reconstructed from cryosectional data, including CT and MRI scans.

The only liquid component of the phantom is CSF, replicated using a mixture of Triton X-100, water, and salt. This recipe to create a fluid with custom dielectric properties is a common and effective strategy that involves only three materials that are easy to find, low-cost, and non toxic [84]. To represent the progression of the disease, five distinct liquid compounds were manufactured and characterized using a coaxial probe kit: one mixture matches the dielectric properties of healthy human CSF derived from the IFAC-CNR database [85], and four mixtures representing varying degrees of AD severity. These were formulated to exhibit relative permittivity values lowered respect to the healthy baseline by 7%, 11%, 19%, and 24% at 1 GHz, where a lower permittivity

Tissue	Urethane rubber (%)	Graphite powder (%)	Salt (%)
Skin	55	45	0
Fat	68	8	24
Skull	80	20	0
Gray	57	43	0
White	62	38	0
Ventricle	50	50	0
Cerebellum	53	47	0

Table 3.1: Recipes of solid materials used in the anthropomorphic phantom employed in the proof-of-concept study.

corresponds to a higher illness severity. The measured permittivity of these liquids, obtained using the dielectric probe method, is shown in Figure 3.2, compared to the literature reference value.

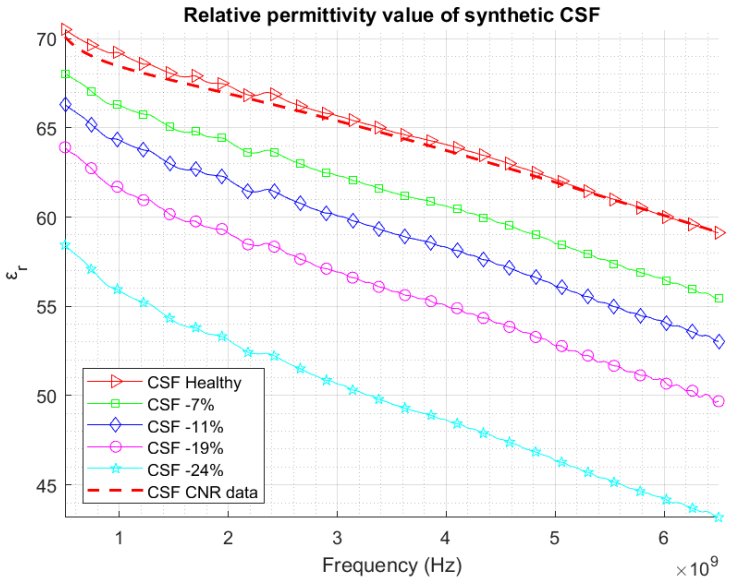

Figure 3.2: Relative permittivity of the synthetic CSF formulations. The graphs illustrate the properties of the five manufactured mixtures, distinguishing between the healthy mimic and the four pathological variants. The dashed red line indicates the literature reference value for healthy human CSF.

The probe used is the Keysight N1501A probe, with the high temperature probe, and the Keysight measurement suite [86]. Figure 3.3 illustrates the equivalent conductivity

of the five liquids. Each sample exhibits marginally lower conductivity than the reference across the entire frequency band. This reduction decreases power transmission between antennas, establishing a more rigorous test condition. However, the variance is negligible, confirming that the liquids provide an accurate approximation of the permittivity found in authentic CSF.

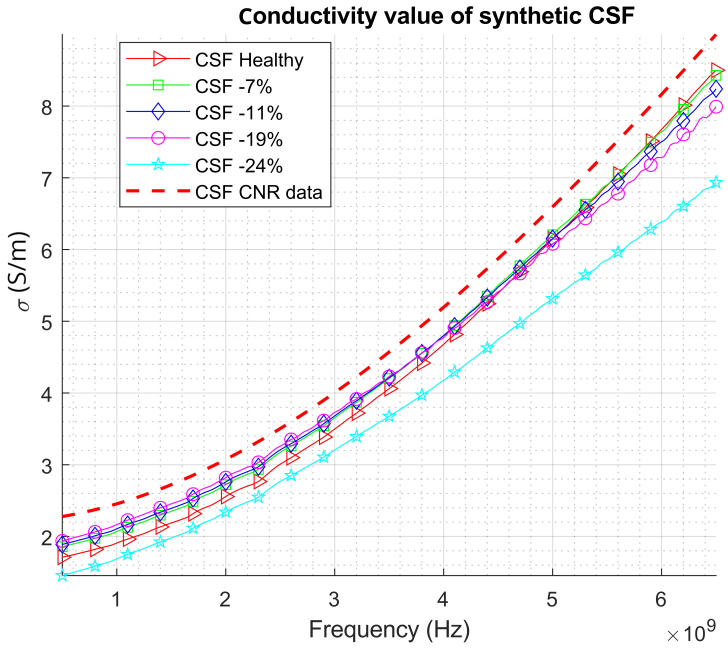

Figure 3.3: Conductivity of the synthetic CSF formulations. The graphs illustrate the properties of the five manufactured mixtures, distinguishing between the healthy mimic and the four pathological variants. The dashed red line indicates the literature reference value for healthy human CSF.

Following the literature [77, 78], a decrease in permittivity between the healthy and AD conditions on the order of 5% would be expected. The larger differences observed between disease severities in this proof-of-concept study are instead related to the objectives and constraints of this initial phase. Specifically, the aim is to assess whether a machine learning algorithm can, in general, discriminate data corresponding to the highest-permittivity liquid (healthy) from the others using a binary classifier. Moreover, the experimental conditions are non-optimal: the phantom was not designed for the specific use case under investigation, and the antennas are optimized for a different application, namely stroke detection [26]. To simplify the classification task at this stage, liquids with pronounced dielectric contrasts are therefore employed, with the intention of adopting more realistic dielectric values in the more in-depth analysis presented in chapter 4.

The phantom has two separated solid parts: an external one corresponding to skin,

fat, and skull, and an internal one corresponding to all brain-related materials. The liquid CSF is poured directly in the space between the external and the internal parts. The phantom design includes a mechanism to empty the intracranial space via a tube and clamp system, allowing for the exchange of these liquids without invasive modifications between measurements. The antennas were arranged on the phantom's surface, all o the same side, acting as both transmitters and receivers to capture the scattering matrix.

3.3 Antennas

Each radiating element has overall dimensions of 48 mm × 30 mm, with a thickness of around 10 mm, and is back-fed via a coaxial connector. A schematic representation of the antenna, together with a picture, is shown in Figure 3.4. From a manufacturing perspective, the antenna consists of a ground plane, a triangular radiator, and a feeding line, all printed on a commercial flexible polyimide film with a thickness of 50 μm. The structure integrates a 5 mm flexible dielectric substrate placed between the radiator and the ground plane, and an additional matching layer intended for contact with the skin. Both layers are realized using custom mixtures of urethane rubber and graphite powder, named G35 (35% graphite by volume for the substrate) and G25 (25% graphite for the matching layer), formulated to achieve the desired dielectric properties while minimizing losses. Specifically, at 1 GHz, the G35 material is characterized by a relative permittivity $\varepsilon_r = 18$ and a conductivity $\sigma = 0.3$ S/m, whereas the G25 material presents $\varepsilon_r = 13$ and $\sigma = 0.2$ S/m. In terms of operating conditions, when used for the brain stroke application these antennas are used in the frequency band between 0.8 GHz and 1 GHz. In this band, the reflection parameter S_{ii} of each antenna is optimally below −10 dB when put on the surface of the phantom mimicking the stroke condition, showing good impedance matching. If we consider the 0.5 to 6.5 GHz band used in this work,

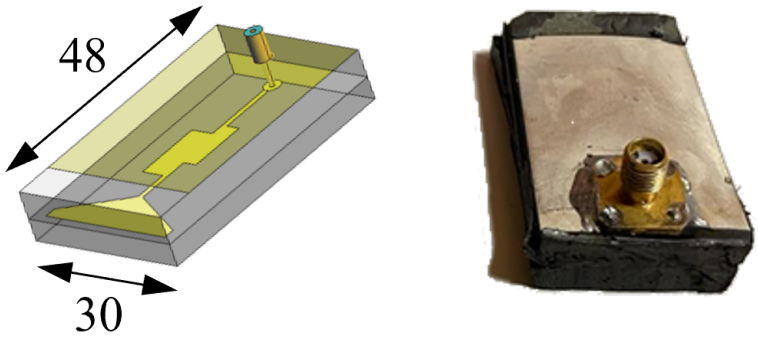

Figure 3.4: Sensors used in the proof-of-concept MWS system: left: schematic with the main dimensions in mm; right: antenna picture.

when put on the surface of the AD mimicking phantom, the S_{ii} of each antenna shows a slightly worse matching is the 0.5 to 0.8 GHz band, the same happens in the band from 1.2 to 2.5 GHz and over 4.5 GHz. The reflection parameters, however, remain under −5 dB, as shown in Figure 3.5. This remains an acceptable value because in the context of a machine learning-based proof-of-concept, the priority in not maximizing power transfer efficiency, but maximizing the spectral information available to the classifier.

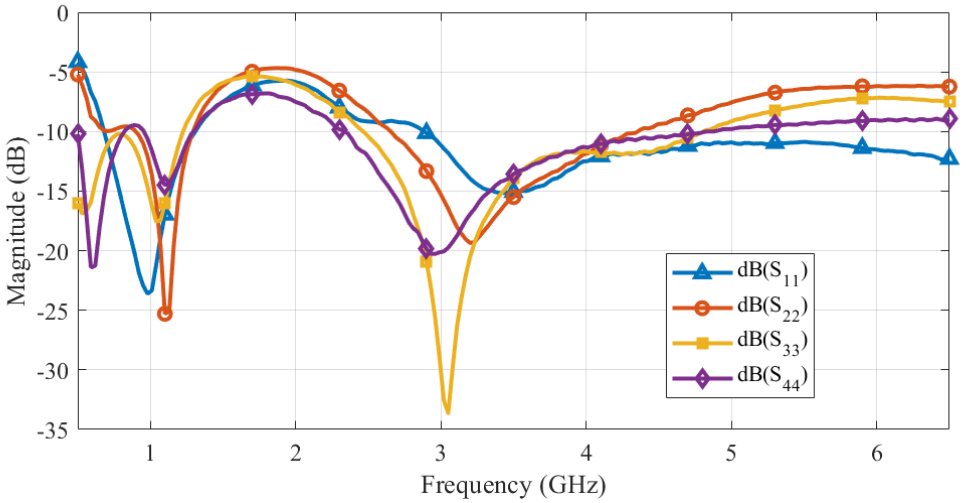

Figure 3.5: Reflection parameters of the four antennas when put on the surface of the phantom filled with the healthy CSF-mimicking liquid

3.4 Data Acquisition Protocol and Dataset Construction

To build a dataset capable of training robust machine learning (ML) models, measurements were conducted over four separate days. The protocol for each session involved filling the phantom with a specific CSF mimic, recording 10 consecutive snapshots of the scattering parameters, emptying the phantom, and repeating the process for the next liquid.

A significant challenge was the inherent class imbalance: there was only one healthy liquid mixture versus four pathological mixtures. To rectify this, 29 additional measurement subsets were performed exclusively for the healthy case. The final aggregated database contained:

- 570 samples representing the Healthy condition;
- 1120 samples representing the AD condition (280 per severity level).

To evaluate the generalization capability of the classifiers, four distinct training sets were constructed based on the temporal distribution of the data (see Table 3.2). This segmentation allows for the assessment of the system's robustness against day-to-day variations and experimental drift.

Dataset	Training data	Healthy/AD Samples	Total
Set 1	Meas. spread widely across all 4 days	370 / 480	850
Set 2	Meas. from the start and end of each day	290 / 600	890
Set 3	All meas. from Days 1, 2, and 4	430 / 800	1230
Set 4	All meas. from Days 1 and 3	600 / 260	860

Table 3.2: Definition of Training Sets for Robustness Analysis

3.5 Machine Learning Implementation Strategies

The classification problem was modeled using Multilayer Perceptron (MLP) due to its non-linear mapping capabilities. Three distinct optimization methodologies were applied to identify the ideal hyperparameters:

Method 1: Basic Architecture Search

This baseline approach utilized a two-layer feed-forward network with sigmoid output neurons. The dataset was split randomly using the following proportions: 70% training, 15% validation, 15% testing. These are standard values in data division for MLP. The variable was the number of neurons in the hidden layer, which was swept from 1 to 100. Training employed the scaled conjugate gradient function with cross-entropy error as the performance metric. The optimized parameters are shown in Table 3.3.

Parameter	Set 1	Set 2	Set 3	Set 4
Number of neurons	20	20	14	17

Table 3.3: Optimized parameters for Method 1

Method 2: Matlab Design Space Exploration

Using the Deep Learning Toolbox, a more extensive search was conducted. The hyperparameters exploration is performed by using all possible combinations of parameters in a given range to establish the best one, using predicted accuracy as the reference metric. The explored parameters are:

- Network structure: Hidden layers (from 1 to 20) and neurons per layer (from 1 to 40).
- Maximum number of iterations (or epochs): set to 150, 500 or 1000.
- Learning rate value: from 1×10^{-4} to 1×10^{-1}.
- Training Function: Resilient backpropagation, scaled conjugate gradient, Powell/Beale restarts, one-step secant, and gradient descent.
- Loss Function: Mean Absolute Error (MAE), Mean Squared Error (MSE), and Cross-Entropy.

The optimized parameters are shown in Table 3.4.

Parameter	Set 1	Set 2	Set 3	Set 4
Number of hidden layers	2	3	3	1
Neurons per hidden layer	30	19	17	19
Maximum iterations	1000	1000	1000	1000
Learning rate value	3×10^{-4}	4.2×10^{-2}	4×10^{-2}	1×10^{-3}
Training function	One step secant	Scaled conjugate gradient	Scaled conjugate gradient	Scaled conjugate gradient
Perform function	Cross-entropy	Mean squared error	Mean squared error	Cross-entropy

Table 3.4: Optimized Parameters for Method 2

Method 3: Python Scikit-learn Optimization

This method leveraged the GridSearchCV tool from the Scikit-learn library [87], that similrarly to method 2 explores the combination of a given set of hyperparameters in a given range. This strategy was used to optimize:

- Network structure: Hidden layers (from 1 to 20) and neurons per layer (from 1 to 40).

- Maximum number of iterations (or epochs): set to 150, 500 or 1000.
- Solvers: Limited-memory BFGS (L-BFGS), Stochastic Gradient Descent (SGD), and Adam.
- Activation Functions: Logistic sigmoid, Hyperbolic tangent (Tanh), and Rectified Linear Unit (ReLU).
- Regularization: Tuning of the Alpha parameter (L2 penalty) and learning rate schedules (constant, inverse scaling, adaptive).

The optimized parameters are shown in Table 3.5.

Parameter	Set 1	Set 2	Traing Set 3	Set 4
Number of hidden layers	20	10	1	1
Neurons per hidden layer	40	20	19	19
Maximum iterations	1000	1000	1000	1000
Solver	LBFGS†	LBFGS†	SGD‡	SGD‡
Alpha parameter	7.5×10^{-3}	11×10^{-2}	1.5×10^{-4}	1×10^{-4}
Activation function	Hyperbolic tangent	Hyperbolic tangent	Logistic sigmoid	Logistic sigmoid

† Limited-memory BFGS.

‡ Stochastic gradient descent with adaptive learning rate.

Table 3.5: Optimized Parameters for Method 3

3.6 Experimental Results and Discussion

The analysis of the binary classifiers demonstrated high accuracy across all methods, summarized in Table 3.6. The most significant finding was the performance of Training Set 4. This set, which trained the network on data from Days 1 and 3 and tested it on Days 2 and 4, achieved accuracies exceeding 90% across all three methods. This indicates a strong capability for domain adaptation, as the network successfully classified measurements from days it had never seen during training. Table 3.7 provides a granular breakdown of the classification metrics for the best-performing scenario (Training Set 4).

Dataset	Method 1	Method 2	Method 3
Set 1	85.1%	88.0%	90.2%
Set 2	85.1%	86.3%	88.1%
Set 3	85.9%	89.6%	83.9%
Set 4	90.8%	90.6%	90.1%

Table 3.6: Comparative Accuracy of the Three Methods on Test Data

Method	Target Class	Precision	Recall	f1-score	Overall Accuracy
Method 1	Healthy	88.5%	89.2%	88.8%	90.8%
	AD	91.9%	91.5%	91.7%	
Method 2	Healthy	88.2%	86.5%	87.3%	90.6%
	AD	92.0%	93.1%	92.5%	
Method 3	Healthy	89.6%	83.2%	86.3%	90.1%
	AD	90.4%	94.2%	92.3%	

Table 3.7: Detailed classification metrics for Set 4 (Test Data)

Regarding network topology, the optimization processes revealed that the decision boundaries of the problem are relatively smooth. In most high-performing configurations, a single hidden layer was sufficient. For instance, Method 3 on Training Set 1 achieved optimal results with a single hidden layer using the hyperbolic tangent activation function.

This initial work confirms that microwave sensing, when coupled with MLP classifiers, can detect AD-related permittivity changes with good accuracy in a realistic phantom. The results validate the feasibility of the non-invasive approach. However, to improve diagnostic granularity, to enhance robustness, and to allow the distinction of different severity levels, a more sophisticated system is required. The following chapter will describe an upgraded hardware configuration with a better-suited new phantom, designed for MWS applications to AD, an increased number of antennas and the implementation of more robust algorithm optimization strategy to address these challenges.

Chapter 4

Design and Validation of a Microwave Sensing System for Early Alzheimer's Disease Detection

This chapter investigates the application of Machine Learning-enhanced Microwave Sensing for the early detection of Alzheimer's Disease. Here is described the development of an advanced experimental framework, built upon the findings of the initial study. This refined system features a custom optimized phantom and an expanded array of six antennas, specifically designed and manufactured for this diagnostic application.

4.1 Microwave Sensing System

The proposed diagnostic tool is built upon a radar-based architecture designed to operate non invasively. The system comprises a computing unit for data processing and a hardware sensing interface. The experimental arrangement for the microwave sensing system is illustrated in Figure 4.1. While it retains the fundamental architecture of the proof-of-concept, consisting of a central processing unit, a VNA, and the antenna array connected to the dielectric head phantom, the following key enhancements have been introduced:

- the VNA configuration has been expanded from four to six ports;
- the radiating elements are custom-designed for broadband operation, ensuring optimal impedance matching across the entire 0.5 to 6.5 GHz frequency spectrum;
- the phantom is specifically engineered for AD investigation, aiming to assess the feasibility of non-invasively classifying CSF based on permittivity variations.

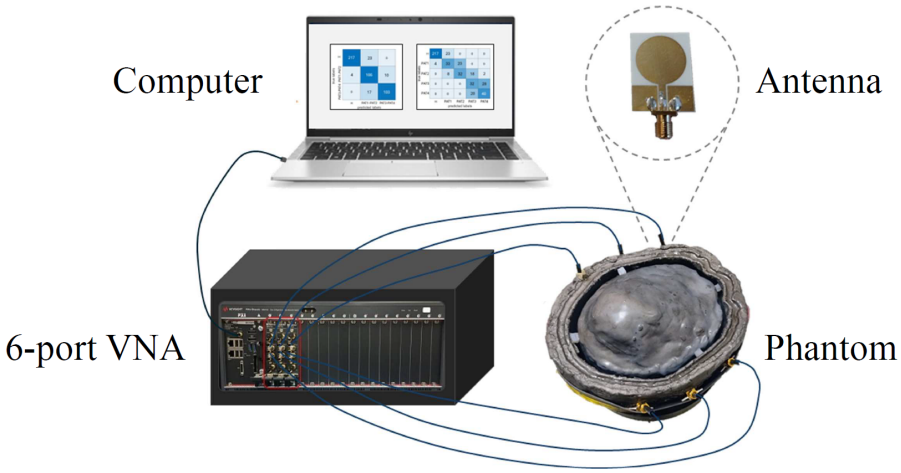

Figure 4.1: Schematic of the microwave sensing system including the VNA, the custom antenna array, and the head phantom.

4.1.1 Antenna Selection and Configuration

The sensing array consists of six custom-designed wideband antennas connected to an M9804A PXIe six-port Vector Network Analyzer [88] via low-loss coaxial cables. The radiating elements are circular monopole antennas printed on a Rogers RO4003C substrate (thickness 1.52 mm), chosen for its ease of manufacturing and compact profile. As in the proof-of-concept case, the operational bandwidth spans from 0.5 to 6.5 GHz.

The antenna geometry was optimized numerically using a simplified multilayer block ($100 \times 100 \times 63$ mm^3) mimicking the dielectric sequence of the human head (skin, fat, skull, CSF, and gray matter) to minimize reflection coefficients in the whole band. The final design is shown in Figure 4.2 and the geometrical parameters are detailed in Table 4.1. Figure 4.3 illustrates the simulated power density profiles within the

Label	W	L	R	W_{Feed}	W_{Gap}	L_{Gap}	L_{GND}
Value	24	32	10	2.9	0.5	0.6	10

Table 4.1: Optimized geometrical parameters of the circular monopole antenna (dimensions in mm).

multi-tissue phantom at the lower, middle, and upper frequency limits. In the center of the frequency band, at 3.5 GHz, the CSF layer is illuminated by a power density distribution that reaches ~25 dBW/m^2 at its maximum inside the layer, while at the minimum frequency of 500 MHz the power density is reduced, primarily due to sub-optimal impedance matching with a maximum of ~2 dBW/m^2. Conversely, at the maximum frequency of 6.5 GHz, the reduction is caused by increased signal attenuation within the tissues, and the maximum value of the power density is ~20 dBW/m^2. This value

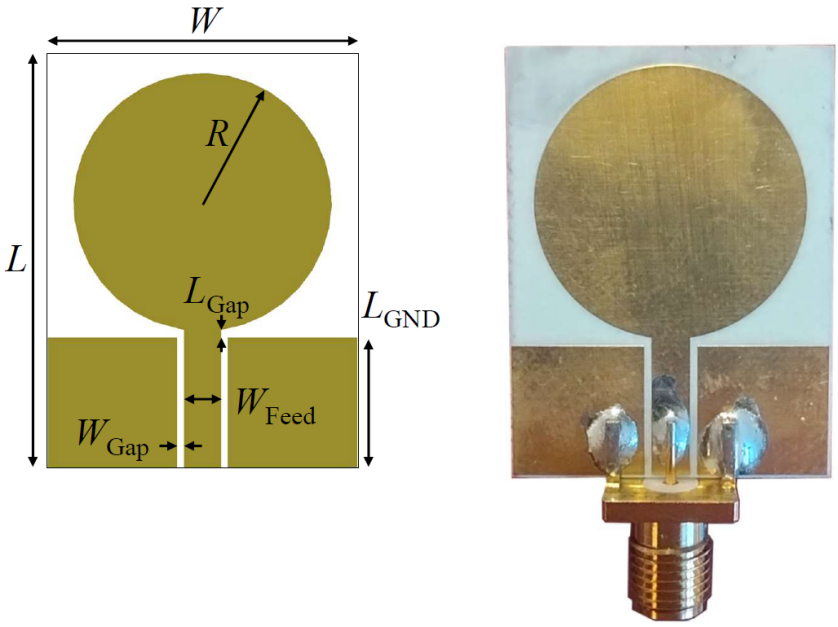

Figure 4.2: Circular monopole antenna design: (a) geometrical layout and (b) the realized prototype used in the array.

exceeds the lower frequency limit because the improved antenna matching compensates for the higher dielectric losses characteristic of the upper spectral range. Despite these limitations at the spectral extremes, the field intensity penetrating the CSF layer remains sufficient in all scenarios to ensure effective sensing performance.

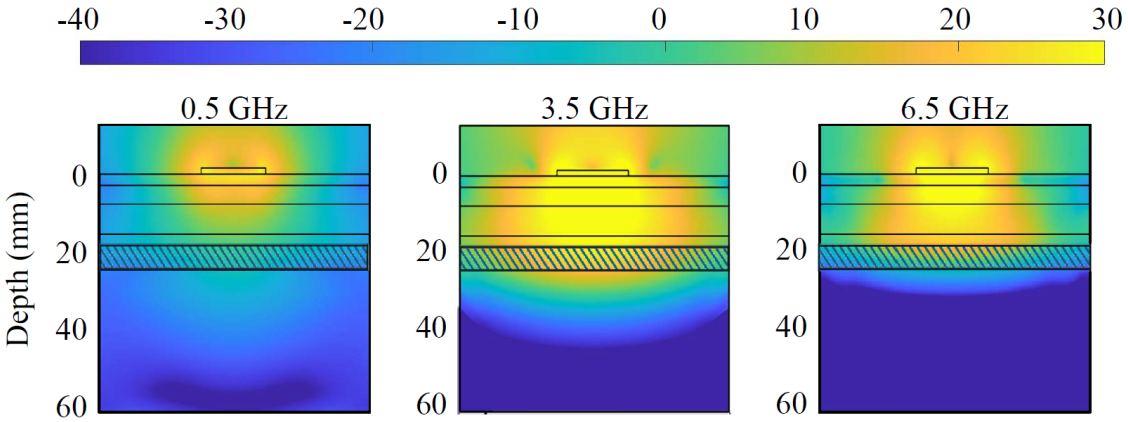

Figure 4.3: Modeled power density distribution (dBW/m^2) inside a block of layered tissues at 0.5, 3.5, and 6.5 GHz. The striped layer denotes the location of the CSF.

Regarding the array configuration, the six antennas are positioned conformally to

the upper lateral sections of the head. This placement exploits the thinner skull regions in the temporal and parietal areas to maximize electromagnetic field penetration into the intracranial cavity. Figure 4.4 illustrates the measured S-parameters, demonstrating that reflection coefficients, shown in 4.4a, remain below -10 dB for most of the band (above 1 GHz). In the 500 MHz to 1 GHz region, matching performance is lower but the S_{11} remains under -5 dB. The transmission levels are within the dynamic range of the instrument, since every transmission coefficient stays above -90 dB for the whole frequency range. In Figure 4.4b, port combinations are organized into three sets according to spatial separation. The short distance group consists of S_{32}, S_{21}, S_{65}, and S_{54}. The medium distance group contains S_{31}, S_{36}, S_{64}, and S_{41}. The remaining port pairs constitute the long distance group.

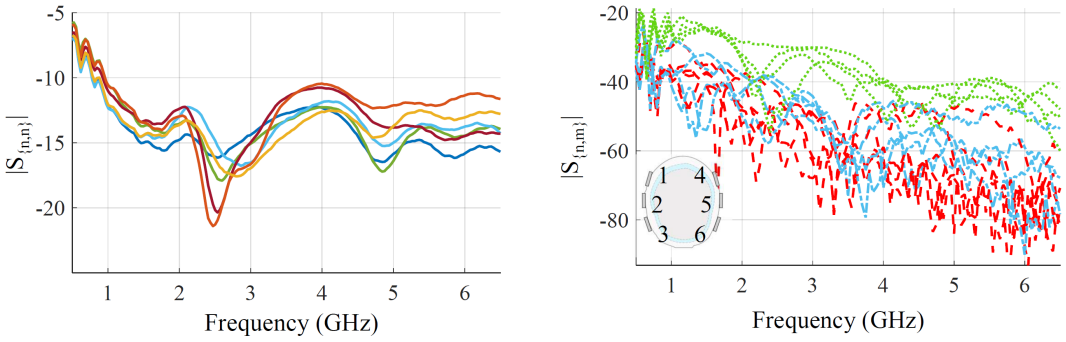

Figure 4.4: Measured scattering parameters on the six antennas on the phantom: (a) Reflection coefficients and (b) Transmission coefficients grouped by antenna distance. Short distances are highlighted using green dotted lines, whereas medium and long distances are marked with blue and red dashed lines. Additionally, a diagram in the corner illustrates the geometric placement of the antennas on the phantom.

4.2 Custom Phantom Development

4.2.1 Material Selection and Characterization

The phantom distinguishes between solid tissues (skin, fat, bone, brain matters) and the liquid CSF. The fat-mimicking tissues were fabricated using 3D-printed carbon-loaded Polylactic Acid (cPLA). Other solid tissues were cast using platinum-catalyzed silicone rubber mixed with graphite powder. This mixture avoids toxic materials like carbon black and allows for dielectric tuning by adjusting the graphite concentration. The specific recipes for the tissue-mimicking materials were selected based on a parametric study of samples containing 1% to 50% graphite mass. By measuring these samples with the coaxial probe method, we matched the graphite content to specific tissue types. The

obtained graphite percentage values are shown in Table 4.2, and Figure 4.5 shows the measured values for the samples compared to the tissue they are representing, together with the dielectric properties of a sample of cPLA compared to human fat.

Tissue	Graphite (%)
Skin	42
Skull	20
Cerebellum	45
Ventricles	50
Gray matter	47
White matter	41

Table 4.2: Graphite powder mass percentage for tissue-mimicking mixtures.

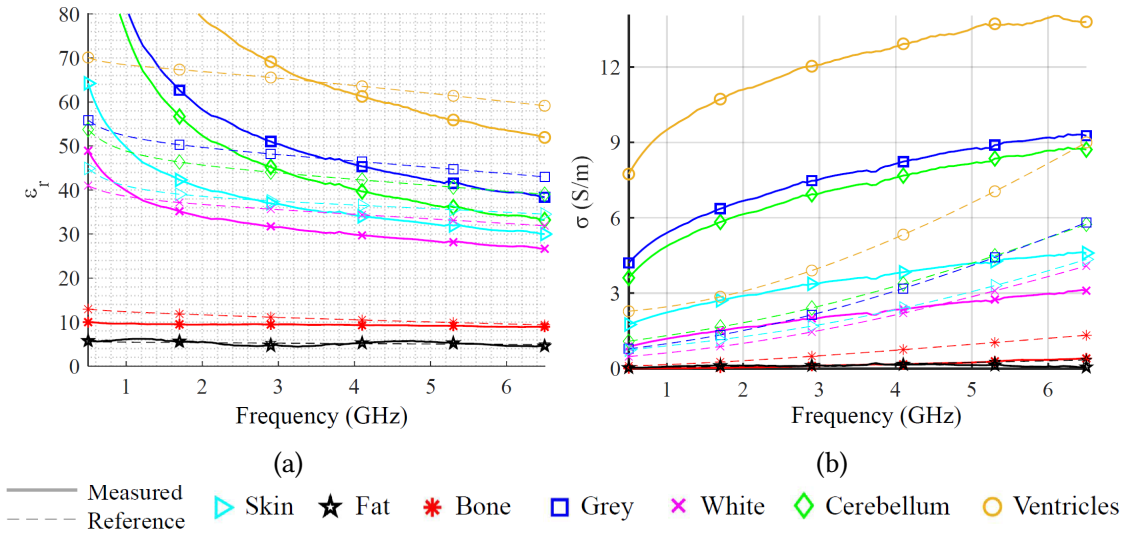

Figure 4.5: Measured dielectric properties of the materials used to create the phantom: (a) permittivity and (b) conductivity.

The optimization process prioritized the relative permittivity at the central frequency (3.5 GHz) to account for the degrees of freedom in the rubber-graphite mixtures and the intrinsic dispersiveness of the tissues. This approach yielded satisfactory agreement with literature data for permittivity, while the conductivity values are higher than the reference targets. This results in increased signal loss, and this condition represent a worsened condition respect to the real case, but still a realistic scenario in terms of signal modulation due to a material changing its properties. Consequently, the phantom

provides a sufficiently challenging and representative environment for the proof-of-concept of the proposed ML-based MWS.

The CSF was simulated using liquid mixtures of water, salt, and Triton X-100. Five distinct fluids were prepared: one representing a healthy condition and four representing pathological stages (PAT1 to PAT4). These pathological fluids mimic the reduced permittivity associated with AD biomarkers, with reductions of 2.5%, 5.0%, 7.5%, and 10.0% relative to the healthy baseline at 1 GHz. The permittivity and conductivity of these liquids, measured using the dielectric probe method with the Keysight N1501A probe, with the high temperature probe, and the Keysight measurement suite [86], is shown in Figure 4.6.

CSF	Water %	Triton X-100 %	Salt %
Healthy	89.43	9.17	1.40
PAT1 (2.5 %)	86.86	11.76	1.38
PAT2 (5.0 %)	84.96	13.66	1.38
PAT3 (7.5 %)	82.99	15.62	1.39
PAT4 (10.0 %)	81.95	16.65	1.40

Table 4.3: Recipes for artificial CSF

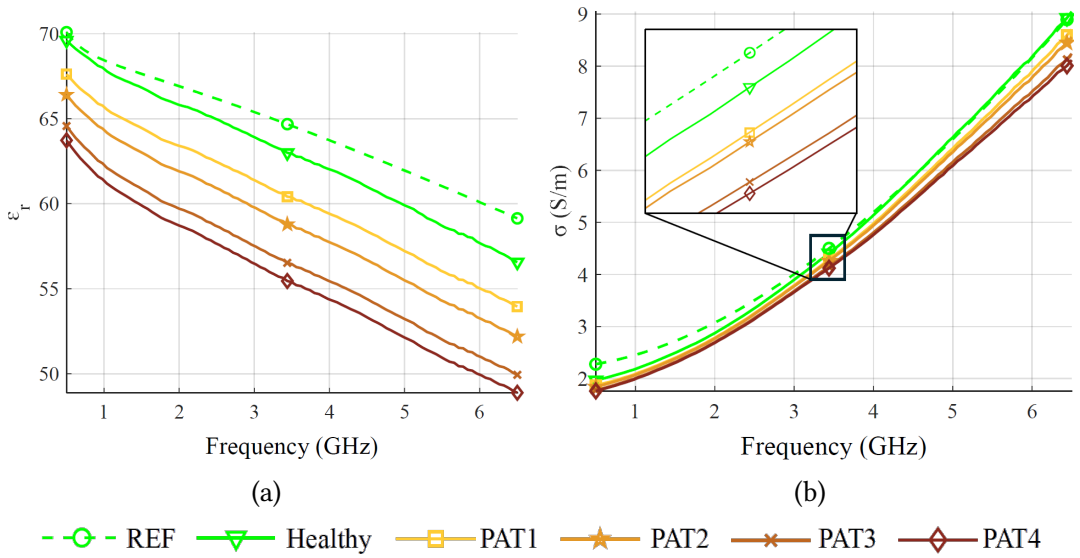

Figure 4.6: Measured dielectric properties of the created liquids that mimic CSF: (a) permittivity and (b) conductivity.

4.2.2 Phantom Fabrication Process

Morphologically, the phantom is derived from the same MRI data as in the proof-of-concept and is divided into two concentric sections separated by a 6 mm gap representing the subarachnoid space filled with CSF. The external shell comprises the skin, skull, and fat layers, while the internal core contains the brain tissues: white matter, gray matter, cerebellum, and ventricles. Rubber spacers maintain the gap width, and a drainage system allows for the exchange of the CSF liquid without disturbing the antenna setup.

The fabrication process begins with the creation of the printed cPLA fat-mimicking tissue, which serves as the structural foundation for the entire external shell (Figure 4.7). This printed substrate is essential for maintaining precise spatial control of the phantom. During assembly, the CSF flushing tube is glued to both the internal and external sections of the printed fat layer. Subsequently, the skull-mimicking material is poured into the space between these sections; due to its lower graphite content, this mixture exhibits a low viscosity that facilitates pouring. Next, the skin-mimicking material is applied to the exterior surface. Its consistency is more viscous and solid-like, allowing for fine regulation of the layer's thickness. Finally, the outer shell is completed by coating the internal surface with a thin layer of rubber to ensure impermeability against the liquid components.

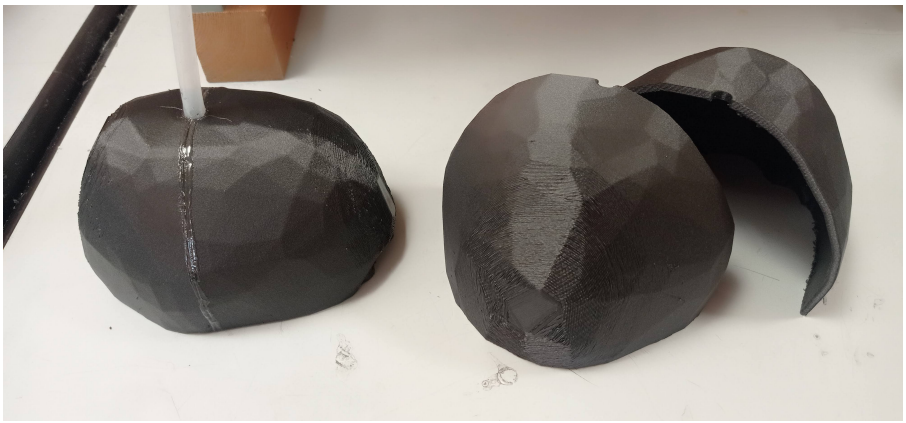

Figure 4.7: The printed fat-mimicking part of the phantom. The tube used to empty the CSF gap is attached to the inner part.

The internal part of the phantom, representing the brain, is shaped using 3D-printed molds, the same of the proof-of-concept case. Figure 4.8 depicts the phantom morphology and highlghts its different parts.

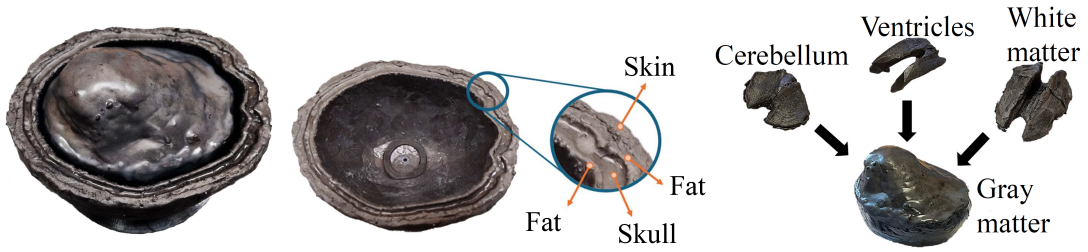

Figure 4.8: The anthropomorphic head phantom: (a) assembled view, (b) external shell, and (c) internal brain core.

4.3 Dataset Construction and Evaluation Protocol

4.3.1 Measurement Setup and Protocols

The system's response is fully characterized using a Multiple Input Multiple Output configuration that captures both transmission and reflection scattering parameters. To ensure data consistency, the experimental procedure for the measurement of a certain scenario adheres to a rigorous iterative workflow consisting of filling the head phantom gap with the appropriate cerebrospinal fluid liquid, acquiring the scattering data 10 consecutive times (these 10 measurements are considered one measurement set), and subsequently draining the phantom. One cycle is made of eight different measurements sets for a total of 80 individual measurements. four sets of each cycle are for the healthy case and each pathological fluid variant is measured for one set, introduced in a randomized order to mitigate any potential systematic bias. This measurement procedure for one cycle is represented in Figure 4.9. The complete dataset is constructed over a three-day measurement campaign, comprising six cycles on each of the first two days and three cycles on the final day. The total dataset is made of 1200 acquisitions of the scattering parameters, where the healthy case is represented 600 times and each pathologic case is represented 150 times.

For each individual measurement, the setup records a 6×6 scattering matrix across a frequency range spanning from 0.5 to 6.5 GHz, distributed over 101 frequency points. The Vector Network Analyzer is configured with an input power of 0 dBm and a narrow Intermediate Frequency (IF) filter of 100 Hz. The narrow bandwidth lowers the noise floor while the power level maintains signal strength, collectively yielding an augmented Signal-to-Noise Ratio (SNR) that ensures precise system characterization.

4.3.2 Data Augmentation

Given the constraints of using a single physical phantom, a data augmentation strategy was employed to enhance dataset variability and account for anatomical asymmetry. A

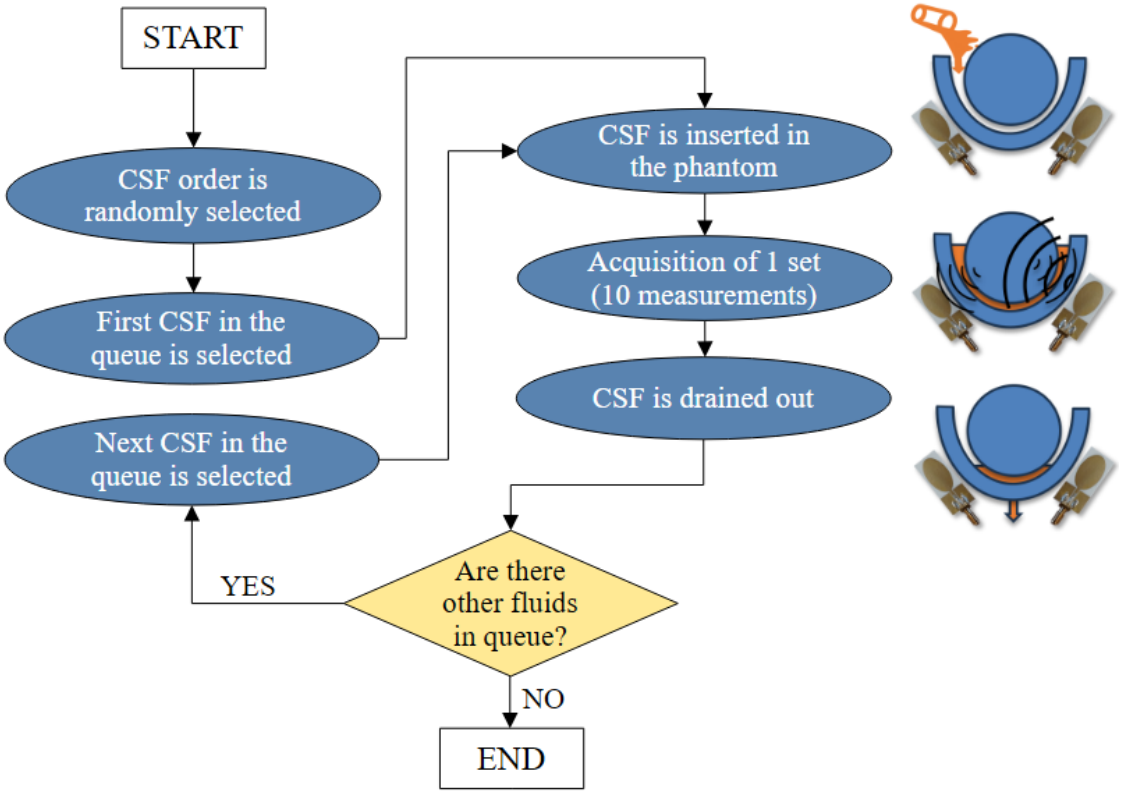

Figure 4.9: Protocol scheme for one measurement cycle.

"flipped" dataset was generated by swapping the data from the left and right antenna elements (as shown in Figure 4.10). This effectively doubled the available samples for training the machine learning models.

4.3.3 Dataset Partitioning

The optimization workflow of the artificial neural network is structured into three sequential stages, namely training, validation, and testing, each serving a distinct and complementary role in the development and assessment of the model. During the training stage, the ANN is exposed to labeled data and iteratively updates its weights and biases through an optimization algorithm with the objective of minimizing a predefined loss function. This process enables the network to capture the underlying patterns and features present in the input data.

The validation stage is introduced to guide model selection and hyperparameter tuning while simultaneously reducing the risk of overfitting. In this phase, the ANN performance is evaluated on a validation set that is not used for weight updates, thereby

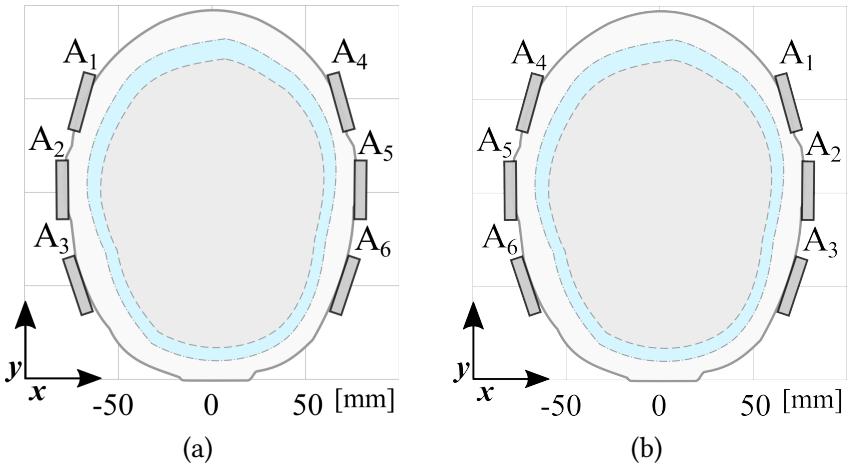

Figure 4.10: Data augmentation. (a) Original array configuration, and (b) flipped configuration.

providing an unbiased estimate of how well the learned representation generalizes beyond the training samples. A critical aspect of this procedure is the division into training and validation subsets according to a predefined ratio, which must balance two competing requirements: ensuring a sufficiently large training set for stable learning and retaining enough validation samples for reliable performance assessment.

To systematically investigate the influence of the training–validation split on classification accuracy and robustness, three commonly adopted split ratios are considered in this study, namely 60:40, 70:30, and 80:20. These configurations allow for a progressive increase in the amount of data available for training, while correspondingly reducing the size of the validation set, enabling a quantitative evaluation of the trade-off between learning capacity and validation reliability. All training and validation experiments are conducted using the data acquired during the first two measurement days.

Two distinct data-partitioning strategies are employed to generate the training and validation sets, with the aim of assessing the sensitivity of the ANN performance to the structure of the data division. In the first strategy, referred to as Data Division 1 (DD1), samples are initially grouped according to their class labels. Subsequently, within each class, samples are randomly assigned to the training and validation sets following the selected split ratio. This approach ensures strict class balance across the subsets and represents a conventional random sampling strategy commonly used in supervised learning tasks.

The second strategy, denoted as Data Division 2 (DD2), adopts a more granular splitting procedure. Specifically, for each of the 192 measurement sets, the 10 individual measurements are randomly partitioned into training and validation subsets using the same percentage ratios. As a result, each measurement set contributes data to both subsets. This design choice is motivated by the need to evaluate whether the ANN performance is influenced by specific measurement conditions or acquisition instances, rather

than solely by class-related features. At the same time, this approach preserves class balance while reducing the likelihood that the model learns measurement-set-specific artifacts. A schematic representation of the DD1 and DD2 procedures is provided in Figure 4.11.

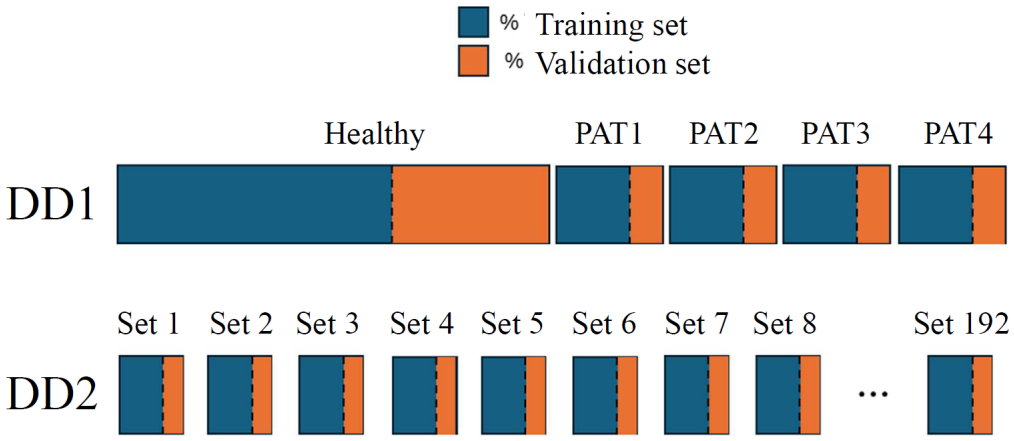

Figure 4.11: Graphical representation of the two data divisions.

Finally, the testing phase is dedicated to evaluating the generalization capability of the trained ANN on completely unseen data. This step provides an unbiased estimate of the model's expected performance in realistic deployment scenarios. To ensure a strict separation between development and evaluation data, the testing set is exclusively composed of measurements collected on the third day, which are not involved in either the training or validation processes.

To summarize, the training and validation data are derived from the first two measurement days and are organized into six distinct partitions. These partitions are generated by applying two data division strategies, DD1 and DD2, across three split ratios: 60:40, 70:30, and 80:20. For each of the six configurations, a single random selection is performed to populate the training and validation subsets. No additional data shuffling or iterative training trials are conducted within a specific configuration. Each resulting classifier is evaluated against a fixed test set consisting of data from the third measurement day, which remains strictly isolated from the training process. The results reported later in this chapter represent the performance of these six individual classifiers, providing a comprehensive view of model behavior across different data selection parameters.

4.4 Machine Learning for Classification

4.4.1 Principal components analysis

To investigate whether the classification task can be effectively addressed using lower-complexity algorithms such as support vector machines (SVMs) or decision trees, a preliminary principal component analysis (PCA) is applied to the original dataset. In this analysis, the augmented samples generated through data flipping are intentionally excluded in order to avoid artificially altering the intrinsic statistical structure of the measurements. PCA is employed as a dimensionality reduction technique that projects the high-dimensional feature space onto a new orthogonal basis composed of uncorrelated principal components, which are ordered according to the amount of variance they explain.

By examining the explained variance ratio associated with each principal component, it is possible to evaluate how the information content of the dataset is distributed across dimensions. In particular, if a large fraction of the total variance is captured by a limited number of components, this would suggest that the underlying structure of the data is relatively low-dimensional, potentially enabling accurate classification using simpler models with reduced representational capacity. Conversely, a slow decay in the explained variance would indicate that the discriminative information is spread across many dimensions, thus motivating the adoption of more expressive classification architectures.

In addition to the quantitative analysis of variance distribution, PCA also enables a qualitative inspection of the data geometry. Visualizing the samples in the space spanned by the first few principal components allows for an assessment of whether distinct clusters or separable regions emerge. The presence of well-defined decision boundaries in this reduced space would support the feasibility of linear or shallow nonlinear classifiers, whereas significant overlap between classes would imply the need for more sophisticated models capable of learning complex, nonlinear decision surfaces.

Figure 4.12 shows a three-dimensional scatter plot of the dataset projected onto the first three principal components (PC1, PC2, and PC3). The visualization highlights the formation of small clusters, each associated with the ten consecutive measurements acquired from a specific measurement set. However, these clusters exhibit noticeable dispersion and partial overlap, which can be attributed to measurement noise, environmental variability, and gradual instrument drift occurring over time. As a consequence, the clusters are not sharply defined or perfectly compact in the reduced-dimensional space. Moreover, the absence of a clear separation that could be achieved through a simple planar decision boundary in the three-dimensional PCA space suggests that the classification problem cannot be adequately solved using linear or low-capacity models alone. This observation provides further justification for adopting a more powerful nonlinear classifier, such as a multilayer perceptron (MLP), which is capable of capturing higher-order feature interactions and complex decision boundaries in the original

feature space.

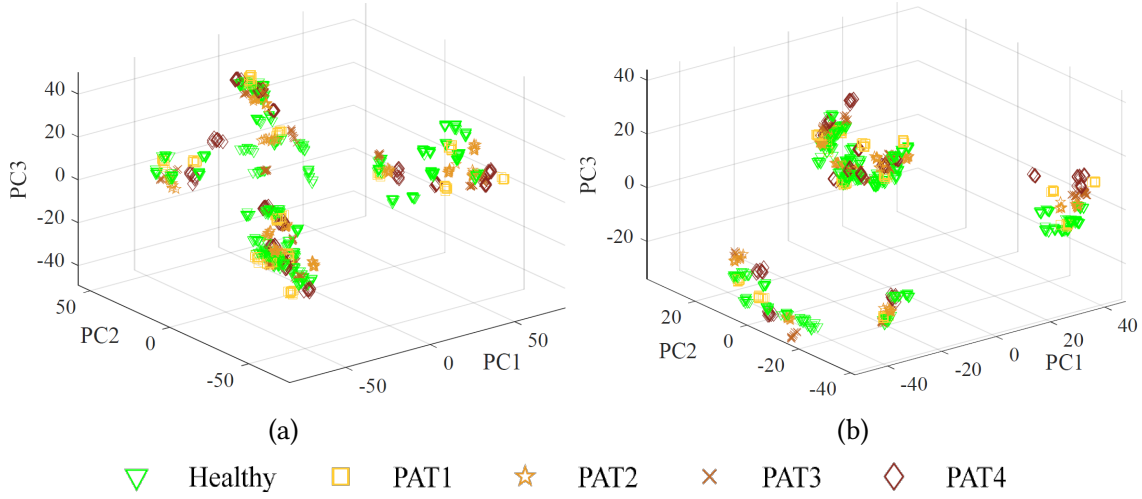

Figure 4.12: PCA analysis. (a) Real and imaginary parts; (b) module only.

4.4.2 Classification Algorithm and Training Strategy

Following the PCA analysis, a MLP neural network is selected for the classification task due to its effectiveness in understanding non-linear differences between classes and because it proved to be a suitable method in the proof-of-concept system. The network architecture includes an input layer, two hidden layers, and an output layer.

During the grid-search optimization procedure, a structured set of hyperparameters defining the architecture and learning behavior of the MLP classifiers is systematically explored. In particular, the optimization includes:

- the number of neurons in each hidden layer, which directly controls the model capacity and its ability to capture non-linear relationships;
- the learning rate, which determines the step size adopted by the optimization algorithm during the iterative minimization of the loss function;
- the training algorithm, responsible for updating the network weights based on the error backpropagation process;
- the loss function, which quantitatively measures the discrepancy between the predicted outputs and the corresponding ground-truth labels.

The resulting optimal hyperparameters configurations for the binary classification task are summarized in Tables 4.4 and 4.5, referring to datasets DD1 and DD2, respectively. For each dataset, results are reported for different training–validation split ratios

(60:40, 70:30, and 80:20) and for the two alternative representations of the input data, namely the full complex-valued scattering parameters (real and imaginary components) and their magnitude (module) only. This comparison enables an assessment of how both data representation and training data availability influence the optimal network configuration.

		60:40 (%)	70:30 (%)	80:20 (%)
Real-Imag	Neurons	6	24	32
	Learning rate	0.03	0.01	0.045
	Training fn.	S-CGB	S-CGB	S-CGB
	Loss fn.	MSE	MSE	SAE
Module	Neurons	32	32	10
	Learning rate	0.035	0.035	0.035
	Training fn.	CGB	CGB	S-CGB
	Loss fn.	MSE	MSE	SAE

Table 4.4: Binary classification, hyperparameters optimization results, DD1.

		60:40 (%)	70:30 (%)	80:20 (%)
Real-Imag	Neurons	10	48	12
	Learning rate	0.02	0.035	0.045
	Training fn.	CGB	CGB	S-CGB
	Loss fn.	MSE	MSE	SAE
Module	Neurons	24	48	24
	Learning rate	0.03	0.025	0.035
	Training fn.	S-CGB	S-CGB	S-CGB
	Loss fn.	MSE	SAE	SAE

Table 4.5: Binary classification, hyperparameters optimization results, DD2.

With respect to the training algorithms, the acronyms CGB and S-CGB denote the conjugate gradient backpropagation method and its scaled variant, respectively. Regarding the loss functions, MSE refers to the mean squared error, which penalizes large deviations more strongly, while SAE indicates the sum of absolute errors, known for its increased robustness to outliers. The selection between these loss functions is determined empirically through the grid-search procedure and reflects the trade-off between sensitivity to large errors and overall stability during training.

All remaining hyperparameters are fixed across the considered configurations in accordance with established best practices for MLP training, as detailed in [89]. Specifically, the minimum gradient threshold of the performance function is set to 10^{-6} as

a stopping criterion, ensuring convergence without unnecessary computational overhead. The validation and test subsets are each assigned a proportion of 15% of the available training data, enabling effective monitoring of generalization performance during learning. A momentum coefficient of 0.9 is employed to accelerate convergence along relevant descent directions while mitigating oscillatory behavior. In addition, the maximum number of allowable validation failures (defined as consecutive epochs during which the validation performance deteriorates) is limited to six, providing an early stopping mechanism to prevent overfitting.

The network architecture is further constrained by fixing the number of hidden layers to two, following the design rationale proposed in the proof-of-concept, which balances expressive power and training stability for problems of comparable complexity. Finally, the maximum number of training epochs is set to 2000, ensuring sufficient iterations for convergence under all tested configurations.

4.4.3 Performance Metrics and Evaluation Criteria

The system performance was evaluated using standard metrics: Accuracy, Precision, Recall, and f1-score. For binary classification tasks, model performance is assessed through accuracy, which represents the fraction of samples that are correctly classified and is defined as:

$$\text{accuracy} = \frac{\text{TP} + \text{TN}}{\text{TP} + \text{TN} + \text{FP} + \text{FN}} \tag{4.1}$$

In this context, TP and TN denote the true positives and true negatives, corresponding to samples that are correctly identified as belonging to the positive and negative classes, respectively. Conversely, FP (false positives) and FN (false negatives) indicate samples that are incorrectly assigned to the positive and negative classes. In addition to accuracy, performance is often characterized using precision, recall, and the f1-score:

$$\text{precision} = \frac{\text{TP}}{\text{TP} + \text{FP}} \tag{4.2}$$

$$\text{recall} = \frac{\text{TP}}{\text{TP} + \text{FN}} \tag{4.3}$$

$$\text{f1-score} = 2 \times \frac{\text{precision} \times \text{recall}}{\text{precision} + \text{recall}} \tag{4.4}$$

Precision expresses how many of the samples predicted as positive are actually correct, whereas recall indicates the ability of the classifier to identify all true positive instances. The f1-score combines precision and recall through their harmonic mean and is particularly suitable in scenarios involving class imbalance. For this reason, it is adopted as the performance metric for the multi-class classifier.

4.5 Results and Discussion

4.5.1 Binary classification

Before presenting and discussing the detailed results of the testing phase for the binary classification task, the performance achieved during the validation stage is summarized in Table 4.6. Specifically, the table reports the accuracy values corresponding to the optimized hyperparameter configurations identified through the grid search procedure. Across all evaluated scenarios, the validation accuracy consistently attains high values, exceeding 96.7%, thereby confirming the effectiveness and stability of the selected MLP architecture prior to final testing.

	Input	60:40 (%)	70:30 (%)	80:20 (%)
DD1	Real-Imaginary	99.35	99.31	99.74
	Module	96.74	98.44	98.18
DD2	Real-Imaginary	99.74	98.26	98.44
	Module	97.92	99.48	98.18

Table 4.6: Binary classification, validation phase accuracy results in percentages.

The performance obtained by applying the various trained classification models to the testing dataset is summarized in Tables 4.7 and 4.8, which correspond to the DD1 and DD2 data-division strategies, respectively. The testing set exclusively consists of previously unseen samples acquired on a different measurement day, thereby providing a stringent and unbiased evaluation of the generalization capability of the trained models under realistic operating conditions.

Input	Metric	60:40 (%)	70:30 (%)	80:20 (%)
Real–Imag	accuracy	73.54	60.62	61.04
	precision	82.70	77.97	78.10
	recall	73.54	60.63	61.04
	f1-score	71.55	53.40	54.07
Module	accuracy	94.37	73.75	81.25
	precision	94.65	82.79	82.14
	recall	94.37	73.75	81.25
	f1-score	94.36	71.81	81.12

Table 4.7: Binary classification performances on the test set, Data Division 1, results in percentages.

Input	Metric	60:40 (%)	70:30 (%)	80:20 (%)
Real–Imag	accuracy	60.00	73.33	72.08
	precision	77.78	82.16	82.00
	recall	60.00	73.33	72.08
	f1-score	52.38	71.29	69.72
Module	accuracy	83.33	92.71	80.00
	precision	86.84	93.34	85.44
	recall	83.33	92.71	80.00
	f1-score	82.93	92.68	79.20

Table 4.8: Binary classification performances on the test set, Data Division 2, results in percentages.

Each table reports a comprehensive set of performance metrics, including accuracy, precision, recall, and f1-score, computed independently for every experimental configuration. The columns represent the different training–validation split ratios adopted during the model optimization phase, as specified in the first row of each table. Furthermore, the results are organized according to the input feature representation: the upper portion of the tables corresponds to the use of separate real and imaginary components of the scattering parameters, while the lower portion presents the results obtained when only the magnitude (module) of the scattering parameters is employed as input to the classifier.

Across both data-division strategies, the classification algorithm consistently achieves superior performance when the module-based feature representation is used. This behavior can be attributed to potential inaccuracies and instability in the experimental estimation of the phase of the scattering parameters, which directly affect the reliability of the complex-valued representation. Phase measurements are inherently more sensitive to noise, instrumental drift, and calibration imperfections, and such effects can propagate through the learning process, ultimately degrading classification performance. In contrast, the magnitude of the scattering parameters is generally more robust to these sources of uncertainty, resulting in more stable and discriminative input features for the neural network.

With respect to the influence of the training–validation split ratios and the adopted data-division strategies (DD1 versus DD2), no systematic or monotonic trend can be identified. In particular, the highest testing performance for DD1 is achieved using the 60:40 partitioning, whereas for DD2 the optimal results correspond to the 70:30 split. This observation suggests that the classification performance is not solely governed by the proportion of training data but is also influenced by the intrinsic variability introduced by the specific data partitioning strategy and measurement structure. As a result, the reported findings emphasize the importance of evaluating multiple data-splitting configurations rather than relying on a single arbitrary partition.

4.5.2 Multiclass classification

Building upon the binary classification results, a subsequent analysis is performed to investigate the capability of the proposed framework to discriminate between different levels of AD severity. This multi-class analysis is conducted starting from the two best-performing binary classifiers, namely the 60:40 configuration for DD1 and the 70:30 configuration for DD2, both using the module-based feature representation. These configurations are selected as they provide the most reliable trade-off between performance and generalization in the binary classification task.

Two alternative pathological classification schemes are considered. In the first scenario, four distinct classes are defined, corresponding to increasing severity levels denoted as PAT1, PAT2, PAT3, and PAT4. In the second scenario, a simplified classification is adopted by grouping the two lowest severity levels (PAT1 and PAT2) into a single class and the two highest severity levels (PAT3 and PAT4) into another class. This hierarchical approach allows for an assessment of whether reducing the granularity of the classification task improves robustness and interpretability.

The optimization of the multi-class MLP algorithm is carried out in the same way as the binary classification, and the results of the optimization process are shown in Table 4.9.

Hyper-Param.	DD1, 60:40 (%)		DD2, 70:30 (%)	
	4 Classes	2 Classes	4 Classes	2 Classes
Neurons	32	2	24	2
Learning rate	0.045	0.03	0.02	0.045
Training fn.	CGB	S-CGB	S-CGB	S-CGB
Loss fn.	MSE	MSE	MSE	MSE

Table 4.9: Multi-class classification, module configuration, MLP hyper-parameters.

The results of the multi-class testing phase are presented in the form of confusion matrices, accompanied by the corresponding f1-score values, in Figures 4.13 and 4.14. In these figures, darker color intensities indicate values closer to the maximum possible count for each true label. Specifically, the maximum value is 240 for the healthy class (labeled as H), 60 for each pathological class in the four-class configuration (PAT1–PAT4) shown in Figure 4.13, and 120 for each pathological group in the two-class configuration (PAT1–PAT2 and PAT3–PAT4) shown in Figure 4.14.

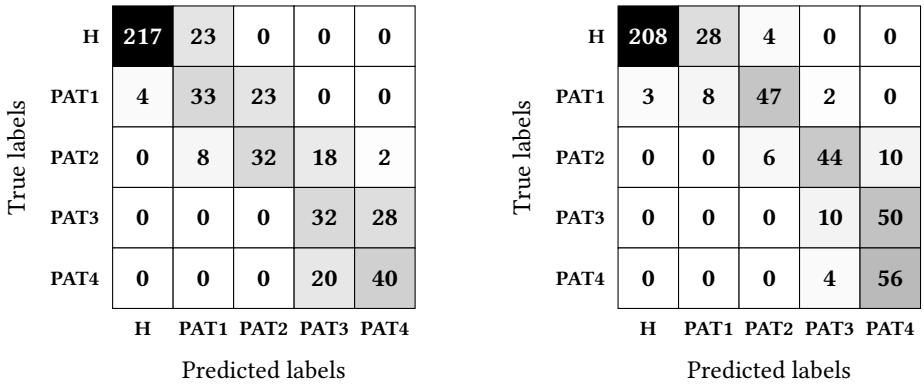

(a) f1-score = 62.76 % (b) f1-score = 39.89 %

Figure 4.13: MLP confusion matrices. for the multi-class classification with four pathological classes, using the module of the scattering parameters as dataset features. A darker color indicates a higher value.(a) DD1, 60:40 (%); (b) DD2, 70:30 (%).

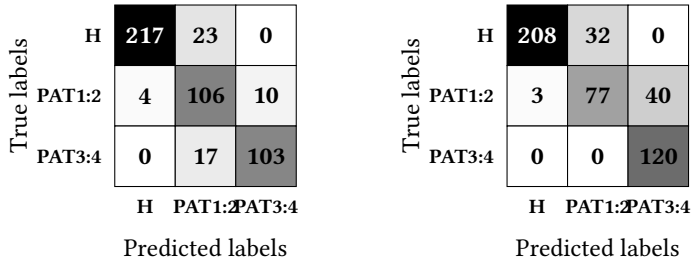

(a) f1-score = 87.42 % (b) f1-score = 81.73 %

Figure 4.14: MLP confusion matrices for the multi-class classification with two pathological classes, using the module of the scattering parameters as dataset features. A darker color indicates a higher value. (a) DD1, 60:40 (%); (b) DD2, 70:30 (%).

It is important to note that these confusion matrices effectively combine the outcomes of the initial binary classification between healthy and pathological cases with the subsequent multi-class classification among pathological categories. This joint representation highlights how errors propagate across the classification hierarchy and provides insight into the specific severity levels that are more prone to misclassification.

The obtained results indicate that the proposed algorithm encounters difficulties when attempting to accurately discriminate among all four pathological severity levels. Nevertheless, when the classification task is simplified to two pathological classes, the model achieves a substantially improved performance, with an f1-score reaching up to 87.42%. This finding suggests that, while fine-grained severity discrimination remains challenging, the framework is effective in distinguishing broader disease stages.

A closer inspection of the confusion matrices in Figure 4.13 reveals that most misclassifications involving pathological cases incorrectly labeled as healthy predominantly occur for PAT1. This behavior is consistent with the fact that PAT1 corresponds to the

mildest pathological condition, which is expected to exhibit dielectric properties more similar to those of healthy cerebrospinal fluid. Conversely, the classifier rarely confuses classes whose permittivity values differ by more than 2.5%, indicating that larger dielectric contrasts translate into more reliable class separability.

4.5.3 Clinical implementation

Several factors must be addressed to transition this technology from a laboratory phantom to a clinical diagnostic setting. For a screening tool to be clinically viable in the context of Alzheimer's Disease, it must achieve performance metrics comparable to existing biomarkers. A common sensitivity and specificity level considered useful for a wide screening is 80%. High sensitivity is especially critical for early stage screening to ensure that potential cases are captured for further diagnostic verification. A high specificity value minimizes false positive results, which lead to unnecessary patient anxiety and healthcare costs. The current system achieves over 94% in all binary classification performance metrics and over 87% in the f1-score for multiclass classification. These results align with the requirements, although these metrics must be validated on a larger and more diverse population.

A significant challenge for clinical translation is the inherent anatomical variability among patients. This study utilizes a single anthropomorphic phantom, even using a data augmentation technique the anatomical variation considered in the experiment is very low. In a real clinical scenario, biological variations and system positioning differences will significantly influence electromagnetic wave propagation. To ensure model generalization, future research must incorporate a library of diverse head geometries and antenna array positions. Training the machine learning models on a broader range of configurations will prevent the algorithm from over fitting to a specific geometry and allow it to learn features that are invariant to individual skull morphology.

Moving toward clinical implementation requires further refinement of the hardware sensing interface. The current use of a benchtop Vector Network Analyzer is suitable for validation but lacks portability. A integrated microwave transceiver system would be necessary for bedside or primary care applications. Furthermore, the machine learning models must be tested against confounding factors such as patient movement or slight variations in antenna placement, which could introduce measurement artifacts not present in a static phantom environment.

Chapter 5

Parkinson's Disease

5.1 Overview on Parkinson's Disease

The history of Parkinson's disease (PD) begins in 1817, when James Parkinson is the first to recognize the today well-known disparate physical changes due to the illness as a single clinical entity. Decades later, Jean-Martin Charcot recognizes the importance of this work and decides to name the condition Parkinson's Disease in honor of his predecessor [90]. Today, what we know about the illness is still being challenged, due to its huge complexity and variety. Recent research from the PD GENEration study [91] has discovered that approximately 13% of people with Parkinson's disease have a genetic link to the condition. This is much higher than previous estimates. While the risk is even higher for certain groups (about 18% for those who started showing symptoms before age 50 or have a family history) nearly 10% of people with no known risk factors also carry these genetic markers. Another finding of the study is that the most common gene involved is GBA1, found in 7.7% of all participants. These findings show that genetics play a bigger role in PD than once thought, and they highlight why genetic testing is becoming an important tool for helping patients find specific clinical trials and more personalized care.

Environmental factors play a critical role in the etiology of Parkinson's disease, often interacting with genetic predispositions to trigger neurodegeneration [92, 93]. Chronic exposure to specific industrial and agricultural chemicals is among the most significant non genetic risks [94, 95, 96, 97]. Pesticides such as paraquat and rotenone are known to inhibit mitochondrial function in dopamine producing neurons [98], while the industrial solvent trichloroethylene (TCE) has recently been linked to a 500% increase in disease risk [99]. Beyond chemical exposure, traumatic brain injury [100] and long term inhalation of fine particulate matter [101] are recognized as major contributors to neuroinflammation and systemic oxidative stress. Conversely, lifestyle choices like regular high intensity aerobic exercise [102] and caffeine consumption [103] have demonstrated neuroprotective effects, likely by enhancing mitochondrial resilience and

modulating dopaminergic signaling. Understanding these modifiable risk factors is essential for developing comprehensive prevention strategies and improving the accuracy of early diagnostic models.

When placed alongside Alzheimer's disease, Parkinson's reflects a similar pattern of progressive system failure. Both conditions share a common biological root: in both diseases, specific proteins in the brain fail to maintain their proper structure and instead begin to clump together, essentially clogging the neural environment and leading to cell death. This process is not immediate; both diseases are characterized by a long period of internal decline that remains hidden until the brain can no longer compensate for the damage. By linking the two, it becomes clear that they are both parts of a broader category of age-related disorders where the brain's internal maintenance systems gradually break down, allowing the accumulation of waste to disrupt the overall neural network.

5.1.1 Clinical Symptoms, Disease Progression and Physiological Changes

Parkinson's disease represents a chronic degradation of neural architecture characterized by the systematic failure of cellular maintenance and the accumulation of misfolded alpha synuclein proteins into insoluble clumps called Lewy bodies [104]. The disease follows a transition from localized clusters to widespread network failure. This process begins decades before clinical diagnosis through two distinct pathways: the body-first and brain-first models [105].

In the body-first model, pathology originates in the peripheral autonomic nervous system, such as the enteric system of the gut. Misfolded proteins ascend through the vagus nerve into the brainstem in a bottom up trajectory. This subtype is associated with early non motor symptoms like sleep disorders and digestive issues [106]. Conversely, the brain-first model follows a top down progression starting in the olfactory bulb or the brain itself. A hallmark of this subtype is marked hemispheric asymmetry during early stages, where neuronal loss and structural changes are significantly more advanced on one side of the brain [107, 108]. Current research indicates that these two subtypes are distributed approximately equally across the patient population, each accounting for roughly 50% of cases [106].

The most critical transition occurs when the pathology reaches the substantia nigra (SN), a component of the basal ganglia, that is a deep brain structure that operates as a control unit for purposeful movement and has a central role in the regulation of reward seeking behavior, motivation, and executive decision making [109]. SN is divided into two distinct functional regions:

- pars compacta (SNpc): This region contains the dense population of neurons responsible for the synthesis and storage of dopamine. It communicates with the striatum, putamen, and caudate nucleus to modulate motor signals;

- pars reticulata (SNpr): This region consists of GABAergic neurons that receive inputs from the putamen and caudate nucleus. Its primary output regulates eye and head movements.

PD affects specifically the SNpc, where between 40% and 60% of dopaminergic neurons are typically lost before motor symptoms emerge [110, 111]. This loss disrupts the production of dopamine, a neurotransmitter that regulates the gain of neural circuits. In the basal ganglia, dopamine acts as a biological switch to balance the direct and indirect pathways. By exciting the direct pathway and inhibiting the indirect pathway, it facilitates fluid movement. It also drives the reward system by signaling prediction errors, functioning as the internal currency for motivation and action [112].

The clinical manifestation of this internal failure begins with non motor prodromal symptoms, such as autonomic dysfunction and mood changes, which indicate early systemic instability [113]. As dopaminergic depletion reaches a critical threshold, motor hallmarks appear. These typically start as asymmetric resting tremors and muscular rigidity [114]. As the degradation of the basal ganglia control loops progresses, patients experience bradykinesia (slowness of movement) and impaired postural stability.

In advanced stages, the neurodegenerative process becomes bilateral and spreads into the cerebral cortex. The brain can no longer compensate for the loss of signal gain. Structural changes such as the accumulation of iron and the loss of neuromelanin in the SNpc alter the local tissue environment and its electromagnetic properties [115]. The final stages involve widespread cortical failure [116], leading to the severe cognitive and systemic decline characteristic of late stage Parkinson's disease.

5.1.2 Epidemiology and Socio-Economic Impact

The global prevalence of Parkinson's disease has more than doubled over the last two decades [117]. It is now categorized as the fastest growing neurological disorder in the world [118, 119]. This surge is primarily attributed to the transition toward an aging global population, though environmental factors and increased industrialization also appear to play a role. Current estimates indicate that over 11.7 million people worldwide live with the condition [120, 121].

The economic burden associated with the disease is substantial and multifaceted. It includes direct medical costs, such as hospitalizations and medications, and indirect costs, such as loss of productivity and premature retirement. The total societal cost of illness for Parkinson's disease on a global scale is estimated to be over $100 billion [122]. This number combines direct medical expenses with indirect and non medical costs. Direct costs include hospitalizations, specialized nursing care, and prescription medications. Indirect costs account for the loss of economic productivity when patients must retire early or when family members reduce their working hours to provide unpaid assistance. These costs scale exponentially as the disease progresses from early to advanced stages.

A critical and often under-reported component of this impact is the cost of informal care. Many patients rely on family members who must reduce their working hours or exit the workforce entirely to provide daily assistance. This unpaid labor represents a significant portion of the total economic strain, often accounting for nearly 40% of the overall cost per patient [123].

Table 5.1 summarizes the main numbers about the impact of PD on a socio-economic level.

Metric	**Estimated Value**
Global Population Impact	> 11.7 million cases [120]
Global Economic Burden	> $100 billion USD [122]
Country Level Burden (USA)	$61.5 billion annually [124]
Informal Care Burden	$25 billion annually [124]
Individual Patient Cost	$22,800 to $50,000 [122]

Table 5.1: Economic and social impact of Parkinson's disease.

5.2 Diagnosis

5.2.1 Clinical Examination and Sypmtom-Based Diagnosis

The current diagnostic framework for Parkinson's disease is fundamentally based on clinical observation rather than a single definitive laboratory test. Because no biological marker is yet universally accepted as a standalone diagnostic tool, neurologists must rely on the identification of specific motor and non motor patterns. The foundational requirement for a diagnosis is the presence of parkinsonism, which is defined as the coexistence of slowness of movement (i.e., bradykinesia) and at least one other cardinal symptom, such as a resting tremor or muscular stiffness [125].

To standardize this observational process, the Movement Disorder Society (MDS) developed the Unified Parkinson's Disease Rating Scale (MDS-UPDRS) [126]. This scale functions as a rigorous scoring system that evaluates the patient across four distinct categories: non motor experiences of daily living, motor experiences of daily living, motor examination, and motor complications. By quantifying these observations, clinicians can track the progression of the disease and the efficacy of treatments. Additionally, clinicians often monitor how a patient responds to dopaminergic medication like levodopa; a significant improvement in motor function often serves as a practical confirmation of the diagnosis.

However, the clinical method faces significant limitations during the early stages of the disease. Many symptoms of Parkinson's disease overlap with those of atypical

parkinsonian syndromes, such as Multiple System Atrophy or Progressive Supranuclear Palsy [127]. These similar conditions can lead to misdiagnosis, particularly when the neural damage is not yet widespread. The subjective nature of the rating scales highlights the need for objective and quantitative diagnostic tools that can detect structural shifts before the physical symptoms become visible to a clinician.

5.2.2 Imaging and Laboratory Tests Used in PD

Beyond clinical observation, the diagnostic landscape for Parkinson's disease has expanded to include advanced neuroimaging and laboratory biomarkers. These technologies transition the diagnosis from a subjective evaluation of motor signals to an objective measurement of the underlying pathology. Neuroimaging primarily focuses on the integrity of the dopaminergic system in the midbrain. Techniques such as DaT-SPECT [128] and 18F-DOPA PET [129] allow clinicians to visualize the depletion of dopamine transporters and the loss of presynaptic function. Additionally, advanced MRI modalities like neuromelanin sensitive imaging (NM-MRI) [130] are increasingly used to detect microstructural changes in the substantia nigra.

In the laboratory, the emergence of the alpha synuclein seed amplification assay (αSyn-SAA) represents a major shift [131, 132]. This biochemical test detects the presence of misfolded protein aggregates in the cerebrospinal fluid or skin with high sensitivity, often before the onset of motor symptoms. Research in now also focused on less invasive blood based biomarkers, including tRNA fragments and mitochondrial DNA, which offer a potential for large scale screening [133]. These quantitative methods provide a necessary technical baseline for the development of microwave imaging, which aims to offer a similarly objective diagnosis at a lower cost.

Table 5.2 summarizes the current used techniques to diagnose PD.

5.3 Current Early Diagnostic Strategies

An earlier PD detection significantly improves the wellness of patients and caregivers by enabling the implementation of proactive management strategies before the neural network reaches a state of critical failure. For the patient, identifying the pathology in its prodromal phase allows for the initiation of neuroprotective therapies and lifestyle interventions that preserve the functional integrity of the dopaminergic system for a longer duration [134]. This early intervention effectively delays the onset of severe motor deficits and cognitive decline, extending the period of physical independence and reducing the psychological distress associated with undiagnosed symptoms. For the caregiver, a timely diagnosis provides a useful window for education and technical training, allowing for the gradual adaptation of the home environment and the establishment of long term financial and legal plans.

Technique	Mechanism	Target
DaT-SPECT [128]	Radioactive tracer binding to dopamine transporters.	Presynaptic integrity
18F-DOPA PET[129]	Positron emission tracking of dopamine synthesis	Metabolic activity
NM-MRI [130]	Sensitivity to the paramagnetic properties of neuromelanin	SN structure
αSyn-SAA [131]	Amplification of misfolded protein seeds in CSF	Protein aggregation
Syn-One Test [132]	Detection of phosphorylated α-synuclein in skin	Peripheral pathology
tRNA Blood Test [133]	Quantification of specific RNA motifs in plasma	Early systemic signal

Table 5.2: Current imaging and laboratory technologies for PD detection.

5.3.1 Digital and Sensor-Based Monitoring

The integration of digital health technologies and wearable sensors represents a significant shift toward continuous, objective monitoring for early PD detection. Unlike periodic clinical visits, these technologies provide high resolution longitudinal data that can capture subtle fluctuations in motor and non motor behavior. Current research focuses on the use of inertial measurement units (IMUs), such as accelerometers and gyroscopes, embedded in smartphones and smartwatches to quantify gait parameters, postural sway, and tremors with sub millimeter precision [135].

Beyond wearable motion sensors, several specialized digital biomarkers are under investigation. These include:

- Digital Typing and Keystroke Dynamics: Analyzing the timing and pressure of typing on a keyboard to detect fine motor degradation [136].
- Acoustic and Speech Analysis: Using machine learning to identify vocal tremors, reduced volume, or changes in pitch that often precede motor symptoms [137].
- Smart Home Ambient Sensors: Utilizing passive infrared or radio frequency sensors to monitor changes in gait speed or sleep patterns without requiring the patient to wear a device [138].
- Virtual Reality (VR) Assessment: Eye movements analysis while in a virtual reality environment [139].

These digital tools offer a non invasive way to collect real world data, providing a more accurate representation of a patient's functional status than a single snapshot in a clinic.

5.3.2 Biomarkers and Neuroimaging Techniques

The following overview details the pre-symptomatic biomarkers used for early PD detection, excluding movement based sensors. These biomarkers are proteopathic, structural, functional, and biochemical signals that emerge during the prodromal phase.

The identification of pre-symptomatic biomarkers has transitioned the diagnostic focus from observing physical tremors to detecting the earliest molecular and structural shifts in the nervous system. The most significant advancement is the Alpha-Synuclein Seed Amplification Assay (αSyn-SAA) [140], which identifies misfolded protein predecessors in CSF or skin biopsies with near-perfect accuracy up to 15 years before motor symptoms appear.

Parallel to protein detection, structural imaging such as Neuromelanin-Sensitive MRI (NM-MRI) [130] allow for the visualization of neuronal attrition in the substantia nigra. These techniques detect the loss of the dark pigment neuromelanin and the increase of extracellular fluid that occurs as cells die [130]. Functional biomarkers, specifically DaT-SPECT and 18F-DOPA PET [128], remain critical for measuring the declining density of dopamine transporters and metabolic activity. Furthermore, systemic biomarkers like Hyposmia (loss of smell) and Isolated REM Sleep Behavior Disorder (iRBD) serve as powerful clinical indicators of early brain-first and body-first pathology [141]. Finally, emerging blood-based biomarkers, including Neurofilament Light Chain (NfL) and immune cell signatures, offer a potential for minimally invasive large-scale screening [142].

Table 5.3 summarizes the primary biomarkers for early PD diagnosis, focusing on structural, biochemical, and sensory markers.

5.4 Opportunities for Microwave Imaging in PD

Given the profound heterogeneity of Parkinson's disease, expanding the availability of diverse diagnostic modalities is essential for capturing its complex range of clinical presentations. The illness varies significantly between individuals, and a single diagnostic approach is often insufficient for a comprehensive assessment. Integrating multiple sensing technologies allows clinicians to cross reference different physiological signals, reducing the risk of misdiagnosis and ensuring that various disease subtypes are identified early.

In this context, microwave imaging offers a distinct technical advantage as a relatively inexpensive and non invasive method. While such a differential approach may have lower sensitivity for the more symmetrical body-first cases, its utility as a low cost and portable screening tool remains significant. Its portability and low operational

Category	Biomarker	Diagnostic Target
Proteopathic	αSyn-SAA (CSF/Skin)	Misfolded α-synuclein seeds [140]
Structural	Neuromelanin-MRI (NM-MRI)	SNpc pigmentation loss [130]
Functional	DaT-SPECT	Dopamine transporter density [128]
Fluid-Based	Neurofilament Light (NfL)	Axonal neurodegeneration [142]
Molecular	Single-cell RNA sequencing (Blood)	Immune system activation [143]
Sensory	Olfactory Testing (SIT)	Olfactory bulb integrity [141]
Autonomic	MIBG Scintigraphy	Cardiac sympathetic denervation [144]

Table 5.3: Pre-Symptomatic and Early Diagnostic Biomarkers for Parkinson's Disease (Non-Motor).

costs make it an ideal candidate for mass screening programs, potentially reaching populations that lack access to high field MRI or PET infrastructure. By providing a scalable solution for large scale monitoring, microwave imaging could serve as a frontline tool to identify high risk individuals, facilitating timely intervention and significantly improving long term patient outcomes.

Recent proof of concept studies have established the technical groundwork for applying microwave based techniques to PD monitoring. These initial works focus on the transition from purely morphological imaging to the detection of biological activity. By utilizing Ultra Wideband (UWB) antennas, researchers successfully localized signals produced by a microtag mimicking an action potential that is potentially associated with PD [145]. The authors utilized a pair of UWB antennas operating in the 0.5 to 2.5 GHz range to perform measurements on a cylindrical brain phantom containing a microtag. This microtag employed a photodiode to modulate the incident microwave field with a 1 kHz signal which was then re-radiated as backscattered microwave currents. By extracting the 1 kHz modulation from the received signals, the system successfully localized the simulated activity source. This system achieved a good spatial resolution within the brain phantom, demonstrating that microwave fields can be modulated to capture functional signals rather than just anatomical structures.

Further advancements have moved toward disease specific applications by targeting

known biomarkers of PD. One notable methodology employs Pulse Amplitude Modulation (PAM) to monitor the beta frequency band within the basal ganglia thalamocortical (BGTC) circuit, a key indicator of Parkinsonian states [146]. This approach utilizes two orthogonal sets of UWB probes to extract modeled action potentials from a microtag. Experimental results confirmed the ability to differentiate between healthy and pathological signaling characteristics within a head phantom. These works represent the first steps in validating microwaves as a tool capable of monitoring PD.

Chapter 6

Microwave Imaging for Parkinson's Disease Detection

This chapter details the research conducted at Universitat Politècnica de Catalunya (UPC) under the supervision of professor Luis Jofre-Roca. The primary objective was to evaluate the feasibility of detecting and imaging localized dielectric contrasts within a controlled environment as a proxy for the physiological changes associated with Parkinson disease. While the precise magnitude of these dielectric variations in real pathological scenarios is not yet fully quantified by the scientific community, the massive loss of dopaminergic neurons and subsequent astrogliosis alters the local water content and ionic concentrations. These factors are the primary determinants of dielectric behavior at microwave frequencies. Additionally, the accumulation of iron and the depletion of neuromelanin within the SNpc modify the conductive properties of tissues, generating a measurable dielectric contrast relatively to healthy tissue. For the brain-first subtype the resulting hemispheric asymmetry provides a differential signal that microwave algorithms can leverage to isolate pathological changes from common mode noise allowing for detection during early stages.

The experimental configuration consists of four horn antennas positioned around a head model to acquire the 4×4 complex scattering matrices across a frequency range from 0.5 to 2 GHz. The imaging process employs a differential approach by comparing data from a background scenario representing healthy tissue with a target scenario containing a specific dielectric contrast. This methodology allows for the spatial reconstruction of the dielectric anomaly to identify its exact coordinates.

To evaluate system sensitivity and the ability to detect localized contrasts within deep brain structures like the SNpc, a simplified 3D printed phantom of the human head was developed. A novel validation technique was implemented that utilizes the temperature dependent dielectric properties of water to simulate varying contrast levels. This approach provides a reliable and repeatable framework for determining the minimum dielectric contrast threshold required to accurately localize the target within the reconstructed image.

6.1 Dielectric Characterization of Water

6.1.1 Theoretical Model from Literature

Having precise data regarding the dielectric characteristics of materials is fundamental in microwave-based sensing and imaging systems. Because of this, deionized water is a standard selection for anthropomorphic phantoms. This choice is due to its well-known electromagnetic behavior, the abundance of the resource, and its low price. Both relative permittivity ε_r and conductivity σ dependencies on frequency f and temperature T have been deeply studied and documented. The objective of this study is to leverage the thermal dependencies of this material to produce customized contrasts within a static phantom structure without altering its physical configuration. Avoiding any unwanted modifications in the test scenario is crucial to produce reliable information, especially when testing a system sensitivity is being quantified.

The behavior of materials exposed to an oscillating field is generally described through the Debye relaxation model. It provides a mathematical framework for the time dependent polarization of a material and, through the model, it is possible to describe the complex permittivity of water $\varepsilon(f, T)$ as:

$$\varepsilon(f, T) = \varepsilon_\infty(T) + \frac{\varepsilon_s(T) - \varepsilon_\infty(T)}{1 + j2\pi f \tau(T)}, \tag{6.1}$$

where ε_s represents the static permittivity while ε_∞ denotes the permittivity at the high frequency limit and τ is the relaxation time. Since water is a homogeneous simple material, there is no need for the more complex Cole-Cole model described in 1.4. In literature, the dependence of complex permittivity to temperature and frequency is calculated experimentally [147]. From the complex permittivity we get the relative permittivity ε_r and the conductivity σ, and by applying this model the values of ε_r and σ for the thermal range between 25°C and 50°C are calculated. The calculation results are plotted in Figure 6.1 for frequencies from 0.5 to 3 GHz.

The model prediction, by visual inspection, seems to highlight a linear behavior for both dielectric parameters inside this temperature window. This linearity is quantified using the coefficient of determination R^2 [148], that defines the strength of the relationship between the model and the data, comparing the data calculated using the Debye model with their linear regression. The closer the coefficient value is to 1, the closer we are to a linear behavior.

The formula to calculate this coefficient is:

$$R^2 = 1 - \frac{SS_{\text{res}}}{SS_{\text{tot}}}, \tag{6.2}$$

where the residual sum of squares SS_{res} and the total sum of squares SS_{tot} are calculated as:

$$SS_{\text{res}} = \sum_i (y_i - \hat{y}_i)^2, \quad SS_{\text{tot}} = \sum_i (y_i - \bar{y})^2. \tag{6.3}$$

In these expressions, y_i is the calculated data while $\hat{y}_i$ is the linear model estimate and $\bar{y}$ is the arithmetic mean. For all investigated frequencies, the calculated R^2 exceeds 0.985 which confirms a near linear trend.

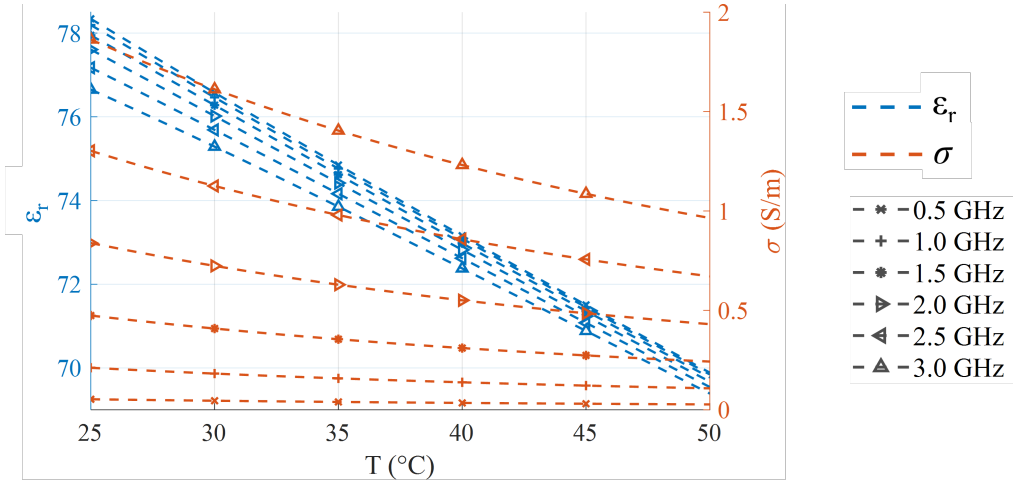

Figure 6.1: Dielectric properties ε_r (blue) and σ (orange) of water across a 25°C to 50°C range. Data points are derived from the Debye model at discrete frequency intervals. All results show a linearity coefficient $R^2 > 0.985$.

6.1.2 Experimental Measurements

Empirical measurements were performed on deionized water to test the linearity of water dielectric properties in temperature in a real setup. The used sample is a 80 mL volume of water that was initially heated to 36.5°C and then monitored during a cooling phase until reaching 26.0°C, very close to room temperature. The speed at which the water temperature cools down decreases when approaching room temperature, from few seconds at the start to several minutes towards the end of the process. A thermal sensor with a resolution of 0.1°C tracked the cooling process. At every 0.1°C temperature decrement, the complex permittivity is captured using a coaxial probe interfaced with a Keysight N9918A vector network analyzer (VNA) [149]. Data extraction and analysis utilized the Keysight Materials Measurement Suite version 20.0.24092501 [150]. To evaluate the precision obtainable in the control of the dielectric properties of deionized water, the relative sensitivity is evaluated and compared with the theorethical sensitivity. The relative sensitivity in the control of relative permittivity η_{ε_r} and the relative sensitivity in the control of conductivity η_σ for a 0.1°C thermal shift are defined as:

$$\eta_\sigma = \frac{\sigma(26°\text{C}) - \sigma(36.5°\text{C})}{n_T \cdot \sigma(26°\text{C})}, \quad \eta_{\varepsilon_r} = \frac{\varepsilon_r(26°\text{C}) - \varepsilon_r(36.5°\text{C})}{n_T \cdot \varepsilon_r(26°\text{C})}, \tag{6.4}$$

where $n_T = 105$ represents the number of discrete thermal steps. The adopted decision of normalizing the total variation against the 26°C baseline provides a dimensionless

sensitivity metric that represents the fractional change relative to the lower thermal state.

The measured data and sensitivities are then compared with the theoretical model in order to assess its reliability in a real scenario. Figure 6.2 illustrates the maximum relative error across the spectrum when comparing the acquisitions to the Debye model. For permittivity ε_r the peak deviation is 3.56% at 1.275 GHz which indicates strong agreement with theoretical predictions. Conversely conductivity σ shows higher relative error at lower frequencies. This occurs because the absolute conductivity of water is extremely low at these frequencies so even minor measurement offsets produce large relative deviations. Furthermore VNA phase noise and algorithm inversion errors become dominant as σ approaches zero. At higher frequencies the relative error for conductivity stabilizes near 7%. Systematic errors are attributed to VNA phase drift thermal inaccuracies and residual ions in the water samples.

Despite these constraints the measured data exhibits the expected linear thermal dependence. Figure 6.3 demonstrates that R^2 exceeds 0.99 for permittivity and 0.98 for conductivity except at 0.5 GHz where accuracy is limited by low absolute values. Tables 6.1 and 6.2 confirm that dielectric parameters can be controlled with high precision where σ shifts by approximately $4.7 \cdot 10^{-4}$% and ε_r by $4.2 \cdot 10^{-2}$% per thermal step.

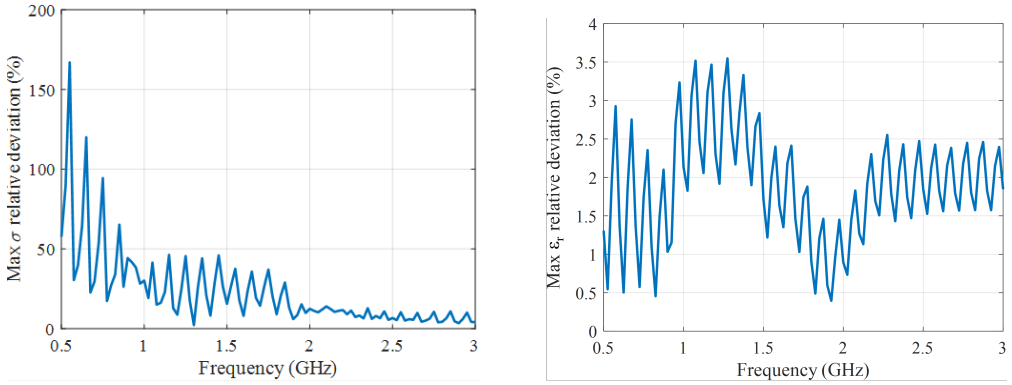

(a) (b)

Figure 6.2: Frequency dependent relative deviation between Debye predictions and empirical data. (a) Maximum error for conductivity. (b) Maximum error for relative permittivity.

To evaluate the capacity of the imaging system to detect subtle dielectric contrasts, such as those present in early stage Parkinson disease, this study simulates localized targets through thermal control. We analyze the microwave signals resulting from these temperature shifts to establish the minimum contrast threshold the system can resolve. Although the absolute properties of water differ from neural tissue, the relative percentage shifts provide a valid metric for characterizing resolution limits. This approach allows us to modulate permittivity and conductivity with high precision and repeatability, eliminating the need for physical reconfiguration of the phantom.

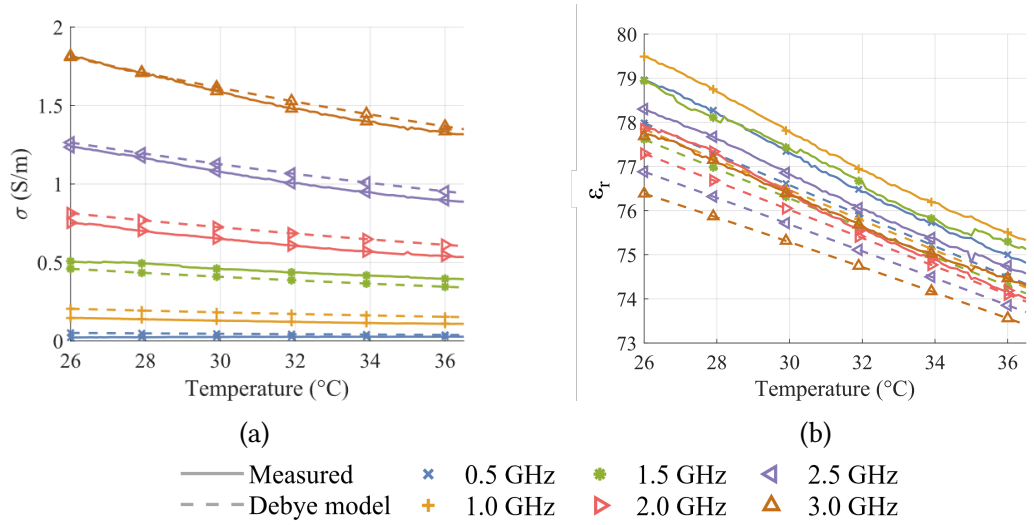

Figure 6.3: Dielectric characteristics of deionized water as a function of thermal state. (a) Conductivity results. (b) Relative permittivity results.

Freq. (GHz)	η_σ Debye (%)	η_σ Measured (%)
0.5	$(1.6 \pm 0.05) \cdot 10^{-4}$	$(6.3 \pm 0.05) \cdot 10^{-5}$
1.0	$(6.4 \pm 0.05) \cdot 10^{-4}$	$(4.4 \pm 0.05) \cdot 10^{-4}$
1.5	$(1.4 \pm 0.05) \cdot 10^{-3}$	$(1.3 \pm 0.05) \cdot 10^{-3}$
2.0	$(2.5 \pm 0.05) \cdot 10^{-3}$	$(2.6 \pm 0.05) \cdot 10^{-3}$
2.5	$(3.9 \pm 0.05) \cdot 10^{-3}$	$(4.1 \pm 0.05) \cdot 10^{-3}$
3.0	$(5.6 \pm 0.05) \cdot 10^{-3}$	$(6.0 \pm 0.05) \cdot 10^{-3}$

Table 6.1: Relative sensitivity of σ per 0.1°C shift at specific frequencies.

Freq. (GHz)	η_{ε_r} Debye (%)	η_{ε_r} Measured (%)
0.5	$(4.4 \pm 0.05) \cdot 10^{-2}$	$(4.9 \pm 0.05) \cdot 10^{-2}$
1.0	$(4.3 \pm 0.05) \cdot 10^{-2}$	$(4.9 \pm 0.05) \cdot 10^{-2}$
1.5	$(4.2 \pm 0.05) \cdot 10^{-2}$	$(4.5 \pm 0.05) \cdot 10^{-2}$
2.0	$(4.0 \pm 0.05) \cdot 10^{-2}$	$(4.6 \pm 0.05) \cdot 10^{-2}$
2.5	$(3.9 \pm 0.05) \cdot 10^{-2}$	$(4.4 \pm 0.05) \cdot 10^{-2}$
3.0	$(3.6 \pm 0.05) \cdot 10^{-2}$	$(4.1 \pm 0.05) \cdot 10^{-2}$

Table 6.2: Relative sensitivity of ε_r per 0.1°C shift at specific frequencies.

6.2 Microwave Imaging System

A Rohde & Schwarz ZNA26 vector network analyzer [151] serves as the core of the acquisition setup, driving four broadband antennas. Building on the protocols defined in [152, 145], this configuration allows for the immediate retrieval of the 4×4 scattering matrix. The use of a native four port interface removes the reliance on auxiliary switching hardware, effectively preserving signal quality.

We selected the frequency range of the VNA to be from 0.5 to 3 GHz (201 points) to balance two competing physical requirements: penetration depth and resolution. Lower frequencies allow deep signal propagation into the brain phantom, while higher frequencies provide shorter wavelengths for better imaging precision. To optimize the acquisition rate without sacrificing stability, the intermediate frequency (IF) bandwidth was set to 10 kHz, achieving total scan times in the tenths of a second. Finally, we utilized an input power of 0 dBm to maximize the signal to noise ratio while keeping the system within the linear operating region of the antennas.

The antenna array consists of two orthogonal pairs arranged along a 100 mm radius circle, matching the scale of the human head. As illustrated in Figure 6.4, Antennas 1 and 2 are spaced by an angular distance of $\alpha = 35°$, with an identical spacing applied to Antennas 3 and 4. This specific topology was derived from cranial imaging studies [152] to solve the problem of mechanical overlap while providing comprehensive angular views. Consequently, the geometric arrangement focuses the interrogation field on the central ROI, allowing for precise monitoring of the SNpc.

The antennas are housed within a cylindrical phantom with an internal radius R_w of 105 mm, providing sufficient clearance for the mounting hardware. Inside this volume, the ROI occupies a circular area with a 100 mm radius on the common transverse plane. The sensors are oriented so that their boresight directions converge at the phantom mid height (50 mm from the base). This geometric optimization ensures high beam density within the ROI, which is critical for improving spatial resolution and mitigating

boundary reflection errors.

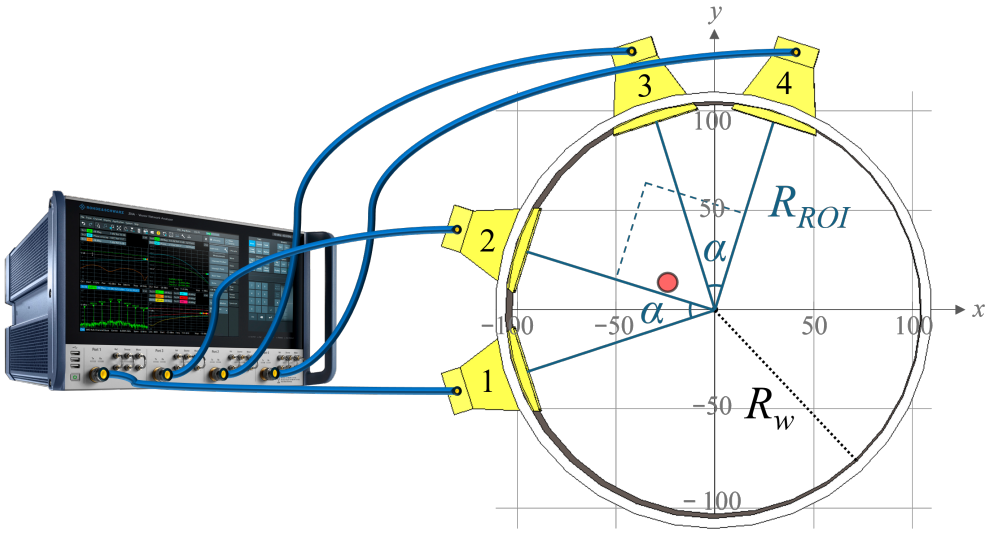

Figure 6.4: Experimental system architecture: (left) Vector network analyzer integration. (right) Geometric antenna distribution within the phantom boundaries. The target coordinate for the dielectric contrast is indicated by the red marker. Grid units are in mm.

6.2.1 Antennas

The system employs four extended gap ridge horn (EGRH) antennas, previously characterized in [153] for biomedical sensing applications. These components are engineered for wideband performance, delivering stable near field characteristics and minimal cross polarization. When interfacing with biological media, the frequency response extends from 0.5 GHz to 3 GHz. This combination of stable spectral behavior and physical compactness makes the EGRH design highly effective for the constraints of this imaging modality.

In this configuration, the antennas operate within deionized water ($\varepsilon_r \approx 74$–79) rather than the originally intended coupling medium ($\varepsilon_r \approx 50$). While the nominal design ensures a reflection coefficient $|S_{11}|$ better than -10 dB (VSWR$\leq$2) up to 1.5 GHz and lower than -5 dB (VSWR$\leq$3.5) up to 3 GHz, the change in background material alters the response. The higher permittivity of the water imposes additional dielectric loading, resulting in a slight deviation of the operating frequency bands from the original specifications.

Figure 6.6 and Figure 6.7 present the measured scattering parameters for reflection (S_{ii}) and transmission (S_{ij}) respectively. All data points were acquired using the spatial arrangement depicted in Figure 6.4 with the array immersed in deionized water. Analysis of the reflection profile in Figure 6.6a shows a consistent magnitude below -5 dB

throughout the spectrum. Furthermore, the plot highlights two distinct operating windows: 0.75 GHz to 0.9 GHz and 2 GHz to 2.3 GHz. In these windows the return loss improves to reflection parameters lower than −10 dB.

Analysis of the spectral response identifies a critical operational boundary at 2.3 GHz. As shown in Figure 6.7a, signal magnitude suffers severe attenuation above this frequency, falling below −80 dB. This energy loss renders the upper spectrum effectively useless for the inverse scattering problem. Furthermore, the phase stability deteriorates in this region; while the response remains coherent at lower frequencies, Figure 6.7b shows a transition to stochastic behavior beyond the 2.3 GHz threshold. Consequently, the reconstruction algorithm is configured to discard this noisy data, focusing exclusively on the bandwidth where the signal to noise ratio guarantees measurement validity.

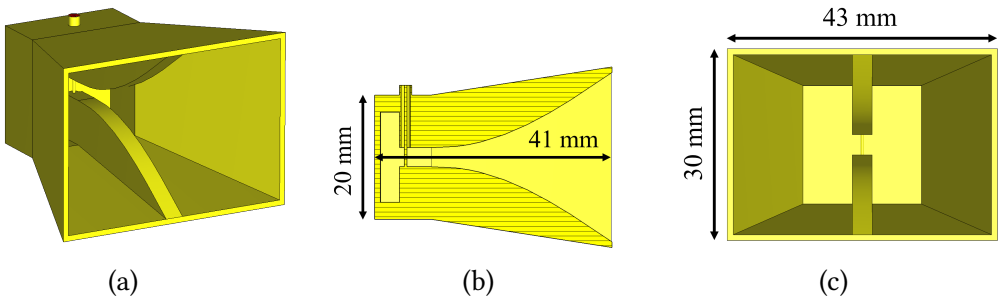

Figure 6.5: Extended gap ridge horn antenna architecture: (a) Isometric 3D view. (b) Longitudinal cross section. (c) Aperture front view.

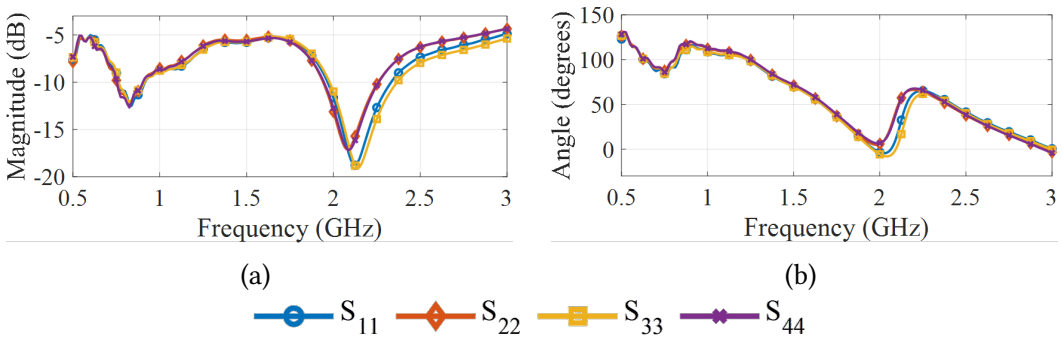

Figure 6.6: Measured reflection coefficients of the sensors immersed in water at 25°C: (a) Magnitude response. (b) Phase response.

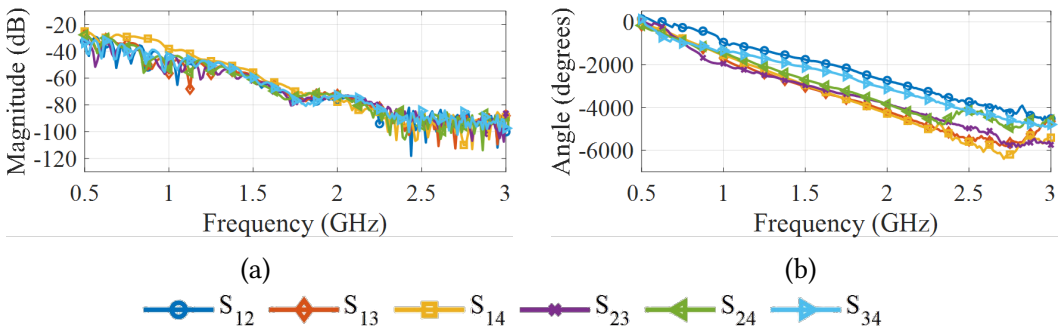

Figure 6.7: Measured transmission coefficients between antenna pairs in water at 25°C: (a) Magnitude response. (b) Phase response.

6.2.2 Phase Center Determination

To ensure the fidelity of the reconstructed image, we performed full wave electromagnetic simulations using a frequency domain solver. The radiated field distribution was analyzed at discrete intervals of 0.1 GHz across the 0.5 GHz to 3 GHz band. This rigorous examination allows for the precise location of the phase center, defined as the theoretical point source from which equiphase wavefronts originate. Accurate determination of this effective origin is critical, as it dictates the reliability of propagation path estimation and the correctness of phase alignment within the imaging algorithm.

During the simulations, the antenna was placed in a homogeneous water environment at a temperature of 25°C, matching the conditions adopted in the experimental measurements. Since the radiation properties of the antenna vary with frequency, the phase center was determined independently at each frequency point. Although the antenna operates in the near-field region, where wavefronts deviate from ideal spherical behavior, the horn geometry provides sufficient symmetry such that, in the area corresponding to the region of interest, the intersection of the wavefronts with the transverse plane yields an approximately circular equiphase contour.

To locate the phase center, we computed the centroid of the equiphase surface points within the transverse plane. The input data was generated from a rectangular computational domain designed to match the physical setup: 200 mm in front of the antenna, 100 mm behind the rear housing, and 200 mm in each transverse direction. By processing the electric field distribution within this specific volume, we ensured the numerical model aligns with the physical capture zone.

To verify the stability of the estimator, we perturbed the simulation domain boundaries by ± 5 mm along each axis. The computed centroid location remained invariant across the full frequency band, confirming that the method is insensitive to minor setup variations. Figure 6.8 presents the resulting phase center distance relative to the aperture, modeled by a fifth order polynomial fit. While the physical response follows a smooth trend, the raw data exhibits slight irregularities, particularly around 2 GHz.

These deviations arise from imperfect wave sphericity and weak numerical reflections from the absorbing boundaries of the computational volume. Despite these minor artifacts, the derived model provides the accuracy required for phase compensation, ensuring precise focusing in multi frequency imaging scenarios.

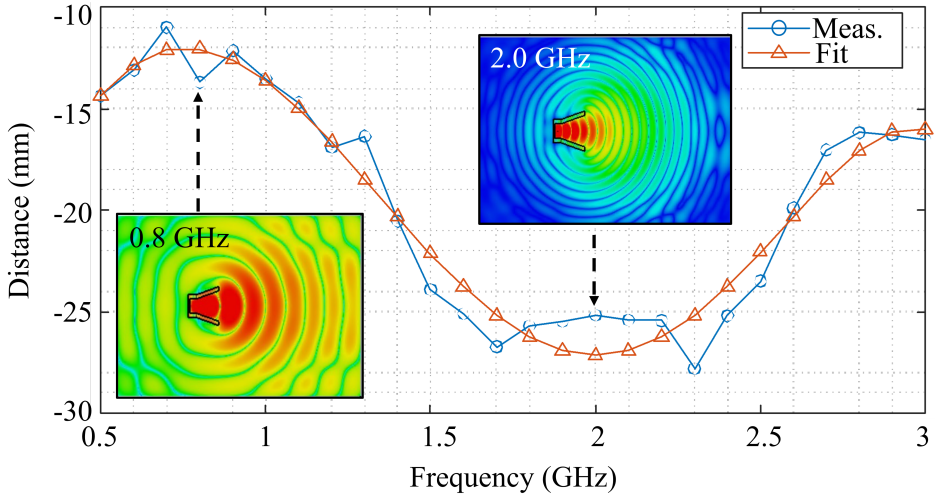

Figure 6.8: Phase center reconstruction: The simulated position of the phase center relative to the antenna aperture is indicated by the blue curve with circular markers, while the red curve with triangular markers shows the corresponding polynomial fit. Representative top-view maps of the electric field distributions employed for the phase center estimation are reported at 0.8 GHz and 2.0 GHz.

6.3 Multi-Frequency Bi-Focusing Imaging Algorithm

The Multi Frequency Bi Focusing (MFBF) algorithm constructs an image by synthetically focusing measured fields rather than solving the full nonlinear inverse scattering problem. For every voxel in the reconstruction domain, the method back propagates both the incident and scattered waves using free space Green's functions. It then coherently sums the contributions from all transmitting receiving antenna pairs across the available spectrum. As detailed in [154], this approach generates an intensity map that identifies regions of strong induced currents. Consequently, the output provides a qualitative localization of scattering structures rather than a quantitative profile of permittivity.

6.3.1 Algorithm Description

The signal processing stage aims to generate a two dimensional image that indicates the position of the dielectric contrast created in the phantom target tube. To achieve this, it is necessary to define a reconstruction zone. The chosen zone covers the entire interior

of the head phantom, and is a circular ROI with a 100 mm radius, with the center of the ROI corresponding to the center of the antenna configuration in 6.4. The imaging process operates on this domain using a grid resolution of 1 mm^2. This specific granularity was selected to ensure the system can resolve small anomalies without incurring excessive computational overhead.

The final spatial image is generated by computing the differential signal between a dynamic test state and a static reference baseline. We established the "healthy" physiological standard using a background measurement where the internal target is stabilized at 40.5°C. The reconstruction engine processes the VNA scattering parameters for each discrete pixel to quantify the contrast against this reference. As the target cools via natural thermal dissipation, its permittivity rises, thereby providing the data necessary to simulate the onset of a pathological condition. For every discrete temperature interval, the differential scattering matrix ΔS is determined as:

$$\Delta S = S_{background} - S_{target} \tag{6.5}$$

where $S_{background}$ is the scattering matrix obtained at the reference healthy temperature and S_{target} is the matrix recorded at the specific pathological temperature under investigation. These differential inputs allow the algorithm to isolate permittivity deviations from the healthy baseline. This methodology is well suited for detecting early stage brain-first PD, where the inherent hemispheric asymmetry allows the contralateral side of the brain to serve as a natural reference standard.

Each pixel in the grid corresponds to a specific focal point (x_{f_p}, y_{f_p}) where the reconstructed intensity is computed via the following summation:

$$I(x_{f_p}, y_{f_p}) = \sum_{f} \sum_{T_i} \sum_{R_j} \frac{\Delta S_{T_i R_j}(f)}{k^2} \cdot e^{jk\rho_{R_j,f_p}} \cdot e^{jk\rho_{T_i,f_p}} \tag{6.6}$$

In this equation, $I(x_{f_p}, y_{f_p})$ is the intensity at the focal point, f represents the operational frequency, and $\Delta S_{T_i R_j}(f)$ is the differential transmission parameter between the transmitting sensor T_i and the receiving sensor R_j. The wavenumber $k(f)$ of the electromagnetic signal within the coupling medium is defined as:

$$k(f) = \frac{2\pi f \sqrt{\varepsilon_r(f)}}{c} \tag{6.7}$$

where $\varepsilon_r(f)$ is the relative permittivity of the background medium and c is the velocity of light in a vacuum. The variables ρ_{T_i,f_p} and ρ_{R_j,f_p} represent the Euclidean distances from the focal point to the respective transmitting and receiving apertures:

$$\rho_{R_j,f_p} = \sqrt{(x_{R_j} - x_{f_p})^2 + (y_{R_j} - y_{f_p})^2}, \qquad \rho_{T_i,f_p} = \sqrt{(x_{T_i} - x_{f_p})^2 + (y_{T_i} - y_{f_p})^2} \tag{6.8}$$

The intensity value assigned to each pixel serves as a dimensionless metric of local dielectric contrast, reflecting the magnitude of permittivity variation relative to the established background.

6.4 Experimental Phantom Design and Fabrication

To quantify the minimum detectable permittivity variations at deep brain coordinates, we engineered a specialized 3D printed head phantom. This design prioritizes experimental repeatability over anatomical realism through two primary structural abstractions. First, we replaced the stratified tissue architecture of the human head with a homogeneous volume of deionized water, thereby eliminating the complex impedance mismatches and variable attenuation rates found in biological environments. Second, the geometry was reduced to a 2D cylindrical format, modeling both the cranial cavity and the SNpc target as vertical cylinders. These simplifications create a controlled test scenario that allows for precise benchmarking, at the cost of yielding a more favorable signal environment than a real cranium.

The phantom structure, shown in Figure 6.9, was manufactured from Polylactic Acid (PLA) using Fused Deposition Modeling (FDM) on an Original Prusa XL system. The vessel features a cylindrical geometry with an internal radius of 105 mm, a wall thickness of 5 mm, and a vertical span of 100 mm. To accommodate the sensing hardware, the design includes four integrated apertures equipped with mechanical supports. These fixtures rigidly position the antenna apertures at a radial distance of 100 mm from the central axis. Finally, the internal cavity is filled with room temperature deionized water, which functions as both the propagation medium and a dielectric matching layer.

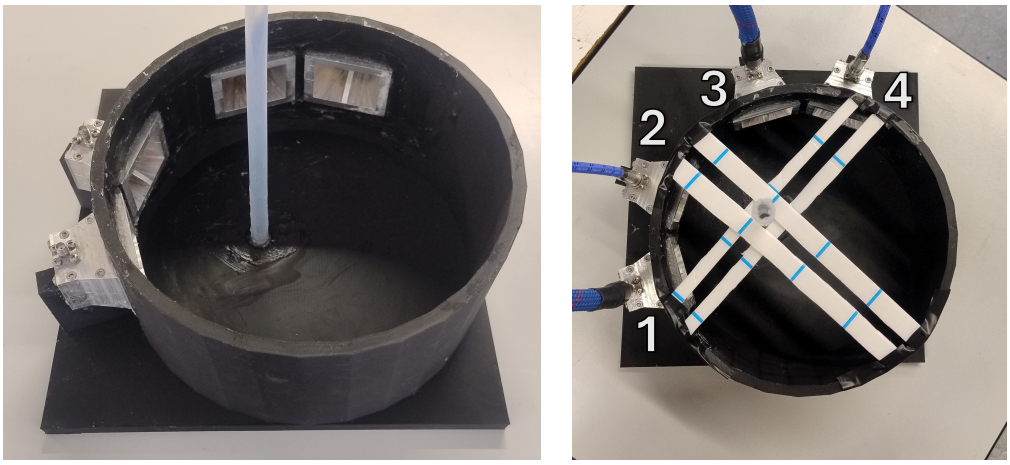

(a) (b)

Figure 6.9: Experimental phantom utilized for system validation: (a) The empty PLA structure prior to VNA integration. (b) The fully assembled and water-filled system during data acquisition. External stabilizing strips were utilized to maintain the vertical alignment of the Teflon target.

To ensure hydraulic integrity, the external antenna surfaces were treated with a conformal lacquer coating, while silicone sealant was applied to the phantom interfaces to create a watertight assembly. Within this sealed volume, we introduced a Teflon tube (8 mm internal diameter, 1 mm wall thickness) to replicate the transverse geometry of the SNpc. Mirroring the lateralized degeneration typical of early stage Parkinson disease [155], the target was mounted at the coordinates x=−25 mm and y=10 mm, as defined in Figure 6.4. The simulation protocol begins with the tube filled with deionized water at 40.5°C, representing the healthy reference state. Subsequent natural thermal dissipation induces a permittivity rise, thereby providing a controlled analog for the dielectric shifts associated with astrogliosis and neuronal attrition.

6.5 Thermal Analysis and Stability of the Phantom Environment

The experimental volume consists of a cylinder filled with water (radius 105 mm, height 100 mm) holding a total capacity of approximately 3.46 L. Within this bulk medium, we positioned a thermal target: a vertical tube defining a 4 mm internal radius, 1 mm wall thickness, and 100 mm length. This subvolume contains a discrete mass of 7.8 g of deionized water raised to an initial temperature of 40.5°C. To quantify the system stability, we calculate the heat capacity C for the specified water mass m using the fundamental expression:

$$C = m\, c_p, \tag{6.9}$$

where $c_p = 4186\,\text{J/(kg·°C)}$ represents the specific heat capacity of water. Based on these parameters, the bulk water volume in the phantom (mass $\approx 3.46\,\text{kg}$) possesses a thermal capacity of approximately $1.45 \times 10^4\,\text{J/°C}$, whereas the water within the localized target (mass $\approx 0.0078\,\text{kg}$) has a significantly lower capacity of roughly $33\,\text{J/°C}$.

The total energy Q dissipated by the target during its cooling phase from 40.5°C to 36°C ($\Delta T = 4.5$°C) is determined by:

$$Q = C_{\text{target}} \cdot \Delta T \approx 148\,\text{J}, \tag{6.10}$$

where C_{target} is the thermal capacity of the internal target volume. Under the conservative assumption that the entirety of this energy is absorbed by the surrounding bulk medium, the resulting temperature shift in the phantom is calculated as:

$$\Delta T_{\text{phantom}} = \frac{Q}{C_{\text{phantom}}} \approx 0.01\text{°C}, \tag{6.11}$$

where C_{phantom} is the thermal capacity of the bulk water volume. Furthermore, the characteristic time constant τ for convective cooling in a water volume V is expressed as:

$$\tau = \frac{\rho c_p V}{hA}, \tag{6.12}$$

The resulting thermal time constant τ ranges from 3 to 6 hours, a value several orders of magnitude greater than the total experimental duration of 237 s. This calculation assumes a standard laboratory environment where the air to water convective heat transfer coefficient h falls between 5 and 10 $\text{Wm}^{-2}\text{K}^{-1}$. Given this significant disparity in time scales, we model the ambient conditions and the bulk phantom temperature as effectively invariant during the measurement window. Consequently, any thermal drift within the coupling medium is considered negligible when compared to the 0.1°C resolution threshold defined for the dielectric characterization. In the governing expression, ρ represents the water density and A corresponds to the exposed surface area.

6.5.1 Measurement Setup and Protocols

System accuracy is established through a calibration procedure utilizing a Rohde & Schwarz ZN-Z151 electronic unit at the antenna reference ports. Once the VNA is ready, the phantom is prepared to simulate the thermal contrast: the main body receives ambient temperature deionized water, while the target cylinder is injected with fluid heated to above 40.5°C. To capture the cooling profile, we employ a digital thermometer with 0.1°C precision to record the target temperature continuously.

The acquisition protocol, illustrated in Figure 6.10, operates within a thermal window of 40.5°C to 36.0°C. Inside this range, the Debye relaxation model predicts a linear shift in dielectric parameters here, ensuring predictable material behavior. As the target cools, S-parameters are recorded for the full array at every 0.1°C decrement. To

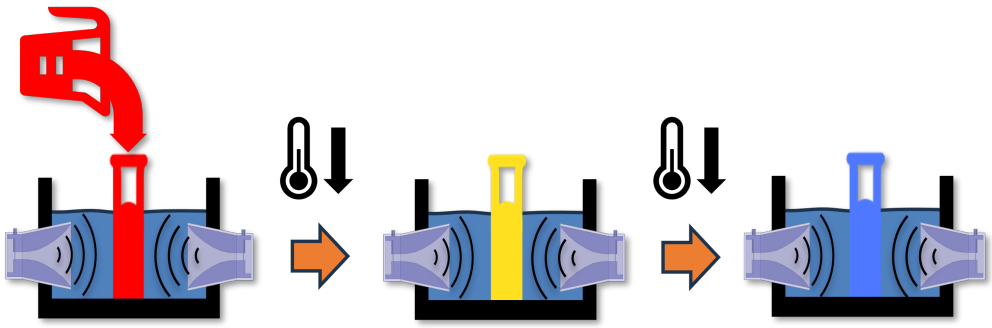

Figure 6.10: Measurement protocol for the PD experiment: hot water (40.5°C) is poured in the target tube and each time a 0.1°C decrease is detected the S-parameters are recorded.

preserve the integrity of these fine grain measurements, the experimental setup is left untouched, preventing any artifacts related to physical movement or vibration.

The acquisition of all 46 experimental samples required a total duration of 237 s, encompassing 45 cooling intervals. Temporal data extracted from the VNA timestamped files indicate that the mean duration for a 0.1°C thermal decrease is 5.27 s with a standard deviation of 0.98 s. Analysis of the cooling rate reveals that the initial 23 intervals occurred more rapidly, with an average duration of 4.78 s (standard deviation 0.99 s), compared to the final 22 intervals, which averaged 5.77 s (standard deviation 0.68 s). This deceleration in the cooling rate is consistent with the reduction in the thermal gradient between the target and the bulk medium as the system approaches room temperature. The resulting scattering data are utilized for sequential image reconstruction to determine the minimum dielectric contrast threshold at which the target becomes spatially resolvable. This threshold serves as a critical benchmark for evaluating system sensitivity relative to the subtle permittivity variations anticipated in the early stages of Parkinson disease.

6.6 Experimental Results and Discussion

To establish a performance baseline, a validation phase is carried out utilizing a high dielectric contrast scenario. We generate differential data by comparing a test case where the target tube only contains air against the case where is contains ambient temperature water. The transmission scattering parameters, plotted in Figure 6.11, show a distinct decline in signal quality for frequencies exceeding 2 GHz. Accordingly, the reconstruction algorithm operates on a bandwidth restricted to the 0.5 GHz to 2 GHz window, for a total of 121 frequency points. As shown in Figure 6.12, the final image accurately resolves the target coordinates, thereby verifying the computational approach.

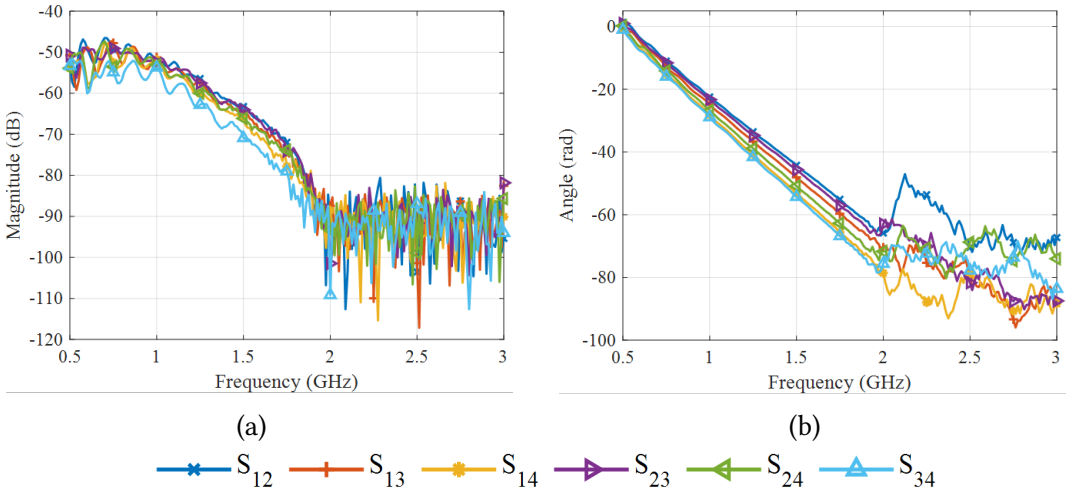

Figure 6.11: Frequency analysis regarding differential transmission scattering parameters. Data reliability decreases above 2 GHz, necessitating the use of the 0.5 to 2 GHz band for imaging. (a) Magnitude. (b) Phase.

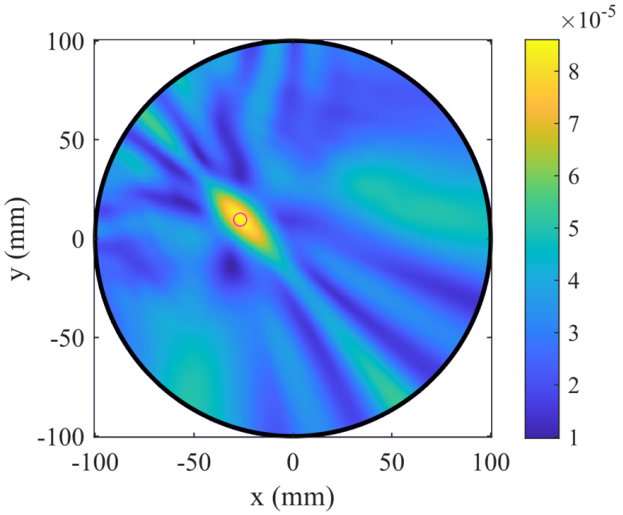

Figure 6.12: Differential reconstruction comparing an air filled target against a water background. The magenta circle denotes the actual target site, which is correctly identified by the algorithm.

The impact of bandwidth and frequency sampling on image quality was evaluated through a series of reconstruction tests. While the signal magnitude approaches the noise floor near 1.9 GHz, including the data up to 2 GHz was found to improve the spatial resolution of the localized target. Truncating the bandwidth below this threshold resulted in a broader main lobe and reduced image sharpness. The 121 frequency points represent the entire dataset acquired during the measurement phase. The necessity of

these points and the selected bandwidth was verified by testing the reconstruction with a reduced subset of the data. This reduction led to a broader main lobe and a general loss of image detail. Consequently, the full frequency range was retained to maximize spatial resolution and ensure the best possible localization of the target.

We evaluated the minimum detectable contrast by analyzing the system response to thermal steps between 0.1°C and 0.9°C (Figure 6.13). The results indicate a specific detection threshold at ΔT=0.4°C; at this value, a distinct intensity peak first emerges at the target location. Conversely, for smaller shifts where $\Delta T \leq 0.3$°C, the signal is insufficient to generate a clear maximum, confirming that the dielectric contrast remains below the noise floor. As the temperature difference widens beyond the 0.4°C threshold, the reconstruction quality improves, characterized by higher peak intensity and tighter spatial confinement.

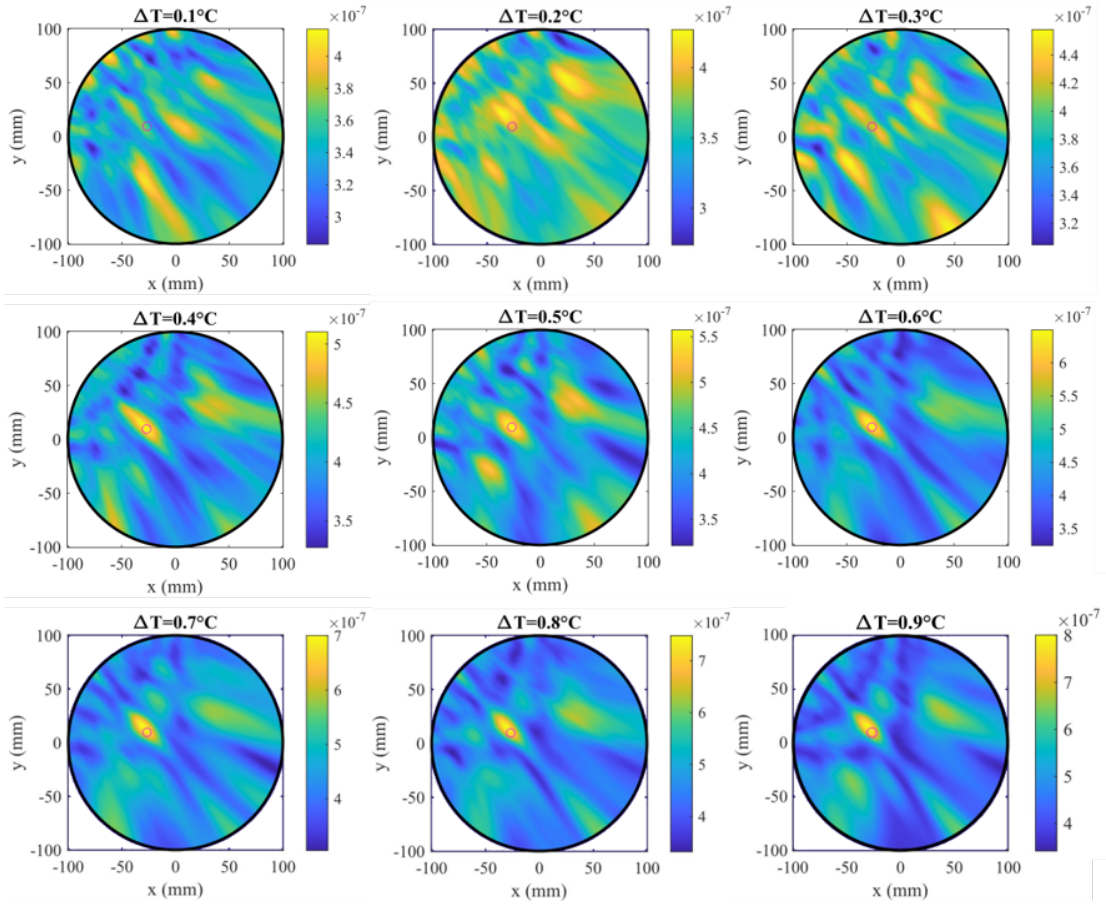

Figure 6.13: Reconstructed differential maps for temperature gradients ΔT between 0.1°C and 0.9°C. The target location is highlighted with a magenta circle in all frames.

Figure 6.14 presents the metric analysis of the imaging results. First, we evaluated

spatial fidelity by calculating the Euclidean distance between the actual target coordinates and the reconstructed maximum; as plotted in Figure 6.14(a), this error metric stabilizes once the thermal gradient reaches 0.4°C. Second, Figure 6.14(b) illustrates the peak magnitude as a function of ΔT. The resulting curve exhibits a linear trend, indicating that the recovered intensity scales proportionally with the permittivity perturbation.

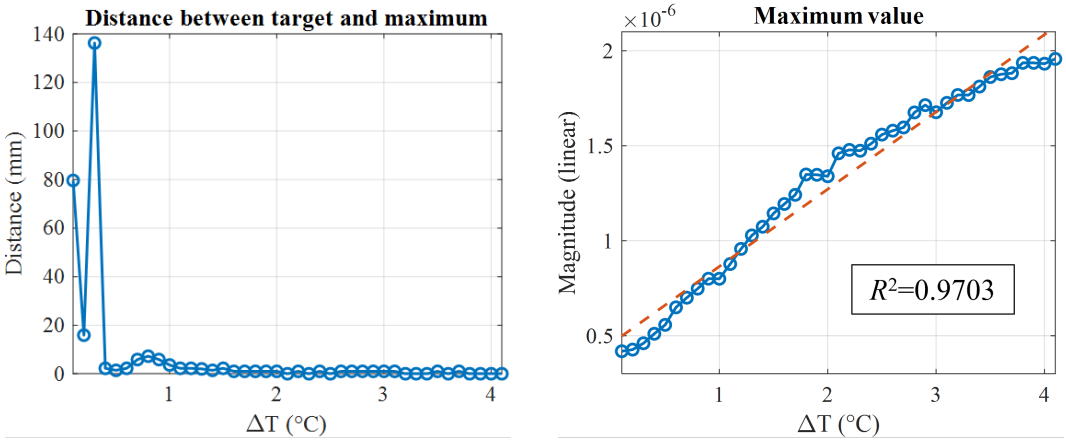

(a) (b)

Figure 6.14: Quantitative reconstruction metrics: (a) spatial offset between the reconstructed peak and the true target center versus ΔT; (b) peak magnitude as a function of ΔT including a linear regression fit. The R^2 value is provided in the inset.

The linear regression presented in Figure 6.14b yields a coefficient of determination $R^2 = 0.9703$, confirming that the imaging output scales predictably with the permittivity variation. This reliable response allows for precise characterization down to a thermal shift of 0.4°C. At this specific operating point, the system resolves relative variations as low as 0.17% for ϵ_r and 0.0047% for σ. Consequently, we establish thermal modulation as a viable and effective tool for evaluating microwave sensor performance under conditions of low dielectric contrast.

Chapter 7

Conclusion and Perspectives

This final chapter synthesizes the research conducted on microwave based sensing and imaging for neurodegenerative disease early detection. By integrating hardware development, numerical modeling, and signal processing, this work establishes a framework for non invasive early detection of Alzheimer's Disease and Parkinson's Disease. Even if the cure for these widespread illnesses has not yet been found, a timely intervention can highly improve the life quality of patients and caregivers. The factors that push the research on microwave techniques for these diseases are mainly two:

- current technologies able to detect the earliest signs of the pathologies are not suitable for mass-screening, because of their cost, bulk, and invasiveness;
- having more and more diverse detection methods allows for pathologies with such a variety of symptoms and physiological changes to be detected with higher accuracy.

7.1 Summary of Contributions

This thesis work is divided in two parts: one regards the exploration of microwave techniques for Alzheimer's disease early detection, carried out at Politecnico di Torino, and the other one is about Parkinson's disease early detection, carried out at Universitat Politécnica de Catalunya.

7.1.1 Alzheimer's disease

Regarding the research activity on AD, the investigation focused on the classification of simulated scenarios where the disease is simulated using permittivity variations in the cerebrospinal fluid inside a dielectric phantom, exploiting neural networks to build the classifier due to the non-linearity and the small differences between the healthy and the pathological scenario simulated.

A first proof-of-concept study was carried out using four antennas adopted from a previous work by our group, where they had been optimized for stroke detection. The phantom employed in this experiment was not specifically designed for the present application; however, it could be emptied and refilled with custom liquids representing healthy and pathological CSF. A measurement campaign was conducted by acquiring the antennas' scattering parameters when placed on the phantom filled with liquids simulating the healthy condition and different severities of Alzheimer's disease, thereby generating a labeled dataset. Various training, validation, and test splits of this dataset were then used to train, optimize, and evaluate machine-learning binary classifiers, specifically MLP, to distinguish between the healthy and the pathological cases. Despite the non-optimized experimental setup, this approach achieved high binary classification accuracy on the test data, over 90%, motivating the development of a more advanced system and a more realistic experimental framework to further assess feasibility in real-case scenarios.

The new microwave sensing system employed six wideband antennas specifically optimized for this application. A realistic multitissue head phantom was fabricated, with particular improvements to the thickness, dielectric properties, and geometry of the outer layers (i.e., the solid components external to the brain). The dimensions of the CSF layer were also refined, and the pathological CSF-mimicking liquids were formulated to more closely replicate real-case dielectric properties. The measurement campaign produced a balanced dataset comprising healthy and pathological cases and was conducted over three days, with data collected on the final day reserved exclusively for testing. Two different strategies for splitting the remaining data into training and validation sets were investigated: one based on class labels and the other based on measurement sessions. For each strategy, three training–validation ratios were evaluated (60:40, 70:30, and 80:20). The dataset was further expanded using a data augmentation technique. Data processing again relied on a MLP classification architecture. By leveraging data augmentation to enhance dataset diversity, the system achieved a binary classification accuracy exceeding 94%. Moreover, a multiclass f1-score above 87% was obtained when distinguishing between different levels of pathological severity. These results demonstrate the capability of machine-learning approaches to extract diagnostically relevant features from complex scattering-parameter data.

These results represent a significant advancement over previous microwave sensing studies for neurodegeneration. Existing literature often focuses on brain atrophy, a structural change that occurs in the later stages of the disease. In contrast, this work targets the early accumulation of amyloid and tau proteins in the cerebrospinal fluid by detecting their specific dielectric signatures. By achieving a classification accuracy of 94% within a realistic multi tissue environment, this research bridges the gap between theoretical feasibility and practical clinical implementation.

In the broader landscape of early detection, blood based biomarkers have recently demonstrated high diagnostic precision in clinical settings. However, microwave sensing offers a distinct and complementary advantage. While blood tests measure systemic

concentrations of biomarkers, microwave techniques provide an in situ assessment of the brain environment. This enables the detection of localized physiological changes without the need for invasive sampling or specialized laboratory processing required for blood analysis.

Furthermore, the complexity of Alzheimer's disease requires a multi modal diagnostic strategy. No single biomarker or test is currently sufficient to capture the full heterogeneity of the pathology across diverse patient populations. Integrating microwave sensing into a broader screening framework alongside digital cognitive tools and fluid biomarkers allows for ensemble prediction. This diversity in detection methods increases overall diagnostic accuracy by cross validating findings across different physiological indicators. Providing a suite of non invasive, low cost tools is essential for mass screening programs, ensuring that early intervention can be initiated with higher confidence and broader accessibility.

7.1.2 Parkinson's disease

The second contribution focused on the detection of PD using microwave imaging techniques. A four-antenna measurement setup was combined with a multi-frequency bifocusing algorithm to localize small dielectric anomalies associated with PD-related physiological alterations in the brain. The system employed horn antennas specifically designed for microwave imaging applications on the human body, ensuring wideband operation and adequate spatial resolution. Experimental validation was performed using a dynamic cylindrical phantom designed and created for this specific application, which enabled controlled and repeatable testing conditions. The phantom consists of a bowl filled with room-temperature water, featuring dedicated openings for antenna placement, inside which a tube containing hotter water is positioned. A key novelty of this work lies in the controlled regulation of dielectric contrast within the target tube, which represents the substantia nigra pars compacta region where PD-related changes are most pronounced. This contrast was precisely controlled by adjusting the temperature of deionized water and exploiting its well-known temperature-dependent dielectric properties. This approach allowed for fine-grained emulation of pathological variations that are difficult to reproduce with static phantoms.

The experimental results demonstrated that the proposed system is sensitive to relative permittivity variations as small as 0.17%, highlighting its capability to detect subtle physiological changes. Furthermore, this study introduced a symmetry-based processing strategy that leverages the inherent left–right asymmetry observed in early-stage, brain-first PD. By using the contralateral hemisphere as an internal reference, this method has the potential to eliminate the need for subject-specific baseline measurements, thereby improving clinical practicality and robustness.

In the context of the current literature, the developed system addresses two major bottlenecks in microwave imaging. First, the introduction of the temperature controlled dynamic phantom overcomes the limitations of static dielectric targets, providing a benchmark for emulating physiological changes with a precision of $4.2 \cdot 10^{-2}\%$. The dynamicity of the phantom allows switching between healthy and pathologic states without invasive modifications that could alter the measurement. This provides a significantly finer level of control compared to state of the art phantoms. Second, the symmetry based processing strategy offers a solution to the reference problem prevalent in microwave imaging. Whereas standard differential imaging techniques typically require a healthy baseline measurement of the same patient, this work leverages anatomical symmetry to provide an internal reference. This shift from absolute to relative hemispheric sensing positions microwave imaging as a viable tool for longitudinal monitoring of PD.

Beyond these technical milestones, the work introduces a new modality to the existing landscape of Parkinson's Disease screening. Current clinical diagnosis relies heavily on the observation of motor symptoms, which manifest only after significant degradation of the SNpc. By targeting the early dielectric variations associated with these physiological changes, microwave imaging provides a unique diagnostic angle. Incorporating this technology into a multimodal framework alongside other emerging tools, such as digital biomarkers from wearable sensors or biochemical assays, increases the overall precision of the screening process. Given the widespread prevalence of PD, the availability of diverse noninvasive technologies is critical. A redundant sensing approach ensures that the disease is detected through independent physical markers, leading to more robust early intervention strategies and better management of the pathology.

7.2 Open Challenges and Future Directions

Research into microwave sensing and imaging for neurodegenerative diseases detection is still in its early stages. Several technical parameters require further exploration, as antenna array configurations, signal processing algorithms for image reconstruction or classification, and the development of high fidelity phantoms. Currently, simulating Alzheimer's and Parkinson's disease within computational or physical environments is limited by incomplete clinical understanding and significant interpatient physiological variability.

Ultimately, the goal is to initiate in-vivo pilot studies to validate the performance of these microwave systems in real biological conditions, paving the way for low cost, portable, and non ionizing neurodiagnostic tools.

7.2.1 Alzheimer's disease

Even if the results are promising, several steps remain before clinical translation. A primary limitation is the discrepancy between laboratory phantoms and the high complexity of real human anatomy. While the phantoms used in this research included multiple tissue layers, they do not fully capture the stochastic nature of biological tissue distribution or the presence of hair and skin irregularities. The limitation of only having one phantom was coped using a data augmentation technique, but it is necessary to have hundreds, if not thousands, of different head models to acquire the data diversity necessary to reproduce the real diversity of human physiology.

Furthermore, the sensitivity of the system to motion artifacts and environmental noise presents an engineering challenge. In a clinical setting, patient movement could introduce phase shifts that mask the subtle dielectric changes caused by disease. Beyond motion artifacts, the impact of repositioning error is a critical factor for the practical use of this technology. This study serves as a proof of concept conducted under strictly controlled laboratory conditions where antenna placement remained constant. In a clinical scenario involving repeated scans over time, achieving identical positioning for every session is unlikely. Because the dielectric variations associated with the early stages of Alzheimer or Parkinson are extremely small, the signal variations caused by slight antenna misalignments could potentially exceed the target physiological signal. To address this challenge, future work must focus on the robustness of the classification algorithms. We anticipate that expanding the training dataset to include multiple antenna orientations and diverse subject alignments will improve the system capacity to generalize. By training the machine learning models on data that explicitly accounts for these physical variations, the algorithm should learn to distinguish relevant permittivity changes in the CSF from the noise introduced by repositioning. Quantifying these effects and establishing clear tolerances for sensor placement will be essential steps in transitioning this prototype into a reliable diagnostic tool for real world medical environments.

A different strategy for AD detection that is being explored is the possibility of imaging the CSF inside the spinal cord by applying the antennas on the neck surface. Preliminary numerical analysis indicates that this approach is technically feasible [156].

Further experimental characterization of healthy and pathological CSF is required to establish the precise correlation between protein concentration and dielectric permittivity variations. Defining this relationship is critical for validating the sensitivity of microwave systems to the biochemical changes associated with neurodegeneration.

7.2.2 Parkinson's disease

The experiments were conducted in a highly simplified scenario. Future work on this microwave imaging application will require more realistic experimental conditions, including phantoms that reproduce the complexity of a multitissue environment and more

closely resemble the geometry of the human head.

In addition, a deeper understanding of the dielectric changes occurring in the brain as a result of Parkinson's disease is necessary to accurately model the early-stage dielectric contrast associated with the pathology. Such knowledge will enable feasibility studies to be carried out in close-to-realistic environments, particularly to assess the potential of exploiting the asymmetrical alterations characteristic of brain-first Parkinson's disease for reliable detection.

Bibliography

[1] Nazish Khalid et al. "Emerging paradigms in microwave imaging technology for biomedical applications: unleashing the power of artificial intelligence." In: *npj Imaging* 2.1 (2024), p. 13. DOI: 10.1038/s44303-024-00012-8.

[2] Cristina Origlia et al. "Review of microwave near-field sensing and imaging devices in medical applications." In: *Sensors* 24.14 (2024), p. 4515. DOI: 10.3390/s24144515.

[3] *Radio Regulations*. Most recent edition. Definitions of UHF, SHF, and EHF bands. Geneva, Switzerland, 2020.

[4] *IEEE Standard Letter Designations for Radar-Frequency Bands*. 2003. DOI: 10.1109/IEEESTD.2003.1197645.

[5] Camelia Gabriel, Sami Gabriel, and YE Corthout. "The dielectric properties of biological tissues: I. Literature survey." In: *Physics in medicine & biology* 41.11 (1996), p. 2231.

[6] Kenneth S Cole and Robert H Cole. "Dispersion and absorption in dielectrics I. Alternating current characteristics." In: *The Journal of chemical physics* 9.4 (1941), pp. 341–351. DOI: 10.1063/1.1750906.

[7] Karl J Bois, Aaron D Benally, and Reza Zoughi. "Microwave near-field reflection property analysis of concrete for material content determination." In: *IEEE Transactions on Instrumentation and measurement* 49.1 (2002), pp. 49–55. DOI: 10.1109/19.836308.

[8] Vittorio Memmolo et al. "Ultra-wideband microwave leakage monitoring for stringer debonding detection in carbon composite fuselage structures." In: *NDT & E International* 142 (2024), p. 103006. DOI: 10.1016/j.ndteint.2023.103006.

[9] Danladi Agadi Tonga et al. "Nondestructive Evaluation of Fiber-Reinforced polymer using Microwave techniques: A review." In: *Coatings* 13.3 (2023), p. 590. DOI: 10.3390/coatings13030590.

[10] Samir Trabelsi and Stuart O. Nelson. "Microwave sensing of quality attributes of agricultural and food products." In: *IEEE Instrumentation & Measurement Magazine* 19.1 (2016), pp. 36–41. DOI: 10.1109/MIM.2016.7384959.

[11] Jorge A Tobon Vasquez et al. "Noninvasive inline food inspection via microwave imaging technology: An application example in the food industry." In: *IEEE Antennas and Propagation Magazine* 62.5 (2020), pp. 18–32. DOI: 10.1109/MAP.2020.3012898.

[12] Ala Eldin Omer et al. "Low-cost portable microwave sensor for non-invasive monitoring of blood glucose level: Novel design utilizing a four-cell CSRR hexagonal configuration." In: *Scientific Reports* 10.1 (2020), p. 15200. DOI: 10.1038/s41598-020-72114-3.

[13] Carlos G Juan et al. "Microwave planar resonant solutions for glucose concentration sensing: A systematic review." In: *Applied Sciences* 11.15 (2021), p. 7018. DOI: 10.3390/app11157018.

[14] Ebbe Nyfors. "Industrial microwave sensors—A review." In: *Subsurface Sensing Technologies and Applications* 1.1 (2000), pp. 23–43. DOI: 10.1023/A:1010118609079.

[15] Mengke Zhan, Cheng-Gang Xie, and Jian-Jun Shu. "Microwave probe sensing location for Venturi-based real-time multiphase flowmeter." In: *Journal of Petroleum Science and Engineering* 218 (2022), p. 111027. DOI: 10.48550/arXiv.2210.00622.

[16] Adel Omrani et al. "An electromagnetic time-reversal imaging algorithm for moisture detection in polymer foam in an industrial microwave drying system." In: *Sensors* 21.21 (2021), p. 7409. DOI: 10.3390/s21217409.

[17] Ilaria Catapano et al. "A tomographic approach for helicopter-borne ground penetrating radar imaging." In: *IEEE Geoscience and Remote Sensing Letters* 9.3 (2011), pp. 378–382. DOI: 10.1109/LGRS.2011.2169390.

[18] Sherif S. Ahmed. "Microwave Imaging in Security — Two Decades of Innovation." In: *IEEE Journal of Microwaves* 1.1 (2021), pp. 191–201. DOI: 10.1109/JMW.2020.3035790.

[19] Lawrence E Larsen and John H Jacobi. "Medical applications of microwave imaging." In: *IEEE Press: New York, NY, USA* 32 (1985).

[20] E.C. Fear and M.A. Stuchly. "Microwave detection of breast cancer." In: *IEEE Transactions on Microwave Theory and Techniques* 48.11 (2000), pp. 1854–1863. DOI: 10.1109/22.883862.

[21] M Guardiola et al. "3-D microwave magnitude combined tomography for breast cancer detection using realistic breast models." In: *IEEE antennas and wireless propagation letters* 11 (2012), pp. 1622–1625. DOI: 10.1109/LAWP.2012.2235813.

[22] Mario R Casu et al. "A COTS-based microwave imaging system for breast-cancer detection." In: *IEEE transactions on biomedical circuits and systems* 11.4 (2017), pp. 804–814. DOI: 10.1109/TBCAS.2017.2703588.

[23] Maged A Aldhaeebi et al. "Review of microwaves techniques for breast cancer detection." In: *Sensors* 20.8 (2020), p. 2390. DOI: 10.3390/s20082390.

[24] Soumya Prakash Rana et al. "Radiation-free microwave technology for breast lesion detection using supervised machine learning model." In: *Tomography* 9.1 (2023), pp. 105–129. DOI: 10.3390/tomography9010010.

[25] Andreas Fhager et al. "Microwave diagnostics ahead: Saving time and the lives of trauma and stroke patients." In: *IEEE Microwave Magazine* 19.3 (2018), pp. 78–90. DOI: 10.1109/MMM.2018.2801646.

[26] David O Rodriguez-Duarte et al. "Experimental assessment of real-time brain stroke monitoring via a microwave imaging scanner." In: *IEEE Open Journal of Antennas and Propagation* 3 (2022), pp. 824–835. DOI: 10.1109/OJAP.2022.3192884.

[27] Lei Guo, Abdulrahman S. M. Alqadami, and Amin Abbosh. "Stroke Diagnosis Using Microwave Techniques: Review of Systems and Algorithms." In: *IEEE Journal of Electromagnetics, RF and Microwaves in Medicine and Biology* 7.2 (2023), pp. 122–135. DOI: 10.1109/JERM.2022.3227724.

[28] Imran M. Saied and Tughrul Arslan. "Noninvasive Wearable RF Device Towards Monitoring Brain Atrophy and Lateral Ventricle Enlargement." In: *IEEE Journal of Electromagnetics, RF and Microwaves in Medicine and Biology* 4.1 (2020), pp. 61–68. DOI: 10.1109/JERM.2019.2926163.

[29] Xin Chen et al. "A deep learning approach for non-invasive Alzheimer's monitoring using microwave radar data." In: *Neural Networks* (2024), p. 106778. DOI: 10.1016/j.neunet.2024.106778.

[30] Reefat Inum et al. "EBG based microstrip patch antenna for brain tumor detection via scattering parameters in microwave imaging system." In: *International journal of biomedical imaging* 2018.1 (2018), p. 8241438. DOI: 10.1155/2018/8241438.

[31] Amran Hossain et al. "Microwave brain imaging system to detect brain tumor using metamaterial loaded stacked antenna array." In: *Scientific reports* 12.1 (2022), p. 16478. DOI: 10.1038/s41598-022-20944-8.

[32] Leonardo Cardinali et al. "A Machine Learning Approach to Microwave Sensing for Non-Invasive Alzheimer's Disease Early Detection." In: *2023 IEEE International Conference on Metrology for eXtended Reality, Artificial Intelligence and Neural Engineering (MetroXRAINE)*. IEEE. 2023, pp. 507–512. DOI: 10.1109/MetroXRAINE58569.2023.10405555.

[33] Leonardo Cardinali et al. "A microwave sensing system enhanced by a machine learning algorithm for alzheimer's disease early detection." In: *2023 IEEE Conference on Antenna Measurements and Applications (CAMA)*. IEEE. 2023, pp. 723–727. DOI: 10.1109/CAMA57522.2023.10352785.

[34] L Cardinali et al. "Feasibility of Alzheimer's Disease Early Detection Through Machine Learning Applied to Microwave Sensing Data Collected from a Realistic Phantom." In: *2024 IEEE International Symposium on Antennas and Propagation and INC/USNC-URSI Radio Science Meeting (AP-S/INC-USNC-URSI)*. IEEE. 2024, pp. 241–242. DOI: 10.1109/AP-S/INC-USNC-URSI52054.2024.10686512.

[35] L. Cardinali et al. "Early Detection of Alzheimer's Disease via Machine Learning-Based Microwave Sensing: An Experimental Validation." In: *Sensors* (2025). In press.

[36] Leonardo Cardinali et al. "Differential Permittivity Modeling in Biological Phantoms via Water Temperature Control." In: *2025 International Conference on Electromagnetics in Advanced Applications (ICEAA)*. IEEE. 2025, pp. 1100–1102. DOI: 10.1109/ICEAA65662.2025.11305745.

[37] Leonardo Cardinali et al. "Microwave Imaging for Parkinson's Disease Detection: A Phantom-Based Feasibility Study Using Temperature-Controlled Dielectric Variations." In: *Sensors* 25.24 (2025), p. 7562. DOI: 10.3390/s25247562.

[38] National Institute on Aging. *What Are the Signs of Alzheimer's Disease?* Available online: https://www.nia.nih.gov/health/alzheimers-symptoms-and-diagnosis/what-are-signs-alzheimers-disease (accessed on: Dec. 4, 2025).

[39] World Health Organization. *Dementia*. Available online: https://www.who.int/news-room/fact-sheets/detail/dementia (accessed on: Dec. 4, 2025).

[40] Lindsay A Farrer et al. "Effects of age, sex, and ethnicity on the association between apolipoprotein E genotype and Alzheimer disease: a meta-analysis." In: *Jama* 278.16 (1997), pp. 1349–1356. DOI: 10.1001/jama.1997.03550160069041.

[41] Margaret Gatz et al. "Role of genes and environments for explaining Alzheimer disease." In: *Archives of general psychiatry* 63.2 (2006), pp. 168–174.

[42] JA Luchsinger et al. "Aggregation of vascular risk factors and risk of incident Alzheimer disease." In: *Neurology* 65.4 (2005), pp. 545–551. DOI: 10.1212/01.wnl.0000172914.08967.dc.

[43] Marcos Vinícius Ferreira Silva et al. "Alzheimer's disease: risk factors and potentially protective measures." In: *Journal of biomedical science* 26.1 (2019), p. 33. DOI: 10.1186/s12929-019-0524-y.

[44] Yunhwan Lee et al. "Systematic review of health behavioral risks and cognitive health in older adults." In: *International psychogeriatrics* 22.2 (2010), pp. 174–187. DOI: 10.1017/S1041610209991189.

[45] Fan Jiang et al. "A comprehensive evaluation on the associations between hearing and vision impairments and risk of all-cause and cause-specific dementia: results from cohort study, meta-analysis and Mendelian randomization study." In: *BMC medicine* 22.1 (2024), p. 518. DOI: 10.1186/s12916-024-03748-7.

[46] Zoltan Ungvari et al. "Sleep disorders increase the risk of dementia, Alzheimer's disease, and cognitive decline: A meta-analysis." In: *GeroScience* (2025), pp. 1–22. DOI: 10.1007/s11357-025-01637-2.

[47] Aaron Jones et al. "Environmental risk factors for all-cause dementia, Alzheimer's disease dementia, vascular dementia, and mild cognitive impairment: An umbrella review and meta-analysis." In: *Environmental research* 270 (2025), p. 121007. DOI: 10.1016/j.envres.2025.121007.

[48] Robert S Wilson et al. "Loneliness and risk of Alzheimer disease." In: *Archives of general psychiatry* 64.2 (2007), pp. 234–240. DOI: 10.1001/archpsyc.64.2.234.

[49] G. McKhann *et al.* "The diagnosis of dementia due to Alzheimer's disease: Recommendations from the National Institute on Aging-Alzheimer's Association workgroups on diagnostic guidelines for Alzheimer's disease." In: *Alzheimer's and Dementia* 7.3 (2011), pp. 263–269. ISSN: 1552-5260. DOI: 10.1016/j.jalz.2011.03.005.

[50] Fabienne Collette, Martial Van der Linden, and Eric Salmon. "Executive dysfunction in Alzheimer's disease." In: *Cortex* 35.1 (1999), pp. 57–72. DOI: 10.1016/s0010-9452(08)70785-8.

[51] Bokyoung Kim, Gie Ok Noh, and Kyunghee Kim. "Behavioural and psychological symptoms of dementia in patients with Alzheimer's disease and family caregiver burden: a path analysis." In: *BMC geriatrics* 21.1 (2021), p. 160. DOI: 10.1186/s12877-021-02109-w.

[52] Qing-Fei Zhao et al. "The prevalence of neuropsychiatric symptoms in Alzheimer's disease: systematic review and meta-analysis." In: *Journal of affective disorders* 190 (2016), pp. 264–271. DOI: 10.1016/j.jad.2015.09.069.

[53] Ane Alberdi, Asier Aztiria, and Adrian Basarab. "On the early diagnosis of Alzheimer's Disease from multimodal signals: A survey." In: *Artificial Intelligence in Medicine* 71 (2016), pp. 1–29. ISSN: 0933-3657. DOI: 10.1016/j.artmed.2016.06.003. URL: https://www.sciencedirect.com/science/article/pii/S0933365716300732.

[54] E. M. Reiman *et al.* "Brain imaging and fluid biomarker analysis in young adults at genetic risk for autosomal dominant Alzheimer's disease in the presenilin 1 E280A kindred: a case-control study." In: *The Lancet Neurology* 11.12 (2012), pp. 1048–1056. DOI: 10.1016/S1474-4422(12)70228-4.

[55] Ana Lloret et al. "When does Alzheimer′ s disease really start? The role of biomarkers." In: *International journal of molecular sciences* 20.22 (2019), p. 5536. DOI: 10.3390/ijms20225536.

[56] Jianping Jia et al. "Biomarker changes during 20 years preceding Alzheimer's disease." In: *New England Journal of Medicine* 390.8 (2024), pp. 712–722. DOI: 10.1056/NEJMoa2310168.

[57] Marta Milà-Alomà et al. "Amyloid beta, tau, synaptic, neurodegeneration, and glial biomarkers in the preclinical stage of the Alzheimer's continuum." In: *Alzheimer's & Dementia* 16.10 (2020), pp. 1358–1371. DOI: 10.1002/alz.12131.

[58] Clifford R Jack et al. "Tracking pathophysiological processes in Alzheimer's disease: an updated hypothetical model of dynamic biomarkers." In: *The lancet neurology* 12.2 (2013), pp. 207–216. DOI: 10.1016/S1474-4422(12)70291-0.

[59] Kaj Blennow and Henrik Zetterberg. "Biomarkers for Alzheimer's disease: current status and prospects for the future." In: *Journal of internal medicine* 284.6 (2018), pp. 643–663. DOI: 10.1111/joim.12816.

[60] Simiao Chen et al. "The global macroeconomic burden of Alzheimer's disease and other dementias: estimates and projections for 152 countries or territories." In: *The Lancet Global Health* 12.9 (2024), e1534–e1543. DOI: 10.1016/S2214-109X(24)00264-X.

[61] Guy McKhann et al. "Clinical diagnosis of Alzheimer's disease." In: *Neurology* 34.7 (1984), pp. 939–939. DOI: 10.1212/WNL.34.7.939.

[62] Ingrid Arevalo-Rodriguez et al. "Mini-Mental State Examination (MMSE) for the detection of Alzheimer's disease and other dementias in people with mild cognitive impairment (MCI)." In: *Cochrane database of systematic reviews* 3 (2015). DOI: 10.1002/14651858.CD010783.pub2.

[63] John Hobson. "The montreal cognitive assessment (MoCA)." In: *Occupational Medicine* 65.9 (2015), pp. 764–765. DOI: 10.1093/occmed/kqv078.

[64] John C Morris. "Clinical dementia rating: a reliable and valid diagnostic and staging measure for dementia of the Alzheimer type." In: *International psychogeriatrics* 9 (1997), pp. 173–176. DOI: 10.1017/S1041610297004870.

[65] Sharpley Hsieh et al. "Validation of the Addenbrooke's Cognitive Examination III in frontotemporal dementia and Alzheimer's disease." In: *Dementia and geriatric cognitive disorders* 36.3-4 (2013), pp. 242–250. DOI: 10.1159/000351671.

[66] Joella E Storey et al. "The Rowland universal dementia assessment scale (RUDAS): a multicultural cognitive assessment scale." In: *International Psychogeriatrics* 16.1 (2004), pp. 13–31. DOI: 10.1017/S1041610204000043.

[67] Wiesje M Van Der Flier and Philip Scheltens. "The ATN framework—moving preclinical Alzheimer disease to clinical relevance." In: *JAMA neurology* 79.10 (2022), pp. 968–970. DOI: 10.1001/jamaneurol.2022.2967.

[68] Hejie Li and Zhe Wang. "Blood biomarkers for clinical applications in Alzheimer's disease: A narrative review." In: *NeuroMarkers* 2.2 (2025), p. 100078. DOI: 10.1016/j.neumar.2025.100078.

[69] Mauro Silvestrini et al. "Carotid atherosclerosis and cognitive decline in patients with Alzheimer's disease." In: *Neurobiology of aging* 30.8 (2009), pp. 1177–1183. DOI: 10.1016/j.neurobiolaging.2007.11.008.

[70] Giovanna Viticchi et al. "Vascular predictors of cognitive decline in patients with mild cognitive impairment." In: *Neurobiology of aging* 33.6 (2012), 1127–e1. DOI: 10.1016/j.neurobiolaging.2011.11.027.

[71] I. Saied, T. Arslan, et al. "Microwave Characterization of Brain Tissue and Modeling for Neurodegenerative Disease Detection." In: *IEEE Transactions on Medical Imaging* (2020). DOI: 10.1109/TMI.2020.3011359.

[72] R. Ullah, I. Saied, and T. Arslan. "Microwave-Based Detection of Brain Atrophy Using Wearable Antenna Arrays." In: *Biomedical Signal Processing and Control* 71 (2022), p. 103083. DOI: 10.1016/j.bspc.2021.103083.

[73] R. Ullah, I. Saied, and T. Arslan. "Microwave S-Parameter Dataset for Brain Atrophy Assessment." In: *Data in Brief* (2023). DOI: 10.1016/j.dib.2023.109006.

[74] Farhatullah, Xin Chen, et al. "A Deep Learning Approach for Non-Invasive Alzheimer's Monitoring Using Microwave Radar Data." In: *Neural Networks* (2024). DOI: 10.1016/j.neunet.2024.106123.

[75] C. Liu et al. "Microwave Sensors and Their Applications in Permittivity Measurement." In: *Sensors* (2024). DOI: 10.3390/s24041234.

[76] Xin Chen et al. "A deep learning approach for non-invasive Alzheimer's monitoring using microwave radar data." In: *Neural Networks* (2024), p. 106778. DOI: 10.1016/j.neunet.2024.106778.

[77] T Yoshikawa et al. "Biosensing of interaction between phospholipid membrane of liposome as model cell membrane and amyloid-beta protein in human serum by dielectric dispersion analysis." In: *Sensors and Actuators B: Chemical* 236 (2016), pp. 1028–1035. DOI: 10.1016/j.snb.2016.04.185.

[78] Mohamed Manoufali et al. "Implantable sensor for detecting changes in the loss tangent of cerebrospinal fluid." In: *IEEE Transactions on biomedical circuits and systems* 14.3 (2020), pp. 452–462. DOI: 10.1109/TBCAS.2020.2973387.

[79] Caiyi Liao, Zheng Gong, and Yifan Chen. "A Generalized Quantitative Microwave Medical Sensing and Imaging System for the Detection of Alzheimer's Disease." In: *2024 Photonics & Electromagnetics Research Symposium (PIERS)*. [CrossRef]. IEEE. 2024, pp. 1–6. DOI: 10.1109/PIERS62282.2024.10617965.

[80] Akram Sheikhi, Maryam Bazgir, and Mohammad Bagher Dowlatshahi. "Optimization and Machine Learning Algorithms for Intelligent Microwave Sensing: A Review." In: *Handbook of Formal Optimization*. Springer, 2024, pp. 1–33. DOI: 10.1007/978-981-19-8851-6_54-1.

[81] Keysight Technologies. *Keysight streamline series USB vector network analyzer P937XA 2-port, up to 26.5 GHz*. Available online: https://www.keysight.com/it/en/assets/7018-06033/data-sheets/5992-2765.pdf (accessed on: December 12, 2025). 2018.

[82] Cristina Origlia et al. "Anthropomorphic multi-tissue head phantom for microwave imaging devices testing." In: *2023 17th European Conference on Antennas and Propagation (EuCAP)*. IEEE. 2023, pp. 1–4. DOI: 10.23919/EuCAP57121.2023.10133539.

[83] MJ Ackerman. "The Visible Human Project: a resource for education." In: *Academic Medicine* 74.6 (1999), pp. 667–70.

[84] Nadine Joachimowicz et al. "Anthropomorphic breast and head phantoms for microwave imaging." In: *Diagnostics* 8.4 (2018), p. 85. DOI: 10.3390/diagnostics8040085.

[85] D Andreuccetti. *An Internet resource for the calculation of the dielectric properties of body tissues in the frequency range 10 Hz-100 GHz*. Available online: http://niremf.ifac.cnr.it/tissprop/ (accessed on: December 12, 2025). 2012.

[86] Keysight Technologies. *N1500A Materials Measurement Suite*. Available online: https://www.keysight.com/it/en/product/N1500A/materialsmeasurement-suite.html (accessed on: December 12, 2025). 2022.

[87] F. Pedregosa et al. "Scikit-learn: Machine Learning in Python." In: *Journal of Machine Learning Research* 12 (2011), pp. 2825–2830.

[88] Keysight Technologies. *M9804A PXIe Vector Network Analyzer*. Available online: https://www.keysight.com/it/en/assets/3119-1014/data-sheets/5992-3596.pdf (accessed on: December 12, 2025).

[89] The MathWorks, Inc. *Patternnet - Generate pattern recognition network*. Available online: https://www.mathworks.com/help/deeplearning/ref/patternnet.html (accessed on: December 12, 2025).

[90] Stanley Fahn. "The medical treatment of Parkinson disease from James Parkinson to George Cotzias." In: *Movement Disorders* 30.1 (2015), pp. 4–18. DOI: 10.1002/mds.26102.

[91] Lola Cook et al. "Parkinson's disease variant detection and disclosure: PD GENEration, a North American study." In: *Brain* 147.8 (2024), pp. 2668–2679. DOI: 10.1093/brain/awae142.

[92] Jason R Cannon and J Timothy Greenamyre. "Gene–environment interactions in Parkinson's disease: Specific evidence in humans and mammalian models." In: *Neurobiology of disease* 57 (2013), pp. 38–46. DOI: 10.1016/j.nbd.2012.06.025.

[93] Honglei Chen. "The changing landscape of Parkinson epidemiologic research." In: *Journal of Parkinson's Disease* 8.1 (2018), pp. 1–12. DOI: 10.3233/JPD-17123.

[94] Karen M Semchuk, Edgar J Love, and Robert G Lee. "Parkinson's disease and exposure to agricultural work and pesticide chemicals." In: *Neurology* 42.7 (1992), pp. 1328–1328. DOI: 10.1212/WNL.42.7.1328.

[95] Benjamin A Rybicki et al. "Parkinson's disease mortality and the industrial use of heavy metals in Michigan." In: *Movement disorders: official journal of the Movement Disorder Society* 8.1 (1993), pp. 87–92. DOI: 10.1002/mds.870080116.

[96] W Michael Caudle et al. "Industrial toxicants and Parkinson's disease." In: *Neurotoxicology* 33.2 (2012), pp. 178–188. DOI: 10.1016/j.neuro.2012.01.010.

[97] Mariah Caballero et al. "Estimated residential exposure to agricultural chemicals and premature mortality by Parkinson's disease in Washington state." In: *International journal of environmental research and public health* 15.12 (2018), p. 2885. DOI: 10.3390/ijerph15122885.

[98] Caroline M Tanner et al. "Rotenone, paraquat, and Parkinson's disease." In: *Environmental health perspectives* 119.6 (2011), p. 866. DOI: 10.1289/ehp.1002839.

[99] E Ray Dorsey et al. "Trichloroethylene: an invisible cause of Parkinson's disease?" In: *Journal of Parkinson's Disease* 13.2 (2023), pp. 203–218. DOI: 10.3233/JPD-225047.

[100] Vedad Delic et al. "Biological links between traumatic brain injury and Parkinson's disease." In: *Acta neuropathologica communications* 8.1 (2020), p. 45. DOI: 10.1186/s40478-020-00924-7.

[101] Natalia Palacios et al. "Particulate matter and risk of Parkinson disease in a large prospective study of women." In: *Environmental Health* 13.1 (2014), p. 80. DOI: 10.1186/1476-069x-13-80.

[102] Kai Zhen et al. "A systematic review and meta-analysis on effects of aerobic exercise in people with Parkinson's disease." In: *npj Parkinson's Disease* 8.1 (2022), p. 146. DOI: 10.1038/s41531-022-00418-4.

[103] Xiangpeng Ren and Jiang-Fan Chen. "Caffeine and Parkinson's disease: multiple benefits and emerging mechanisms." In: *Frontiers in Neuroscience* 14 (2020), p. 602697. DOI: 10.3389/fnins.2020.602697.

[104] Michael X Henderson, John Q Trojanowski, and Virginia M-Y Lee. "α-Synuclein pathology in Parkinson's disease and related α-synucleinopathies." In: *Neuroscience letters* 709 (2019), p. 134316. DOI: 10.1016/j.neulet.2019.134316.

[105] Jacob Horsager, Karoline Knudsen, and Michael Sommerauer. "Clinical and imaging evidence of brain-first and body-first Parkinson's disease." In: *Neurobiology of disease* 164 (2022), p. 105626. DOI: 10.1016/j.nbd.2022.105626.

[106] Jacob Horsager and Per Borghammer. "Brain-first vs. body-first Parkinson's disease: an update on recent evidence." In: *Parkinsonism & Related Disorders* 122 (2024), p. 106101. DOI: 10.1016/j.parkreldis.2024.106101.

[107] Karoline Knudsen et al. "Asymmetric dopaminergic dysfunction in brain-first versus body-first Parkinson's disease subtypes." In: *Journal of Parkinson's Disease* 11.4 (2021), pp. 1677–1687. DOI: 10.3233/JPD-212761.

[108] Jiaxin Shi et al. "MRI structural and functional axial asymmetry in the brain-first versus body-first subtypes of Parkinson's disease." In: *npj Parkinson's Disease* (2025). DOI: 10.1038/s41531-025-01219-1.

[109] Yoland Smith and Jeremy Z Kieval. "Anatomy of the dopamine system in the basal ganglia." In: *Trends in neurosciences* 23 (2000), S28–S33. DOI: 10.1016/S1471-1931(00)00023-9.

[110] P Damier et al. "The substantia nigra of the human brain: II. Patterns of loss of dopamine-containing neurons in Parkinson's disease." In: *Brain* 122.8 (1999), pp. 1437–1448. DOI: 10.1093/brain/122.8.1437.

[111] Nicolas Giguère, Samuel Burke Nanni, and Louis-Eric Trudeau. "On cell loss and selective vulnerability of neuronal populations in Parkinson's disease." In: *Frontiers in neurology* 9 (2018), p. 455. DOI: 10.3389/fneur.2018.00455.

[112] Carly B Young, Vamsi Reddy, and James Sonne. "Neuroanatomy, basal ganglia." In: *StatPearls [Internet]*. Available online: https://www.ncbi.nlm.nih.gov/books/NBK537141/ (accessed on: December 12, 2025). StatPearls Publishing, 2023.

[113] Clelia Pellicano et al. "Prodromal non-motor symptoms of Parkinson's disease." In: *Neuropsychiatric disease and treatment* 3.1 (2007), pp. 145–152. DOI: 10.2147/nedt.2007.3.1.145.

[114] Bastiaan R Bloem, Michael S Okun, and Christine Klein. "Parkinson's disease." In: *The Lancet* 397.10291 (2021), pp. 2284–2303. DOI: 10.1007/978-3-030-88832-9_112.

[115] Mauro Fasano, Bruno Bergamasco, and Leonardo Lopiano. "Modifications of the iron–neuromelanin system in Parkinson's disease." In: *Journal of neurochemistry* 96.4 (2006), pp. 909–916. DOI: 10.1111/j.1471-4159.2005.03638.x.

[116] Heather Wilson et al. "Cortical thinning across Parkinson's disease stages and clinical correlates." In: *Journal of the neurological sciences* 398 (2019), pp. 31–38. DOI: 10.1016/j.jns.2019.01.020.

[117] Mimi Li et al. "Global burden of Parkinson's disease from 1990 to 2021: a population-based study." In: *BMJ open* 15.4 (2025), e095610. DOI: 10.1136/bmjopen-2024-095610.

[118] Roberta Balestrino and Anthnoy HV Schapira. "Parkinson disease." In: *European journal of neurology* 27.1 (2020), pp. 27–42. DOI: 10.1111/ene.14108.

[119] Dongning Su et al. "Projections for prevalence of Parkinson's disease and its driving factors in 195 countries and territories to 2050: modelling study of Global Burden of Disease Study 2021." In: *bmj* 388 (2025). DOI: 10.1136/bmj-2024-080952.

[120] GBD 2021 Diseases and Injuries Collaborators. "Global, regional, and national epidemiology and trends of Parkinson's disease from 1990 to 2021." In: *Frontiers in Aging Neuroscience* 16 (2024). DOI: 10.3389/fnagi.2024.1498756.

[121] Yuanrong Luo et al. "Global, regional, national epidemiology and trends of Parkinson's disease from 1990 to 2021: findings from the Global Burden of Disease Study 2021." In: *Frontiers in aging neuroscience* 16 (2025), p. 1498756. DOI: 10.3389/fnagi.2024.1498756.

[122] K Ray Chaudhuri et al. "Economic burden of Parkinson's disease: A multinational, real-world, cost-of-illness study." In: *Drugs-Real World Outcomes* 11.1 (2024), pp. 1–11. DOI: 10.1007/s40801-023-00410-1.

[123] Paul McCrone, Liesl M Allcock, and David J Burn. "Predicting the cost of Parkinson's disease." In: *Movement Disorders* 22.6 (2007), pp. 804–812. DOI: 10.1002/mds.21360.

[124] Yuanrong Luo et al. "Global, regional, national epidemiology and trends of Parkinson's disease from 1990 to 2021: findings from the Global Burden of Disease Study 2021." In: *Frontiers in aging neuroscience* 16 (2025), p. 1498756. DOI: 10.1038/s41531-020-0117-1.

[125] Adrienne M Keener and Yvette M Bordelon. "Parkinsonism." In: *Seminars in neurology*. Vol. 36. 04. Thieme Medical Publishers. 2016, pp. 330–334. DOI: 10.1055/s-0036-1585097.

[126] Christopher G Goetz et al. "Movement Disorder Society-sponsored revision of the Unified Parkinson's Disease Rating Scale (MDS-UPDRS): scale presentation and clinimetric testing results." In: *Movement disorders: official journal of the Movement Disorder Society* 23.15 (2008), pp. 2129–2170. DOI: 10.1002/mds.22340.

[127] Johannes Levin et al. "The differential diagnosis and treatment of atypical parkinsonism." In: *Deutsches Ärzteblatt International* 113.5 (2016), p. 61. DOI: 10.3238/arztebl.2016.0061.

[128] Ümit Özgür Akdemir, Hatice Ayşe Tokçaer Bora, and Lütfiye Özlem Atay. "Dopamine transporter spect imaging in Parkinson's disease and parkinsoniandisorders." In: *Turkish journal of medical sciences* 51.2 (2021), pp. 400–410. DOI: 10.3906/sag-2008-253.

[129] PK Morrish, GV Sawle, and DJ Brooks. "Clinical and [18F] dopa PET findings in early Parkinson's disease." In: *Journal of Neurology, Neurosurgery & Psychiatry* 59.6 (1995), pp. 597–600. DOI: 10.1136/jnnp.59.6.597.

[130] David Sulzer et al. "Neuromelanin detection by magnetic resonance imaging (MRI) and its promise as a biomarker for Parkinson's disease." In: *NPJ Parkinson's disease* 4.1 (2018), p. 11. DOI: 10.1038/s41531-018-0047-3.

[131] Mohammad Shahnawaz et al. "Development of a biochemical diagnosis of Parkinson disease by detection of α-synuclein misfolded aggregates in cerebrospinal fluid." In: *JAMA neurology* 74.2 (2017), pp. 163–172. DOI: 10.1001/jamaneurol.2016.4547.

[132] Christopher H Gibbons et al. "Skin biopsy detection of phosphorylated α-synuclein in patients with synucleinopathies." In: *Jama* 331.15 (2024), pp. 1298–1306. DOI: 10.1001/jama.2024.0792.

[133] Nimrod Madrer et al. "Pre-symptomatic Parkinson's disease blood test quantifying repetitive sequence motifs in transfer RNA fragments." In: *Nature Aging* (2025), pp. 1–15. DOI: 10.1038/s43587-025-00851-z.

[134] Richard Nathaniel Rees et al. "An early diagnosis is not the same as a timely diagnosis of Parkinson's disease." In: *F1000Research* 7 (2018), F1000–Faculty. DOI: 10.12688/f1000research.14528.1.

[135] Anastasia Bougea. "Application of wearable sensors in Parkinson's disease: state of the art." In: *Journal of Sensor and Actuator Networks* 14.2 (2025), p. 23. DOI: 10.3390/jsan14020023.

[136] Bahar Demir, Sezer Ulukaya, and Oğuzhan Erdem. "Detection of Parkinson's disease with keystroke data." In: *Computer Methods in Biomechanics and Biomedical Engineering* 26.13 (2023), pp. 1653–1667. DOI: 10.1080/10255842.2023.2245516.

[137] Lorenzo Simone et al. "Interpretable Early Detection of Parkinson's Disease Through Speech Analysis." In: *International Conference on Artificial Intelligence in Medicine*. Springer. 2025, pp. 373–378. DOI: 10.48550/arXiv.2504.17739.

[138] Yuzhe Yang et al. "Artificial intelligence-enabled detection and assessment of Parkinson's disease using nocturnal breathing signals." In: *Nature medicine* 28.10 (2022), pp. 2207–2215. DOI: 10.1038/s41591-022-01932-x.

[139] Maosong Jiang et al. "Auxiliary diagnostic method of Parkinson's disease based on eye movement analysis in a virtual reality environment." In: *Neuroscience Letters* 842 (2024), p. 137956. DOI: 10.1016/j.neulet.2024.137956.

[140] David G Coughlin et al. "α-synuclein seed amplification assay amplification parameters and the risk of progression in prodromal parkinson disease." In: *Neurology* 104.5 (2025), e210279. DOI: 10.1212/WNL.0000000000210279.

[141] Gabriel Torres-Pasillas et al. "Olfactory dysfunction in parkinson's disease, its functional and neuroanatomical correlates." In: *NeuroSci* 4.2 (2023), pp. 134–151. DOI: 10.3390/neurosci4020013.

[142] Shannon Halloway et al. "Association of neurofilament light with the development and severity of Parkinson disease." In: *Neurology* 98.22 (2022), e2185–e2193. DOI: 10.1212/WNL.0000000000200338.

[143] Gael Moquin-Beaudry et al. "Mapping the peripheral immune landscape of Parkinson's disease patients with single-cell sequencing." In: *Brain* (2025), awaf066. DOI: 10.1093/brain/awaf066.

[144] Jamir Pitton Rissardo and Ana Letícia Fornari Caprara. "Cardiac 123I-Metaiodobenzylguanidine (MIBG) scintigraphy in Parkinson's disease: a comprehensive review." In: *Brain Sciences* 13.10 (2023), p. 1471. DOI: 10.3390/brainsci13101471.

[145] Youness Akazzim et al. "UWB-modulated microwave imaging for human brain functional monitoring." In: *Sensors* 23.9 (2023), p. 4374. DOI: 10.3390/s23094374.

[146] Youness Akazzim et al. "UWB microwave functional brain activity extraction for Parkinson's disease monitoring." In: *IEEE Sensors Journal* 24.3 (2023), pp. 3844–3852. DOI: 10.1109/JSEN.2023.3341168.

[147] Udo Kaatze. "Complex permittivity of water as a function of frequency and temperature." In: *Journal of Chemical and Engineering Data* 34.4 (1989), pp. 371–374. DOI: 10.1021/je00058a001.

[148] Alessandro Di Bucchianico. "Coefficient of determination (R 2)." In: *Encyclopedia of statistics in quality and reliability* (2008). DOI: 10.1002/9780470061572.eqr173.

[149] Keysight Technologies. *N9918A FieldFox Handheld Microwave Analyzer, 26.5 GHz*, Available online: https://www.keysight.com/us/en/product/N9918A/fieldfox-a-handheldmicrowave-analyzer-26-5-ghz.html (accessed on: December 12, 2025).

[150] Keysight Technologies. *N1500A Materials Measurement Suite*. Available online: https://www.keysight.com/it/en/product/N1500A/materialsmeasurement-suite.html (accessed on: December 12, 2025). 2022.

[151] Rohde & Schwarz. *R&S ZNA26 Vector Network Analyzer*. Available online: https://www.rohde-schwarz.com/us/products/test-and-measurement/network-analyzers/rs-zna-vector-network-analyzers_63493-551810.html (accessed on: December 12, 2025).

[152] Youness Akazzim et al. "Multi-element UWB probe optimization for medical microwave imaging." In: *Sensors* 23.1 (2022), p. 271. DOI: 10.3390/s23010271.

[153] Saba Rashid et al. "3-D printed UWB microwave bodyscope for biomedical measurements." In: *IEEE Antennas and Wireless Propagation Letters* 18.4 (2019), pp. 626–630. DOI: 10.1109/LAWP.2019.2899591.

[154] Lluis Jofre et al. "UWB tomographic radar imaging of penetrable and impenetrable objects." In: *Proceedings of the IEEE* 97.2 (2009), pp. 451–464. DOI: 10.1109/JPROC.2008.2008854.

[155] James Sonne, Vamsi Reddy, and Morris R Beato. "Neuroanatomy, substantia nigra." In: *StatPearls [Internet]*. Available online: https://www.ncbi.nlm.nih.gov/books/NBK536995/ (accessed on: December 12, 2025). StatPearls Publishing, 2024.

[156] V Mariano et al. "Early Detection of Alzheimer's Disease via Microwave Sensing Technique Applied to the Neck." In: *2024 4th URSI Atlantic Radio Science Meeting (AT-RASC)*. IEEE. 2024, pp. 1–4. DOI: 10.46620/URSIATRASC24/HMZB1465.

This Ph.D. thesis has been typeset by means of the TEX-system facilities. The typesetting engine was LuaLATEX. The document class was `toptesi`, by Claudio Beccari, with option `tipotesi=scudo`. This class is available in every up-to-date and complete TEX-system installation.